HYDROGEOLOGICAL CHARACTERISATION AND GROUNDWATER VULNERABILITY TO POLLUTION MAPPING OF THE THYSPUNT NUCLEAR SITE, EASTERN CAPE

MSc RESEARCH REPORT

BY

SEEKE CAROL MOHUBA (839981)

SCHOOL OF GEOSCIENCES

SUPERVISOR: PROF. TAMIRU ABIYE

CO-SUPERVISOR: MR. KHULISO MASINDI

JUNE 2020

ACKNOWLEDGEMENTS

I would like to extend my most sincere gratitude to my supervisor, Prof. Tamiru Abiye for the amazing opportunity, his unprecedented wisdom and guidance throughout this research and my MSc studies as a whole. I can never thank you enough for always pushing me to reach my potential and for the amazing support you have given me. Thank you!

To my co-supervisor, Mr. Khuliso Masindi, I wholeheartedly extend my gratitude to you for the incredible support, guidance and assistance you have given me throughout my studies.

I wish to thank Prof. Molla Demlie for his unreserved assistance during the field work and constructive discussions we made during the course of the research besides the hydrochemical analysis of water samples.

To Dr. Margaret Mkhosi, I can never thank you enough for the generous support, financially and in all other aspects. I most sincerely appreciate the opportunity you gave me. To Mr. Madimetja Segobola, thank you very much for the support and opportunity you afforded me. I am truly grateful! I wish to thank them again for facilitating the field access through ESKOM for data collection.

I wish to thank Mr. Lindani Mkhize, Ms. Nthabiseng Mohlala and Ms. Queen Motaung from the NNR laboratory for helping me with the radionuclide analyses

To Mr. Mike Butler, thank you very much for all your assistance and support in the tritium, ^{13}C and ^{14}C analyses.

To my beautiful, wise mother, Mamadile Mohuba. Words fall short of expressing my love and appreciation for you. Thank you for your unprecedented love, support and advice. Thank you for always being my pillar of strength, for always being in my corner and being the worldly mother that you are.

To my wonderful siblings, Regaogetswe, Koketso and Kabelo. I love and appreciate you wholeheartedly. Thank you for always supporting me and pushing me to become the best version of myself. My precious niece, Bokang, thank you for always keeping me grounded and giving me serenity and haven when I needed it most. Mmane loves you wholeheartedly.

To Moneri Modiba, thank you being an amazing research partner turned friend. I appreciate the knowledge and ideas shared. Your support and assistance are highly appreciated.

To the NNR's Dr. Sifiso Nhleko, Mr. Lindani Mkhize, Mr. Wonderboy Gubela and Mr. Tiyane Maluleke; I sincerely thank you for the wonderful assistance you offered me during the field campaign.

To my wonderful family and friends, thank you for the love and support with which you continue to shower me.

To everyone who was directly and indirectly involved in this research, I appreciate all your contributions, for they made this research possible.

ABSTRACT

A thorough understanding of the hydrogeological system and its dynamics are crucial to achieve sustainable development in the area. A detailed hydrogeological characterisation and mapping the groundwater vulnerability to pollution of the Thyspunt Nuclear Site is presented based on desktop studies, field investigations and laboratory analyses. The geology of the area comprises of the Table Mountain Group (TMG) and the Bokkeveld Group of the Cape Supergroup, indurated coastal Cenozoic deposits of the Algoa Group and Quaternary to Recent sand deposits. Algoa Group sediments, dunes and fractured quartzite of the TMG comprise unconfined aquifer system in the area. Underlying the unconfined aquifers are confined aquifer composed of fracture TMG quartzites. Additionally, as a result of ductile deformation that resulted in the formation of regional anticline, artesian system has been developed, which is characterised by slightly acidic and oxidising water. The aquifers show high variability in physical properties, including variability within each aquifer type, as indicated by the wide range of values in hydraulic conductivity (0.0115 - 19.13 m/day), transmissivity (0.359-108.3 m^2/day) and aquifer thickness (12.85-112.4 m).

The mean annual rainfall ranges between 302 and 922.6 mm (ave. 612.3 mm/year), while the estimated potential evapotranspiration (PET) and the actual evapotranspiration (AET) are 821.5 and 535.9 mm/year, respectively. Annual recharge estimated using the Water Table Fluctuation Method ranges between 0.588 and 72.183 mm/year (ave. 36.092 mm/year). The main hydrochemical facies across the study area is Ca-Mg-HCO_3 type. The groundwater hydrochemical evolution appears to be from a fresh Ca-Mg-HCO_3 type at shallow depth to saline Na-Cl type water in the direction of groundwater flow from west to east. Similarities in the stable isotope signatures indicate a strong hydraulic link between most aquifers and springs, and a strong link between some of the different aquifers. No evidence of seawater intrusion in the sampled aquifers has been noted. All groundwater samples have depleted isotope signatures, indicating that recharge occurred during colder season or from rainfall originating from a high latitude region. The baseline geochemical analyses indicate that the shales of the Ceres Subgroup and Baviaanskloof Formation contain elevated concentrations of metals, especially Cobalt, Thorium, Lead and Uranium. The highest uranium and thorium concentrations were encountered at the Thyspunt site in the quartzite of the Skurwerburg Formation, where most of the rocks contain highly elevated metals and radionuclides. Moreover, elevated concentrations of uranium were also noted in soils sampled from the footprint area of the site. A conceptual

hydrogeological model for the Thyspunt area was proposed based on data from field, laboratory and desktop studies. Multiple hydrostratigraphic units based on lithological logs and aquifer properties exist, where unconfined aquifers with weathered quartzite/sandstone/shale and interstitial sand is the most dominant system underlain by fractured quartzite that is often generates artesian system. Groundwater flow direction is towards the Ocean and hence, helps to buffer the effect of seawater intrusion. The fact that most springs discharge into the sea, coupled with the fold orientation signifies less chance for seawater to penetrate into the aquifers. Based on the DRASTIC model, the foot print area is situated at the medium and high vulnerability zone comprised of Algoa Group sediments underlain by fractured quartzites.

TABLE OF CONTENTS

ACKNOWLEDGEMENTS II

ABSTRACT III

1. INTRODUCTION 1

1.1 RESEARCH BACKGROUND 1

1.2 AIMS AND OBJECTIVES 3

1.3 LITERATURE REVIEW 3

2. DESCRIPTION OF THE STUDY AREA 6

2.1 LOCATION 6

2.2 CLIMATE 6

2.4 LAND USE AND COVER 7

3. METHODOLOGY 9

3.1 DESKTOP INVESTIGATIONS 9

3.2 FIELD INVESTIGATIONS 10

3.2.1 Geological mapping 10

3.2.2 Hydrogeological investigation 11

3.2.3 Infiltration tests 12

3.2.4 Water sampling 13

3.3 LABORATORY ANALYSES 14

3.3.1 Hydrochemistry 14

3.3.2 Environmental isotopes 15

3.3.3 Rock and soil chemistry sampling 16

3.3.4 Radionuclide analyses 17

3.4 DATA ANALYSIS 17

3.4.1 Pumping test data analysis 17

3.5 GROUNDWATER VULNERABILITY TO POLLUTION MAPPING 18

4. RESULTS AND DISCUSSION 24

4.1 EVAPOTRANSPIRATION 24

4.2 GEOLOGICAL SETTING 24

4.3. HYDROGEOLOGICAL CONDITIONS 28

4.3.1 Aquifer characterisation 28

4.3.2 Groundwater levels and flow direction 31
4.4. GROUNDWATER DISCHARGE 32
4.5 GROUNDWATER RECHARGE AND AVAILABILITY 33
4.5.1 Groundwater Recharge 33
4.5.2 Infiltration test 38
4.6 PHYSICOCHEMICAL AND HYDROCHEMISTRY 40
4.6.1 Temperature (℃) 40
4.6.2 Oxidation- reduction potential (ORP) 40
4.6.3 Hydrogen ion activity (pH) 41
4.6.4 Electrical conductivity (EC) 42
4.6.5 Total dissolved solids (TDS) 42
4.6.6 Hydrochemical facies 45
4.7. ENVIRONMENTAL ISOTOPES 52
4.7.1. Deuterium excess (d) 53
4.7.2. Tritium, ^{13}C and ^{14}C 56
4.8. BACKGROUND CHEMISTRY: ROCK, SOIL AND WATER 60
4.9. BASELINE RADIATION 65
4.9.1. Naturally Occurring Radioactive Materials (NORM) in water 65
4.9.2. Tritium concentration in surface water, groundwater and sea water 68
4.9.3. Uranium, thorium and lead concentrations in water 70
4.9.4. NORM in soils 75
4.9.5. Uranium, thorium and lead concentrations in soil 76
4.9.6. NORM in rocks 79
4.9.7. Lead, uranium and thorium concentrations in rocks 81
4.9.8. Effective dose in water 85
4.10. CONCEPTUAL HYDROGEOLOGICAL MODEL FOR THE THYSPUNT AREA 89

5. GROUNDWATER VULNERABILITY TO POLLUTION MAPPING 91
5.1. DEPTH TO GROUNDWATER 91
5.2. RECHARGE 92
5.3. AQUIFER MEDIA 94
5.4. SOIL MEDIA 95
5.5. TOPOGRAPHY 97
5.6. IMPACT OF THE VADOSE ZONE 98
5.7. CONDUCTIVITY (HYDRAULIC) 100
5.8. INTRINSIC VULNERABILITY MAP 101
5.9. SPECIFIC VULNERABILITY MAP 103
5.10. DRASTIC VALIDATION 106

6. CONCLUSION 107

7. RECOMMENDATIONS **109**

8. REFERENCES **110**

LIST OF FIGURES

Figure 2.1. Locality map of the study area. 6

Figure 2.2. Monthly rainfall of Thyspunt. 7

Figure 2.3. Topographic map of the study area in the form of DEM. Note the sampling locations in relation to the surface elevation…….……..8

Figure 3.1. Strike and Dip measurement 11

Figure 3.2: a) Double-ring infiltrometer used to determine soil infiltration rates. b) Field-based infiltration test. 12

Figure 3.3. A) Borehole sampling after purging. B) Wetland sampling 13

Figure 3.4. Water sampling points……..……..…23

Figure 3.5 A) Total Alkalinity titration B) Onsite parameter measurements with CRISON multimeter probe…….....…….……23

Figure 3.6. Sampling for ^{14}C with 60 Litres jar…….……16

Figure 3.7. Soil sampling…….…….……..17

Figure 4.1. a) Highly fractured quartzite coastal outcrops of the Skurwerburg Formation in Thyspunt. b) Skurwerburg Formation quartzite along the coast…….25

Figure 4.2. A) Ceres Subgroup shale B) Baviaanskloof Formation (Organic shale from a quarry) 25

Figure 4.3. Peninisula Formation: A) Peninsula Formation quartzite B)Peninsula Formation ferruginous quartzite …….……26

Figure 4.4. A) Extensive mobile dunes and B) The footprint area as seen from the meteorological station, covered by dunes and Fynbos vegetation……..……..…27

Figure 4.5. Indurated sediment of the Algoa Group (Courtesy: Prof. Tamiru Abiye)…….…….27

Figure 4.6. Geological map of Thyspunt area. Note N-S sectional line used for cross-section construction …….....….…….28

Figure 4.7. Geological cross-section from S to N direction. 28

Figure 4.8. Artesian boreholes in the area……..……...30

Figure 4.9. Depth to groundwater level map of Thyspunt……..30

Figure 4.10. Groundwater flow direction map of Thyspunt area……..33

Figure 4.11. Schematic sketch representing contact spring occurrence in the area…….34

Figure 4.12. Schematic sketch representing depression spring occurrence in the area…….…..34

Figure 4.13. Groundwater levels measured in borehole THY_MR5……35

Figure 4.14. Groundwater levels measured in borehole THY_RP11…….....36

Figure 4.15. Groundwater levels measured in borehole THY_RP2. Red circles outline recharge periods……..…….…..36

Figure 4.16. Monthly rainfall and groundwater level of THY-MR5 and THY-RP2…...37

Figure 4.17. Infiltration graph of Rosa Farm……38

Figure 4.18. Infiltration graph of the Foootprint Area.....……..38

Figure 4.19. Spatial ORP map of Thyspunt……...……...40

Figure 4.20. Spatial pH map of Thyspunt.....43

Figure 4.21. Spatial Electrical Conductivity map of Thyspunt.....43

Figure 4.22. Spatial distribution map of total dissolved solids at Thyspunt.....44

Figure 4.23. Piper plot for the Thyspunt samples 46

Figure 4.24. Gibbs diagrams of Thyspunt groundwater and spring samples 45

Figure 4.25. Major cations and metal concentrations of the analysed samples. 48

Figure 4.26. Iron rich water from shale containing aquifer.....48

Figure 4.27. Chloride and sodium variation diagram of Thyspunt samples 49

Figure 4.28. Chloride and bicarbonate variation in the Thyspunt samples 49

Figure 4.29. Calcium and bicarbonate variation in the Thyspunt samples.....50

Figure 4.30. Stable environmental isotope ($\delta^{18}O$ and $\delta^{2}H$) plot of surface water and groundwater samples collected around Thyspunt.....52

Figure 4.31. Scatter plots of $\delta^{18}O$ and deuterium excess. Note the circles mark the different clusters that represent different moisture sources……..……55

Figure 4.32. Scatter plots of $\delta^{18}O$ and tritium……..……..……58

Figure 4.33. Tritium spatial distribution map of Thyspunt.....59

Figure 4.34. Trace element concentration ranges of rock samples from Thyspunt. 63

Figure 4.35.Trace element concentration ranges of 7 soil samples from Thyspunt. 65

Figure 4.36. Water sample location……..……..66

Figure 4.37. Radionuclide concentrations in water samples from the Thyspunt area….67

Figure 4.38. Tritium sample positions…….……68

Figure 4.39. Spatial distribution map of Tritium in the Thyspunt area……..……..70

Figure 4.40. Sample locations of uranium, lead and thorium water samples……...72

Figure 4.41. Uranium concentration proportion map (units: ppm)…….…74

Figure 4.42. Thorium concentration proportion map (Units: ppm)…….75

Figure 4.43. Lead concentration proportion map (units: ppm)…….76

Figure 4.44. Radionuclide concentrations in rock samples from the Thyspunt area..…78

Figure 4.45. Shale quarry…….……80

Figure 4.46: Rock sampling points in the Thyspunt area…….……..81

Figure 4.47: Lead concentration proportion map (Units: ppm)……82

Figure 4.48. Uranium concentration proportion map (units: ppm)…….…….84

Figure 4.49. Thorium concentration proportion map (Units: ppm)…….…84

Figure 4.50: Rock sampling points in the Thyspunt area…….……..86

Figure 4.51. Lead concentration proportion map (Units: ppm)……87

Figure 4.52. Uranium concentration proportion map (units: ppm)……..……...88

Figure 4.53. Thorium concentration proportion map (Units: ppm)……..……89

Figure 4.54. S - N conceptual model for Thyspunt…….……90

Figure 5.1. Depth to groundwater map…….……..96

Figure 5.2. Depth to groundwater ratings…….…….……..97

Figure 5.3. Annual recharge map……..…….……...…..98

Figure 5.4. Recharge rating map……..……...…98

Figure 5.5. Aquifer map of the Thyspunt area……..……...…….99

Figure 5.6. Aquifer rating map……...……...……..100

Figure 5.7. Soil map…….…..……..…….101

Figure 5.8. Soil rating map……..…….……...…….101

Figure 5.9. Slope percentage distribution……..…..……..……..102

Figure 5.10. Topography rating map……..…….…..……103

Figure 5.11. The lithology of the vadose zone map…….…….……...…104

Figure 5.12. Vadose zone rating map……...……...104

Figure 5.13. Hydraulic conductivity map…….…...……...105

Figure 5.14. Hydraulic conductivity rating map……...……....106

Figure 5.15. Intrinsic aquifer vulnerability to pollution map of the Thyspunt area.....108

Figure 5.16. Nuclear activity rating map. Note rating 8 refers to road buffer……....109

Figure 5.17. Specific vulnerability map, in regards to the Nuclear Power Station in the Thyspunt area…….…..110

LIST OF TABLES

Table 3.1: DRASTIC parameters' data sources……..……..……..19

Table 3.2: Parameter weightings and ratings associated with each range…….……..20

Table 3.3: Percentage influence ratings for each DRASTIC parameter..…….……23

Table 4.1: Monthly and Annual Potential Evapotranspiration estimates of Thyspunt. ..25

Table 4.2. Structural data of different geological formations in Thyspunt. 28

Table 4.3: aquifer properties determined from drilling logs and pumping test analyses of boreholes using Fitts Geosolutions software……..….30

Table 4.4. WTF recharge estimation for Thyspunt for the years 2012 and 2013.....35

Table 4.5. Soil sample characteristics of 7 soil samples from Thyspunt.....38

Table 4.6: Soil sample characteristics of 7 soil samples from Thyspunt. 38

Table 4.7: Range of values for major ions and metals in water.....46

Table 4.8: Correlation matrix of 17 physiochemical and hydrochemical variables for 15 samples……..……...50

Table 4.9: Deuterium excess of 54 water samples……..…….53

Table 4.10: Groundwater residence time…….……56

Table 4.11: Petrographic descriptions of 12 rock samples from Thyspunt…….60

Table 4.12: Trace elements range of values for rock samples …….……61

Table 4.13: Geochemical results of soil samples…….……64

Table 4.14: Activity concentration (Bq/L) in water from the Thyspunt area……..68

Table 4.15: Range of values for activity concentration in water from the Thyspunt area……..69

Table 4.16. Tritium concentration in water sampled from the Thyspunt area……71

Table 4.17. Range of values of radioactive trace metals in water samples from Thyspunt…….74

Table 4.18: Radionuclide concentration in rocks from the Thyspunt area…….…79

Table 4.19: Radioactive trace metal concentrations in soils from Thyspunt……81

zTable 4.20: Range of values for radioactive trace metals in rocks from Thyspunt....…85

Table 4.21: Radioactive trace metal concentrations in rocks from Thyspunt…..……87

Table 4.22: Male ingestion effective dose in eight water samples…….…….94

Table 4.23: Female ingestion effective dose in eight water samples…….…….94

ABBREVIATIONS

AET: Actual Evapotranspiration

DI: Drastic Index

DWAF: Department of Water Affairs and Forestry

DWS: Department of Water and Sanitation

EC: Electrical Conductivity

Mbgl: Meters below ground level

MWL: Meteoric Water Line

NNR: National Nuclear Regulator

NRF: National Research Foundation

ORP: Oxidation Reduction Potential

PET: Potential Evapotranspiration

SAWS: South African Weather Services

TDS: Total Dissolved Solids

TMG: Table Mountain Group

WTF: Water Table Fluctuation

1. INTRODUCTION

1.1 Research Background

Groundwater is a ubiquitous, natural resource found at different depths, with variable quality and volume. It is essential for sustaining life and the environment. Groundwater occurs invariably in different geological formations controlled by geological properties including faults, fractures, weathering profiles and the primary pore spaces. The sustainable development of an area needs to include a thorough understanding of the dynamics of aquifer system (Taylor *et al.*, 2017), where the understanding of aquifer systems requires vast amount of data and information about the various aspects of groundwater occurrence, circulation, storage and quality within the system. Aquifer characterisation affords stakeholders to undertake a sound decision-making and adequate groundwater resources management (Ahmed, 2009). It is very fundamental in the applications of groundwater modelling, especially where the representation of the spatial heterogeneity greatly influences the system's behaviour (Ahmed, 2009). However, in the case of lack of data (meteorological, geological and hydrogeological) and infrastructure (e.g. boreholes), the accurate characterisation of aquifers will be very difficult (Ahmed, 2009; Taylor *et al.*, 2017). This, therefore, diminishes the practicality and accuracy of results (both conceptual hydrogeological and numerical groundwater flow models).

Groundwater has direct interaction with saline water along coastal regions that are known to contain relatively fresh groundwater in the coastal sediments as compared to the saline ocean water. However, the intrusion of seawater into the aquifer poses a great risk to the quality of the groundwater, and thus limits the applicability of the groundwater for different uses (Han *et al.*, 2011). Both surface and ground water resources are potentially vulnerable to pollution emanating from human activities including the operation of nuclear power plants. The potential for pollution, which is defined as vulnerability or risk of groundwater to pollution, is related to the natural setting of an area in relation to hydrology, hydrogeology and geology. Groundwater seems less sensitive to pollution relative to surface water, however, the extent of the impact of human activities on groundwater may not be easily identified. Since groundwater is in continuous circulation within aquifers at different flow rates that depend on the hydrogeological characteristics of aquifers, this, therefore, renders the prediction of groundwater movement (together with the contaminants) and availability very difficult. Once contaminants are introduced into groundwater system, they persist and move at the groundwater velocity towards the discharge areas (Chilton, 1996). The operational (e.g. waste disposal) and

accidental release of toxic waste may reach groundwater resulting in the contamination of the aquifer with irreversible damage.

Chemicals released into the atmosphere can also reach groundwater via deposition onto the ground surface and its subsequent leaching of the deposited chemicals into the subsurface (Chilton, 1996).

From hydrogeological perspective, quantitative and precise criteria for the suitability of a site for the location of toxic industries are rarely used. However, the principal criteria would be the selection of a site where the likelihood of interaction of chemicals from the toxic industries with the major aquifers is minimal. Additionally, a site where the prediction of groundwater flow with a high confidence degree based on numerical modelling of groundwater flow and the travel time to the adjacent surface water bodies and potential users of groundwater exists.

The rehabilitation of polluted aquifers is a very expensive and difficult process, thus a proactive approach to the protection of groundwater is both technically and economically more viable (Leyland et al., 2008). Aquifer vulnerability mapping is an example of a proactive approach. According to the National Research Council (1993), groundwater vulnerability to contamination is "the likelihood or tendency for contaminants to reach a specified position in the groundwater system after introduction at some location above the aquifer". The process of natural attenuation occurs when pollutants migrate through the unsaturated zone and chemical, biological and physical interactions between the pollutants and material in the unsaturated zone lead to the reduction in concentration (Leyland *et al*., 2008).

Conceptualisation of hydrogeological system is very helpful to understand how aquifers work. Conceptual models that are developed for hydrogeological systems are crucial tools for assessing the impacts on the environment as well as in the analyses of the safety of toxic metal industries (Giacinto et al., 2010). In light of the proposed nuclear power plant at Thyspunt, conceptual hydrogeological model serves the primary purpose of developing mitigation measures or plans so as to minimize the effects on safety and public health during the normal operation and accidental conditions (e.g. accidental spills) (Giacinto *et al.*, 2010).

This research envisages contributing to better understanding the prevailing hydrogeological conditions around the Thyspunt area through the development of robust conceptual hydrogeological model based on detailed aquifer characterisation. Conceptual models represent the baseline hydrogeological conditions in the area. The development of the conceptual model is supported by among others collection and analyses of hydrogeochemical data including major ions and metals, environmental isotopes (^{2}H, ^{18}O and ^{3}H), soil and rock geochemical data. The application of environmental isotopes together with certain major ions (e.g. chloride and bromide) will also allow

for the detection of any seawater intrusion in the aquifers. The conceptual hydrogeology model further assist in preparing a groundwater vulnerability to pollution map for the Thyspunt area.

1.2 Aims and objectives

The main aims of this research are:

- To perform detailed hydrogeological characterisation of the aquifers.
- To assess the degree of vulnerability of the aquifers to pollution.

In order to address the aims of the project, key objectives are:

- To develop a conceptual hydrogeological model, including field based infiltration test that can potentially carry pollutants into the aquifers, and determining the hydraulic link between the aquifers as well as between the aquifers and surface water bodies.
- To map the degree of groundwater vulnerability to pollution
- To establish the background hydrogeological and hydrochemical conditions.
- To assess the presence of seawater intrusion in the area.

1.3 Literature review

Conceptual hydrogeological modelling that focuses on the characterisation of aquifers has been widely used to enhance the understanding of different hydrogeological systems. Zeng *et al.* (2015) developed a conceptual model of the karstic aquifer system in the Jade Dragon Snow Mountain (JDSM) region of southwestern China. This was done to understand aquifer characteristics and dynamics, and the connection between the regional climate-warming induced glacier melt water and the groundwater system. Extensive hydrochemical and stable isotope measurements and analyses, coupled with hydrogeological survey of the area were done to acquire the necessary data for developing a conceptual hydrogeological model. Analyses were conducted on the recharging water (rainwater and glacier melt water) and springs (Zeng *et al.*, 2015). The resultant conceptual hydrogeological model suggested a fracture-diffuse flow karstic aquifer system exists in the area (Zeng *et al.*, 2015).

The combined use of hydrochemistry, hydrogeology and stable isotope data proved to be a successful approach in the development of a conceptual model in the groundwater system. Join *et al.* (2005) constructed a conceptual model of the Piton de la Fournaise volcano (Reunion Island) to understand the hydrogeological system dynamics in active shield volcanoes. The development of conceptual

models of groundwater systems in active volcanoes has always been a controversial subject, because of the complexity of studying groundwater within active volcanoes (Join *et al.*, 2005). The relatively great depth of the water levels in the area led to the use of indirect prospecting methods, particularly geophysical surveys. Pre-existing data on the hydrogeology, geology and hydrochemistry acquired from field measurements and surveys were used to generate the model (Join *et al.*, 2005). As a way of validating the resultant conceptual model, a numerical flow simulation was conducted and this confirmed the presence of a single groundwater system as opposed to the previously proposed multiple disconnected aquifers (Join *et al.*, 2005).

A South African example of the application of conceptual modelling is the study by Ndlovu (2015) on Kosi Bay Lakes System in Kwa-Zulu Natal. The development of a conceptual model was initiated to understand the occurrence and interaction of surface water and groundwater, while also characterising the groundwater and surface water systems. A wide spectrum of data including field measurements, stable isotopes and pre-existing data on borehole logs, hydrochemistry, geophysics and borehole yield were successfully utilised to generate the model (Ndlovu, 2015), where it was reported that the groundwater system and the Kosi Bay Lakes are hydraulically connected as suggested by the conceptual model.

In order to carry out groundwater vulnerability to pollution mapping, a DRASTIC model (Aller et al., 1987) was deployed in several studies. The GIS based DRASTIC tool has been extensively applied to many aquifer vulnerability studies (e.g. Lobo Ferreira and Oliveira (1997); Magnuszewski and Suchozebrski (1998); Mato (2007) and Celico *et al.* (2007)) and the application has mostly been successful as proven by the groundwater analyses. The Council of Geosciences employed the DRASTIC vulnerability mapping method to produce a vulnerability map of South Africa (https://www.geoscience.org.za/images/geohazard/Groundwater_vulnerability.pdf). The modified DRASTIC Index was used in order to factor in anthropogenic influences on the pollution of groundwater (Musekiwa and Majola, 2011). This is because anthropogenic activities may have a control on the presence or absence of pollutants in the groundwater. The success of this study was further validated by the good correlation of nitrate concentrations and electrical conductivity with the resultant groundwater vulnerability map.

Mostert (2014) applied the DRASTIC method on a more local scale for the vulnerability mapping of the Rustenburg Municipality. Like the Council for Geosciences study, hydrogeological data relevant for vulnerability mapping were acquired from various agencies. The lack of publically available hydraulic conductivity data led to the omission of the conductivity parameter to avoid skewness of the data and results (Mostert, 2014). Land-use parameter was incorporated in the calculation of the drastic index since the presence of land-use activities exerts potential contamination pressure on the

underlying aquifer; and because the area is dominated by various potential pollution sources (Mostert, 2014). This resulted in the successful generation of DRASTI and DRASTIL maps. The incorporation of the land-use parameter resulted in the changes in the vulnerability distribution of the area; but the severity of vulnerability did not significantly change (Mostert, 2014).

The application of these methods in different areas of the world that differ hydrogeologically, climatically and geologically attests to the flexibility and reliability of these methods in generating robust conceptual models and vulnerability maps.

2. DESCRIPTION OF THE STUDY AREA

2.1 Location

This study focuses on the proposed nuclear power plant at Thyspunt, which is situated in the western region of the Southern Cape Mountain Range in the Eastern Cape Province of South Africa (Figure 2.1). The proposed site is situated approximately 120 km west of Port Elizabeth, between Oyster Bay and Cape St Francis within the K80F, K90D, and K90E quaternary catchments as shown in Figure 2.1

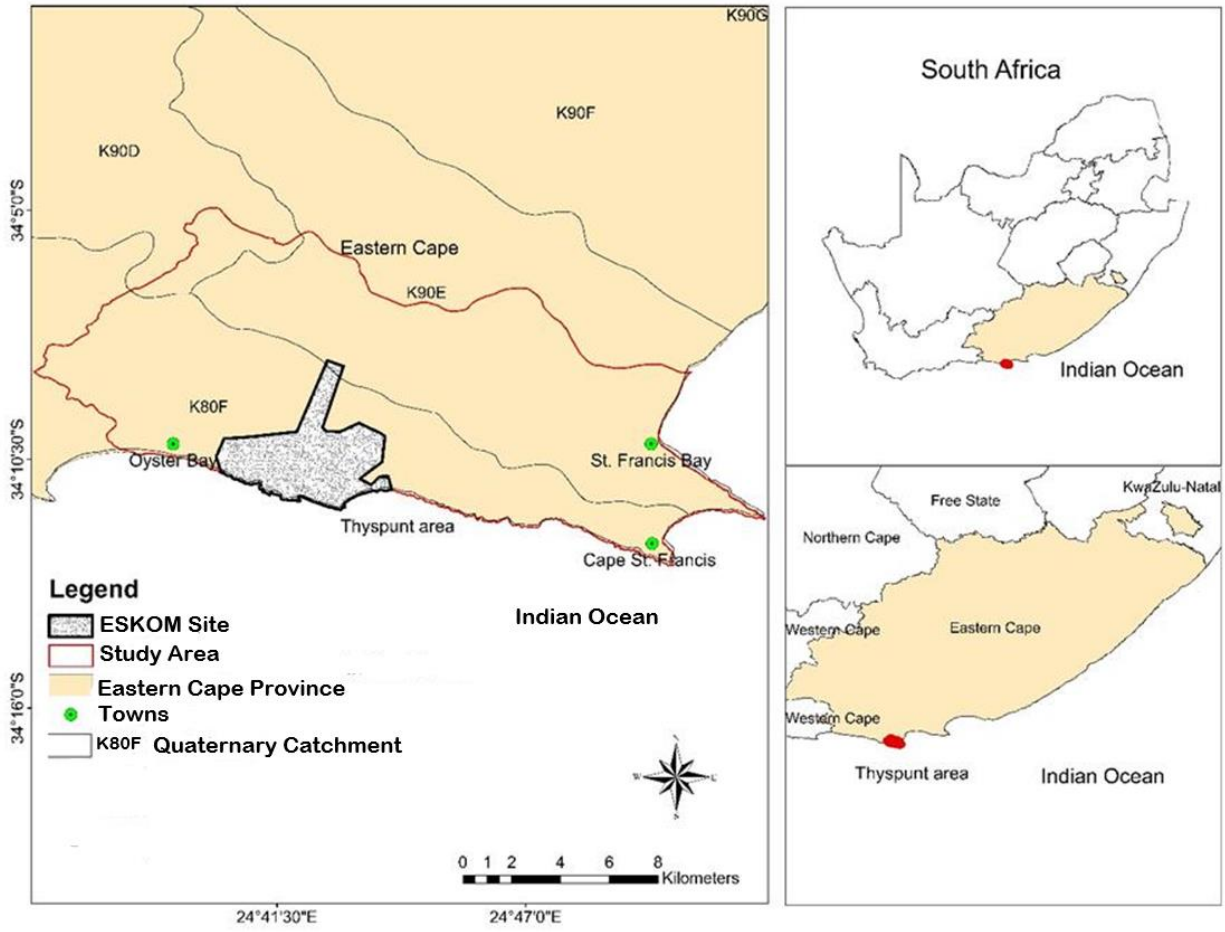

Figure 2.1. Locality map of the study area.

2.2 Climate

The Thyspunt area generally experiences higher rainfall during the summer period (October to March), although winter rainfall does occur (see Figure 2.2). The mean annual rainfall for the area is 621.47 mm. The lowest and highest annual rainfall over 18 years recording period (2000 –2018) are 302 mm (2017) and 935 mm (2011), respectively. The average monthly wind speed is in the range 4.24 – 50.75 m/s, with an average monthly speed of 8.09 m/s (see Figure 2.3). The temperature record

shows seasonal variability, a common phenomenon in temperate regions like Thyspunt. The lowest temperatures are typically experienced during the early hours of winter mornings, with temperatures reaching as low as 4.6°C. However, low temperatures have also been recorded in December and January (3.4°C). High temperatures are typically experienced in December to March, with the highest temperature of 36.6°C. Average monthly temperature ranges from 14.23 to 27.49 °C (Figure 2.3).

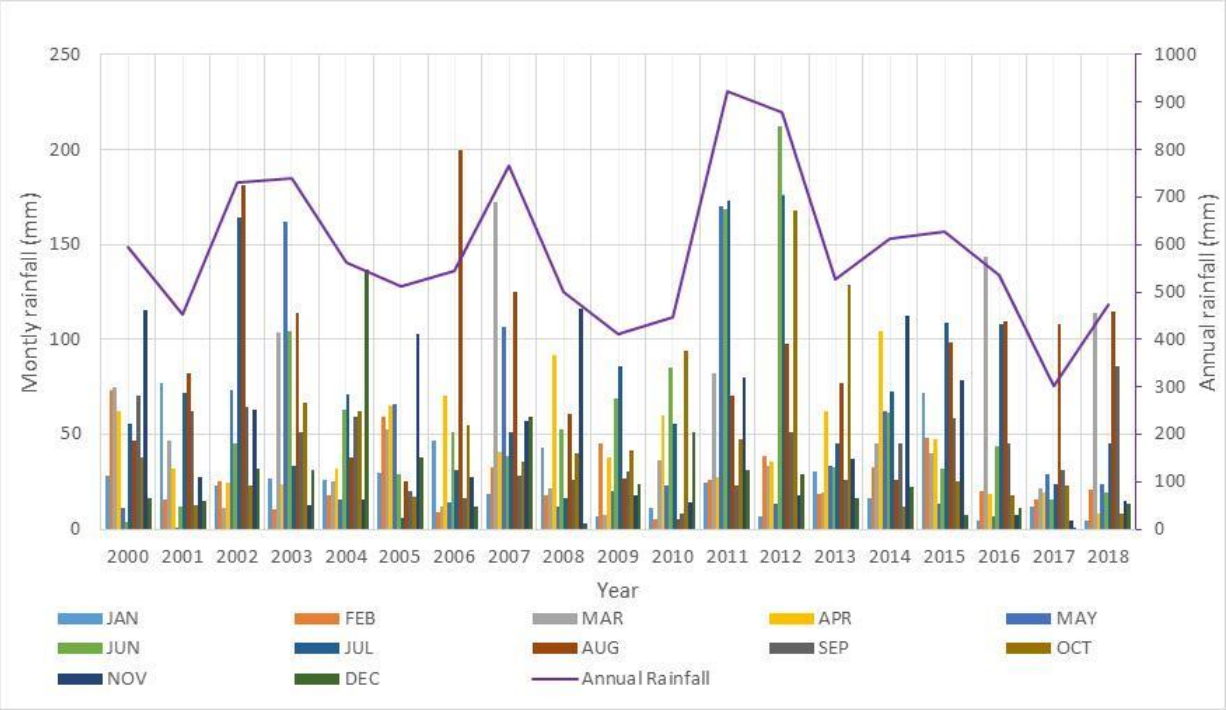

Figure 2.2. Monthly rainfall of Thyspunt.

2.3 **Topography and Drainage**

The topographical setting of the area is shown in Figure 2.4 in the form of a digital elevation model (DEM) with 30 m resolution. The highest elevation is in the central-western parts of the area, where lithologies of the Table Mountain Group (TMG) form topographic highs due to their highly resistant nature to weathering and erosion. Elevation generally decreases away from the topographic highs at the centre of the study area, to sea level towards the coast.

2.4 Land use and Cover

Agricultural activity is the dominant land use activity in the area (Figure 2.6). Most of agricultural activities occur on the north and northwestern part of the Thyspunt area, with less agricultural activity in the eastern part of Thyspunt. The lack of agricultural activity in the southeastern part of Thyspunt is a result of the presence of dune deposits, coastal and shallow marine indurated sediments of the Algoa Group.

There are a number of nature conservation areas around the study area, with the largest nature conservation being Thyspunt Natural Heritage Site followed by Cape St. Francis Nature Reserve, Seal Bay Nature Reserve, Seal Point Private Reserve and Irma Booysen Flora Reserve, respectively. There are few rural settlements around the study area most the people depend on farming and uses groundwater. The Oyster Bay and Cape St. Francis villages are located along the coastal area within the study area.

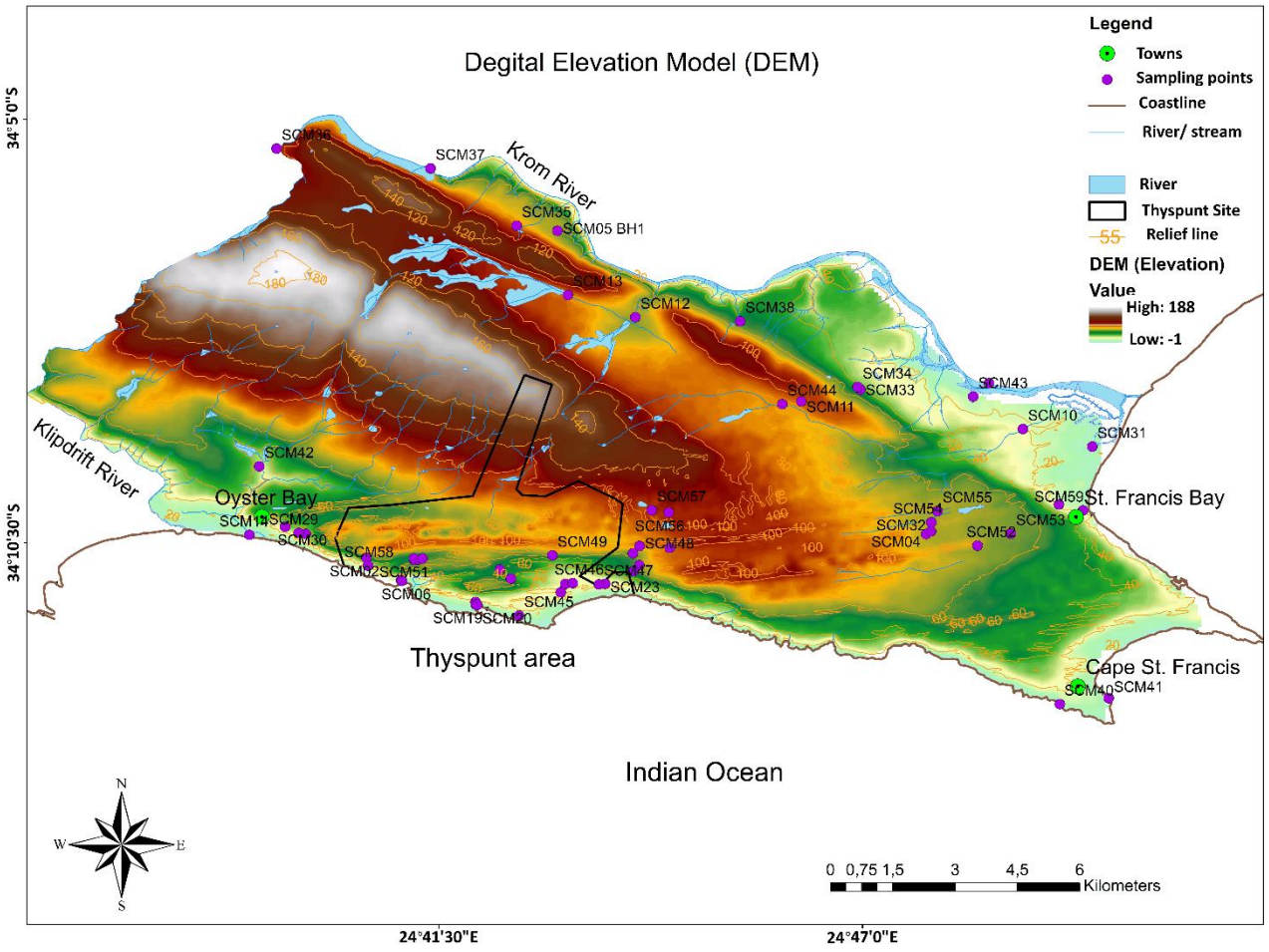

Figure 2.3. Topographic map of the study area in the form of DEM. Note the sampling locations in relation to the surface elevation

3. METHODOLOGY

Several approaches were followed in this research project that can better support the understanding of the hydrogeological system of the area. These include field investigations (geological and hydrogeological mapping), sample collection, laboratory analyses and desktop investigations, including meteorological parameter estimations, aquifer property estimations through pumping test analyses and groundwater vulnerability to pollution mapping. Only one round of field investigation and sample collection was undertaken, and this took place from the 20th to 30th of August 2018.

3.1 Desktop investigations

Desktop study of the geological setting of Thyspunt was undertaken prior to and after the field campaign that took place from the 20th to 30th of August 2018. All meteorological data, including air temperature, rainfall, wind speed and wind direction were obtained from the NNR. Additional rainfall data for the 1980 – 2018 period was acquired from the South African Weather Service (SAWS). The meteorological data have been used for evapotranspiration and recharge estimations, and are detailed below. Evapotranspiration was determined using two techniques.

The Thornwaite and Mather method (Equation 1) was used to determine the potential evapotranspiration (PET), and is calculated as:

$$PET_m = 16\,N_m \left(\frac{10\,\bar{T}_m}{J} \right)^a mm$$

(Equation 1)

Where:

$a = 6.75 \times 10^{-7} J^3 - 7.71 \times 10^{-5} J^2 + 1.792 \times 10^{-2} J + 0.49239$

$J = \sum j_m = \sum (\check{T}_m/5)^{1.514}$

N_m is monthly adjustment factor depending on the season and latitude

m = months in a year 1, 2, ---12

$\check{T}m$ = monthly mean temperature (^0C)

J = the heat index for the year

PET_m = monthly Potential Evapotranspiration

PET was calculated on a monthly basis and summed up to obtain the yearly value. PET represents the maximum evapotranspiration that would take place under ample moisture supply conditions. In

contrast, actual evapotranspiration (AET) is the actual amount of water that has been lost through evapotranspiration. This implies that AET is either less than or equal to the PET of an area.

The AET on annual basis was determined using the Turc method (Equation 2) according to the following equation:

$$AET = P/ [0.9+ (P/L)^{2}]^{½} \text{ mm per annum} \qquad \text{(Equation 2)}$$

Where:

P = mean annual precipitation (mm)

$L = 300 + 25T + 0.05T^3$

T = mean annual Temperature in (^{0}C)

The acquired temperature data spans over a period of two years (2008 and 2009), and, therefore, evapotranspiration was only estimated for 2008 and 2009.

3.2 Field investigations

A field campaign took place from the 20th to 30th of August 2018. A number of data collection activities were undertaken in the field, including ground-truthing of the desktop results, particularly the geology of the area. Details of the field investigation activities are listed in the following subsections.

3.2.1 Geological mapping

The geological mapping of the area was conducted through a desktop study and geological data collection during the fieldwork. A compass clinometer was used to take structural readings in the field, including bedding plane, fractures and joint orientations (Figure 3.1). The features of interest were the strike, dip angle, dip direction and trend of the observed structures. Rock, soil and water samples were also collected for geochemical and radionuclide analyses. Field data and those recorded from desktop investigations were then used to produce a geological cross-section that can better explain the stratigraphic sequence of the rocks.

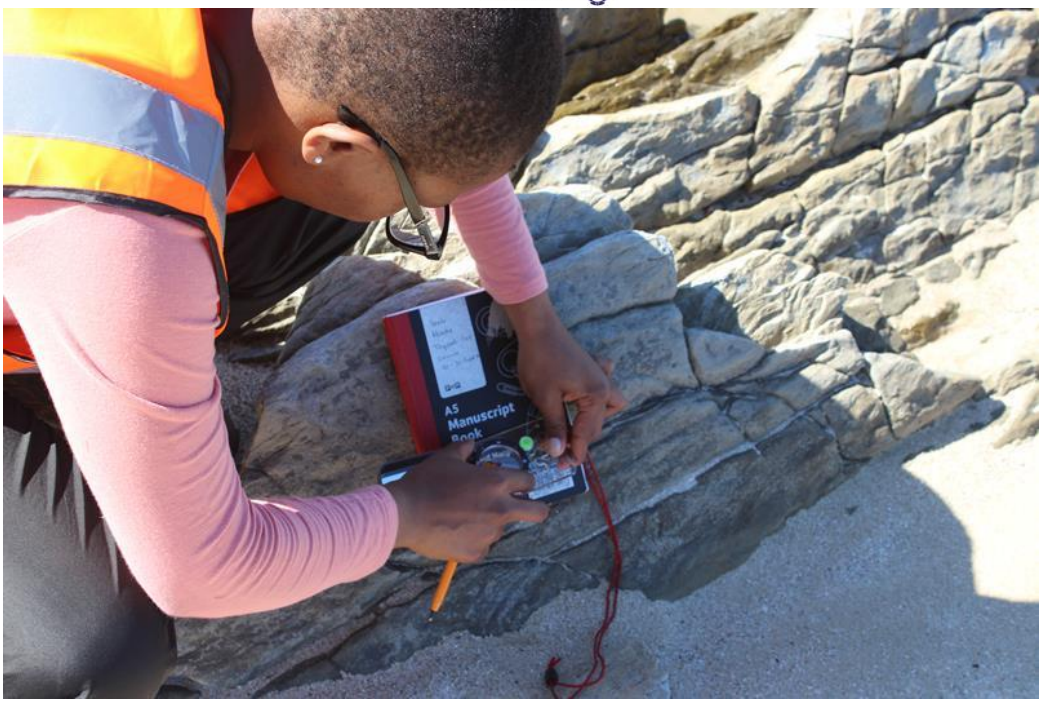

Figure 3.1. Strike and Dip measurement (Courtesy: Prof. Tamiru Abiye)

3.2.2 Hydrogeological investigation

Field based observations coupled with existing data obtained from NNR were used to characterise the hydrogeology of the area. Groundwater level measurements were taken using a dip and TLC meters, in order to verify and ensure high quality water level data. Geological logs of the boreholes obtained from the NNR were examined to determine the type of aquifers present in the area. Pumping test data recorded during or shortly after the drilling of the boreholes were used to determine the hydraulic properties of the aquifers, such as hydraulic conductivity, transmissivity and storativity. Detailed explanations on the pumping test data analyses to determine the aquifer properties are presented in subsection 3.4.1.

Recharge was calculated using the Water Table Fluctuation (WTF) method (Equation 3) (Xu and Beekham, 2003). This technique is best applied to areas with shallow water tables that show sharp rise and decline in groundwater levels. The method operates under the assumption that any rise in groundwater level of an unconfined aquifer is a result of the addition of recharging water to the aquifer. The WTF approach was chosen because of the characteristic shallow water table in the area. This method provides point recharge for an area and hence, is suitable for understanding the recharge conditions. The WTF recharge estimate is a function of the specific yield and changes in groundwater level over time, and is therefore, calculated as:

$$R = S_y \frac{\Delta h}{\Delta t} \qquad \textit{(Equation 3)}$$

Where:

S_y = *specific yield (determined from pump tests)*

Δh = *change in water level*

Δt = *observation time*

Water level monitoring data collected over a two-year period; 2008-2009 for borehole THY-MR5 and 2012 – 2013 for borehole THY-RP2, were supplied by NNR, and these data were used in determining the groundwater recharge over the specified periods. Continuous groundwater level measurements have not been taken after 2013, hence, only water level data from the two years were used. The specific yield was determined from the pumping test data. Recharge estimates are based on data from boreholes THY_RP2, THY_MR5 and THY_RP11. These boreholes were selected for three reasons, namely, they were drilled in the unconfined aquifers; have relatively good pumping test data and hence, have specific yield information. Periods of groundwater level increase were used to estimate the recharge amount.

3.2.3 Infiltration tests

Five infiltration tests were conducted in the field using a double-ring infiltrometer (Figure 3.2) in order to determine the infiltration rate /capacity of the soils and eventually to determine the recharge condition. The test locations were chosen on both the Thyspunt site and the outside areas. Water was dispensed into both rings, and the change in water level in the inner ring was measured against time using a stopwatch. The tests were stopped when the water level in the inner ring remained constant overtime, indicating water saturation of the soil. The results were then tabulated and used to determine the infiltration rate and total infiltration.

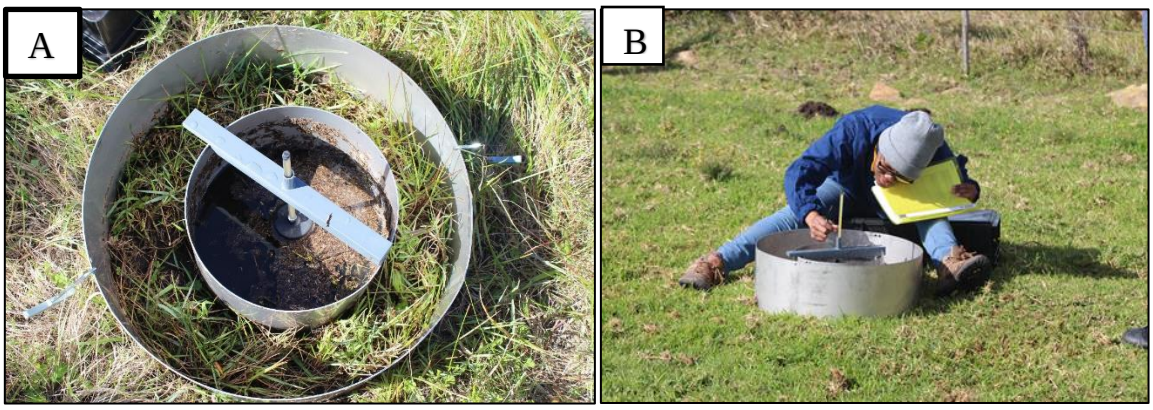

Figure 3.2. a) Double-ring infiltrometer used to determine soil infiltration rates. b) Field-based infiltration test. (Courtesy: Prof. Tamiru Abiye)

3.2.4 Water sampling

Fifty-five water samples were collected from different sources across the study area, including boreholes, springs, rivers, reservoir, wetlands and rain (Figures 3.3 to 3.5). All boreholes were purged for at least 5 minutes prior to sampling with a low-flow sampling pump. This was intended to remove stagnant water from the borehole column, and thus allow for the sampling of water flowing directly from the aquifer. Water quality parameters such as water temperature, pH, electrical conductivity (EC), oxidation-reduction potential (ORP) and total dissolved solids (TDS) were determined in the field during sampling. This was done for accurate determination of the physico-chemical parameters that are representative of the water source. Measurements were taken using the ACCSEN and Crison multiparameter probes and the instruments were calibrated with buffer solution based on the manufacturer guideline every morning before measurement. Onsite field titration using the Fixed Endpoint method was conducted to determine total alkalinity (TAL), HCO_3^- and CO_3^{2-} composition of surface and ground water. The Fixed end point (pH 8.3 and 4.5) method gives double the inflection point method.

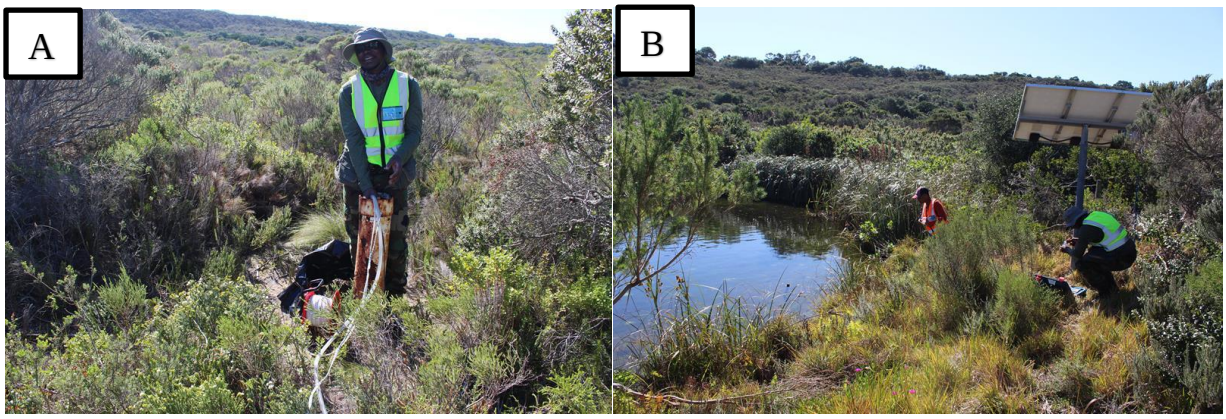

Figure 3.3. A) Borehole sampling after purging. B) Wetland sampling (Courtesy Prof. Tamiru Abiye)

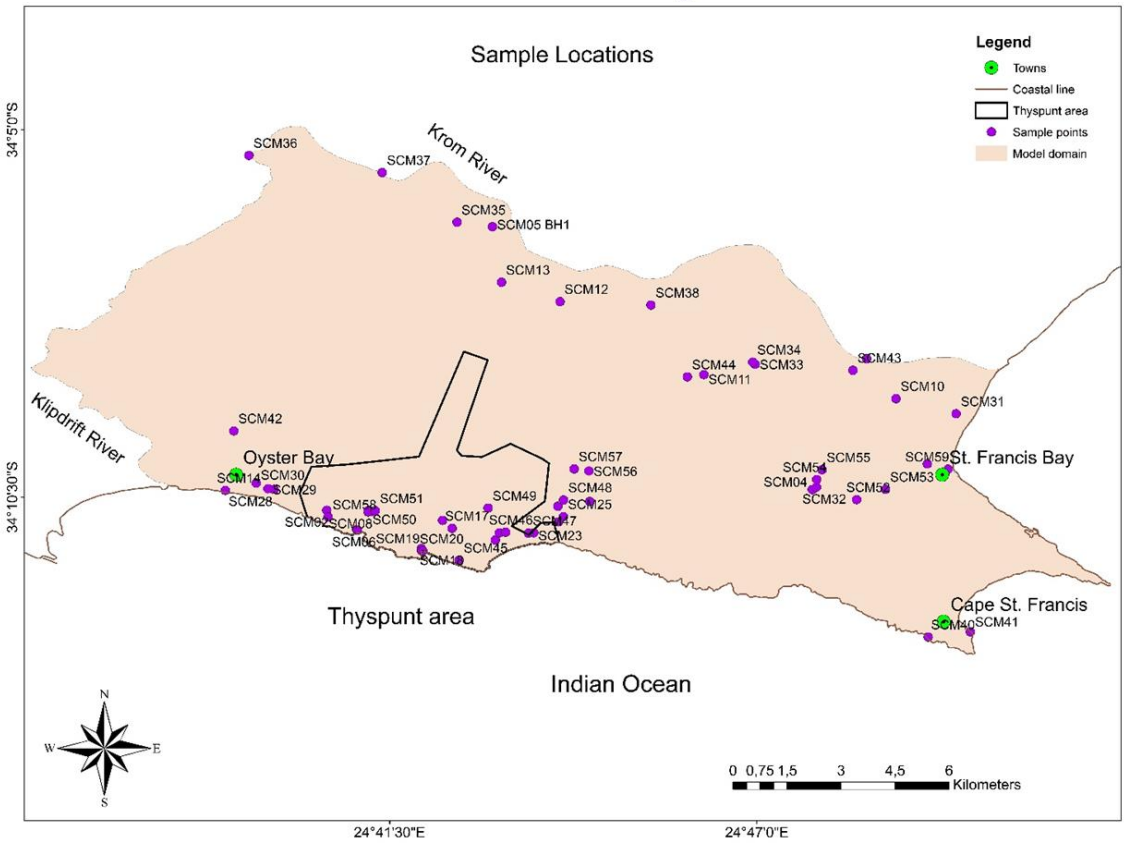

Figure 3.4. Water sampling points (Courtesy: Moneri Modiba)

Figure 3.5 A) Total Alkalinity titration B) Onsite parameter measurements with CRISON multimeter probe (Courtesy: Prof. Tamiru Abiye)

3.3 Laboratory analyses

3.3.1 Hydrochemistry

Forty-one water samples were collected from different water sources, in order to carry out hydrochemical analysis. Fourteen samples were analysed for major ions and twenty seven water samples analysed for metals. These parameters were analysed at the University of Kwa-Zulu Natal

using a Dionex IC instrument and the University of Stellenbosch Analytical Facility, using ICP_AES and ICP-MS, respectively.

3.3.2 Environmental isotopes

Fifty-nine stable isotope (^{18}O and ^{2}H) water samples were collected in the field. Thirty one of the samples were from monitoring boreholes, 11 from springs, 3 rainfall, 2 river samples, 3 seawater and 10 wetland samples. These samples were analysed using the Liquid Water Isotope Analyser (LWIA) model 45-EP laser machine in the Hydrogeology Lab at the University of the Witwatersrand. The stable isotopes of oxygen and hydrogen are very useful tools for deciphering the origin/ source of water, and this is done with the aid of a meteoric water line (MWL). For the purpose of this study, the local meteoric water line of the Sandveld Station ($\delta^2H = 5.8\delta^{18}O + 5.2‰$, Van Wyk, 2010) and the Global Meteoric water Line ($\delta^2H = 8\delta^{18}O + 10‰$, Craig, 1961) were used for the interpretation of the results. Thirty three tritium samples were collected in 1L PVC bottles from different water sources, and submitted to the NRF iThemba Labs for analyses. Tritium is crucial for relative dating of water, as it gives a relative residence time of water below the surface. Residence times were only for groundwater sample because the water is separated from the atmosphere, from where the tritium originates. The mean residence times were determined according to Equation 4 (Clark and Fritz, 1997):

$$t = -17.93\ln\left(\frac{at^{3}H}{a0^{3}H}\right) \qquad (\textit{Equation 4})$$

Where:

t = mean residence time (MRT) in years

$a_t{}^3H$ = Residual activity remaining after decay overtime

$a_0{}^3H$ = Initial Tritium activity

The tritium activity in the sampled rainfall was used as the initial tritium activity.

^{14}C samples were collected following the stand technique (Figure 3.6), and analysed at iThemba Labs. The ^{14}C results were reported as present modern carbon (pMC). The mean residence time of groundwater was then estimated from the ^{14}C pMC content according to Equation 5 (Clark and Fritz, 1997):

$$t = -8267 ln \frac{A}{A_o} \qquad (\textit{Equation 5})$$

Where, t is MRT of groundwater between the time of recharge until groundwater abstraction, A_o represents the initial ^{14}C activity and A is the final ^{14}C activity measured in percent modern carbon (pMC) (Clark and Fritz, 1997).

Figure 3.6. Sampling for ^{14}C with 60 Litres jar (Courtesy: Prof. Tamiru Abiye).

3.3.3 Rock and soil chemistry sampling

Twelve rock and seven soil samples were collected from different parts of the study area for geochemical analysis. The rock samples were subsequently crushed and milled at the Rock crushing Lab, School of Geosciences. The soil samples were collected from at least 0.5 m deep pit (Figure 3.7), and were dried overnight in a conventional oven, to remove any moisture present in the soil prior to analyses. All prepared samples were submitted to the Earth Lab for trace element and major ions analyses, with ICP-MS and XRF, respectively.

Figure 3.7. Soil sampling

3.3.4 Radionuclide analyses

Seven rock and five soil samples were submitted to the NNR radiation laboratory, to determine the baseline radiation of the study area. The samples were analysed for ^{238}U, ^{234}U, ^{226}Ra ^{210}Pb, ^{235}U, ^{232}Th, ^{228}Ra, ^{228}Th, ^{40}K, Gross Alpha and Gross Beta activities. Additionally, eight unfiltered (raw) groundwater, spring and ocean samples were collected with 1 L high-density plastic bottles. Before analysis, the samples were filtered in the Lab. Concentrations and radiation parameters were determined for ^{238}U, ^{235}U, ^{234}U, ^{226}Ra, ^{224}Ra, ^{223}Ra, ^{90}Sr, Gross alpha and Gross beta.

Thirty-three water samples were also collected for tritium analyses in 1L high-density plastic bottles from purged boreholes. These samples were analysed at the iThemba Labs, Gauteng and the results were presented in tritium units (TU). The results were then converted to Bq/L using the following conversion factor:

$$1TU = 0.0118Bq/L$$

Twenty-seven water samples were analysed for trace metal concentration including uranium, thorium and lead. Major ions and metals, including uranium (U), thorium (Th) and lead (Pb) have also been analysed.

3.4 Data analysis

The major ion data were plotted on the Piper and variation diagrams, to determine the dominant ions in the water and their interrelationship. This ultimately enables one to infer the sources of the ions, and thus the responsible process for their occurrence. The diagrams also give an insight on some of the processes responsible for the hydrochemical characteristics of the water in question, such as mixing of different waters.

3.4.1 Pumping test data analysis

Pumping test data for the Eskom boreholes were obtained from the NNR. These data were used to determine different aquifer properties such as transmissivity and hydraulic conductivity. Unconfined aquifer properties were determined using the modified Fitts Geosolutions software. The Neuman Method serves as the basis of the software. In contrast, the Theis Method was used to determine the aquifer properties of confined aquifers.

Pumping test data from boreholes THY- RP8, THY-RP10, THY-MR2, 5 and 11 were used to determine the unconfined aquifer properties using the Neuman method.

3.5 Groundwater vulnerability to pollution mapping

Groundwater vulnerability refers to the susceptibility of aquifers to pollution. Several methods are available for mapping, but the DRASTIC method was applied in this research as it contains more parameters than other methods. The DRASTIC method was developed by the Environmental Protection Agency of the United States of America in 1983 (Aller *et al.*, 1987).(). DRASTIC method is capable of processing vast amounts of complex database through ARCGIS platform and has proven to be the best-suited model for aquifer vulnerability mapping in regions dominated by agricultural activities and semi-arid climate (Aller *et al.*, 1987 Leyland *et al.*, 2008; Mostert, 2014). Additionally, the method is best-suited for regional applications and the results are presented in a simple, understandable manner (Aller *et al.*, 1987). The DRASTIC model operates on the basis of 4 assumptions: (1) all contaminants are sourced from the land surface; (2) the contaminant is carried into the aquifer by precipitation; (3) the contaminant moves at the same velocity as water; and (4) the area evaluated is at least 0.4 km^2 (Aller *et al.*, 1987). The DRASTIC method is used to evaluate aquifer vulnerability to potential pollution by employing a parametric system (Aller *et al.*, 1987).

The pollution potential, also known as the drastic index is given by Equation 6:

DRASTIC Index (DI) = DrDw + RrRw + ArAw + SrSw + TrTw + IrIw + CrCw *(Equation 6)*

w is the weight (relative importance) of the parameter. The weights range from 1 to 5; with 5 being the most important parameter and 1 being the least important parameter. These weights are fixed and, therefore, remain the same for every DRASTIC application (Aller *et al.*, 1987).

r is the rating of the parameter and varies from 1 to 10. 10 is assigned to the parameter that poses the highest risk and 1 is assigned to the parameter that poses the least risk. Unlike weights, ratings of each parameter are assigned by the researcher and are therefore subjective.

The higher the DI, the higher the potential for groundwater pollution. The computation of DI allows for the identification of areas that are more vulnerable to pollution potential in relation to the rest of the study area. For the purpose of this study, all assigned ratings have been modified.

Data Preparation

The data used to produce the individual parameter maps were obtained from a variety of sources, including own field measurements and investigations. A summary of the different data sources and applications is presented in Table 3.1.

Table 3.1: DRASTIC parameters' data sources

Parameter	Data source	Data type	Application
Depth to groundwater	Field measurements from field work	Numerical (table)	D
Recharge	Department of Water and Sanitation: Resource Quality Information Services (RQIS) http://www.dwaf.gov.za/iwqs/gis_data/river/rivs500k.aspx	Digital	R
Aquifer media	Council for Geosciences: Geological map of the Eastern Cape	Digital	A,I
Soil media	https://data.isric.org/geonetwork/srv/eng/catalog.search#/metadata/c3f7cfd5-1f25-4da1-bce9-cdcdd8c1a9a	Digital	S
Topography	Digital Elevation Model developed by the United States Geological Survey	Digital	T
Impact of vadose zone	Council for Geosciences: Geological map of the Eastern Cape	Digital	A,I
Conductivity (hydraulic)	Determined from pumping test data using the Fitts Geosolution Software. Pumping data provided by the National Nuclear Regulator (NNR)	Numerical (table)	C

Determination of individual parameter maps

Depth to groundwater (**D**)

The depth to groundwater indicates the distance and time required for contaminants to travel through the vadose zone to reach groundwater (Aller *et al.*, 1987). Aquifers with shallow groundwater levels are more vulnerable to pollution relative to deeper groundwater levels. The confining media in a confined aquifer system has very low permeability, therefore, contaminant velocity is very low and confined aquifers are less vulnerable to pollution as compared to unconfined aquifers (Aller *et al.*, 1987). In terms of DRASTIC, the shallow the groundwater level, the higher the vulnerability rating. The ratings associated with different groundwater depth ranges for the study area are presented in Table 3.2.

Table 3.2: Parameter weightings and ratings associated with each range (modified from Aller *et al.*, 1987)

DRASTIC parameter	**Weight**	**Range**	**Rating**
Depth to groundwater (m.b.g.l) D	5	0-5	10
		5-10	9
		10-20	5
		20-30	3
Recharge (mm) R	4	0-60	6
		60-120	8
		120-180	10
Aquifer media A	3	Fractured (quartzite)	7
		Hard rock (shale)	6
		Intergranular	9
Soil media S	2	Sand (arenosol)	9
		Loamy-sand (arenosol)	7
		Sandy clay (plinthosol)	4

Topography: Slope measured as % T	1	0-5	10
		5-10	8
		10-20	5
		20-30	2
Impact of vadose zone I	5	Recent deposits: Alluvium and mobile dunes	10
		Quaternary deposits: Consolidated dunes	9
		Shale	3
		Quartzite	5
Hydraulic Conductivity (m/day) C	3	0.00 - 5	2
		5 - 10	7
		10-15	9
		>15	10

Recharge (**R**)

Groundwater recharge represents the volume of water that infiltrates the ground surface and eventually percolates to reach the groundwater/aquifer. This water thus has the capacity to transport or facilitate the movement of contaminants into the aquifer (Aller *et al.*, 1987). Recharging of unconfined aquifers occurs more readily as opposed to confined aquifers, therefore, the potential for recharge- related pollution is higher in unconfined aquifers (Aller *et al.*, 1987). The higher the recharge value, the higher the vulnerability rating. The different recharge ranges and associated ratings for the Thyspunt area are presented in Table 3.

Aquifer media (**A**)

This represents any consolidated or unconsolidated geological formation with the capacity to bear groundwater and yield sufficient water quantities for a certain use (Aller *et al.*, 1987). Fractures that

occur within rock formations will also be considered as they play a crucial role in providing conduits for contaminant migration in the aquifer. This parameter gives information about the physical properties of the aquifer medium (such as porosity and permeability) in contact with the contaminant. The porosity and permeability influence the path length and route that the contaminant will follow in the aquifer (Aller *et al.*, 1987). Aquifers with higher permeability and hydraulic conductivity (such as alluvial and fractured aquifers) are more vulnerable to groundwater pollution and are thus assigned higher vulnerability ratings. Additionally, confined and deep aquifers are less vulnerable to pollution because the confining units are commonly less permeable and less vulnerable, and contaminants encounter higher travel times and paths and may thus never reach deep aquifers respectively. The different aquifers and associated ratings for the Thyspunt area are presented in Table 3.2.

Soil media (**S**)

This is the upper-most part of the unsaturated zone (Aller *et al.*, 1987). This acts as the first line of defence against contaminants since the contaminants first have to migrate through the soil zone before reaching the aquifer. The thickness and soil type have an effect on the rate of contaminant migration to the groundwater. Aquifers overlain by thin soil zones and/or soils that have a low clay content are therefore more vulnerable to pollution due to the high permeability of the media (Aller *et al.*, 1987). The thinner and clay-poor the soil is, the higher the vulnerability rating. The different soil types and related ratings are presented in Table 3.2.

Topography (**T**)

Topography refers to the variability of the slope of the land surface (Aller *et al.*, 1987). This parameter dictates whether a contaminant will run-off on the land surface or remain on the land surface long enough for infiltration into the subsurface and eventually the groundwater (Aller *et al.*, 1987). The shallow the slope, the higher the potential to infiltrate into the ground surface and thus the higher the vulnerability rating. The different slope ranges and corresponding vulnerability ratings are presented in Table 3.2.

Impact of the vadose zone (**I**)

This is the portion of the subsurface located above the water table where the pore spaces are filled by air and water. The vadose zone has the ability to breakdown contaminants into secondary (and less harmful) products through chemical, biological and physical interactions with material in the aquifer. The characteristics of the vadose zone thus affect the contact time between the contaminants and vadose zone material (Aller *et al.*, 1987). Vadose zones with low porosity, permeability and hydraulic

conductivity are less vulnerable to groundwater pollution and thus assigned lower ratings. The different vadose zone types and related ratings are presented in Table 3.2.

Conductivity (**C**)

This is a measure of the ability of an aquifer to transmit water and affects the flow velocity of groundwater and thus the velocity of the contaminants through the aquifer (Aller *et al.*, 1987). The higher the hydraulic conductivity, the higher the vulnerability to pollution and thus, a high rating is assigned. Hydraulic conductivity ranges and associated ratings are presented in Table 3.2.

Intrinsic aquifer vulnerability map

The intrinsic aquifer vulnerability map was developed using the weighted overlay tool in ArcMap 10.4.1. The weighted overlay tool unifies multiple raster layers via a synonymous measurement scale. Each raster layer may not have the same influence on the outcome, and, therefore, each raster is assigned an influence percentage according to its importance to the final output. The sum of all the influence percentages should equal to 100%. The percentage influence of each layer is multiplied by the scale value (assigned rating), and the products are summed together to generate the outcome. The final output map was rounded off to the nearest integer since the weighted overlay tool is in integer format. The percentage influences were calculated based on the weights assigned to each parameter according to Equation 7. The percentage influence of each parameter is presented in Table 3.3.

$$Percentage\ influence\ \% = \frac{weighting}{weighting\ sum}\ x\ 100 \qquad (Equation\ 7)$$

Table 3.3: Percentage influence ratings for each DRASTIC parameter

Parameter	Weighting	Percentage influence (%) – rounded to the nearest whole number
D	5	22
R	4	17
A	3	13
S	2	9
T	1	4
I	5	22
C	3	13
Total	**23**	**100**

4. RESULTS AND DISCUSSION

4.1 Evapotranspiration

The estimated evapotranspiration values are presented in Table 4.1. The 2009 PET is higher than the 2008 PET values. However, the AET value has decreased from 2008 to 2009, which could be due to decrease in ambient temperature and increase in rainfall. Effective rainfall (difference between annual rainfall and PET) for both years is negative, indicating a rainfall deficit over the two-year period. This implies that theoretically, all rainfall is lost through evapotranspiration and thus, no water is available for infiltration (and recharge) and runoff. A water balance for the two years would yield a negative change in storage. In reality, this may not be the case. There are many other factors that controls recharge from rainfall.

4.2 Geological Setting

The Table Mountain Group rocks covers most parts of the surface geology of the study area, as shown in Figure 4.6 . The Precambrian rocks of the Gamtoos Group and the Cape Granites do not outcrop in the Thyspunt area, but rather form the basement to the surface geology (DWA, 2010; DEA, 2016). The Peninsula Formation, which is the oldest of the five formations of the TMG, is characterised by quartzite, sandstone and shale (Claassen, 2014), which constitutes the base of the geology in the area. The TMG rocks form an anticline with the Peninsula Formation at its core. Field outcrops of this formation are characterised by alternating ridges of sandstones and/or quartzites and shale dominated flatlands. Overlying the Peninsula Formation is the shale-dominated Cedarburg Formation. Analogous to the shales of the Peninsula Formation, the Cedarburg Formation forms laterally extensive flatlands due to weathering. The Goudini, Skurwerburg and Baviaanskloof Formations collectively make up the Nardouw Subgroup. Meta-sandstone, quartzite and minor shales constitute the Goudini Formation. The Skurwerburg Formation comprises grey-white, cross-bedded and intensively fractured quartzite, outcropping along the coast of the Thyspunt area as shown in Figure 4.1. The dip direction varies from the southwest to the northeast towards Cape St. Francis. The change in dip direction over a relatively small scale is indicative of substantial folding. This is further supported by the intensely deformed nature of the local geology. Randomly oriented fractures, which occasionally host quartz veins, are ubiquitous in the coastal quartzite outcrops. Muddy shales are characteristic lithologies of the Baviaanskloof Formation (Claassen, 2014). The main rock outcrops in the area are presented in field pictures given in Figures 4.1 to 4.5.

Table 4.1: Monthly and Annual Potential Evapotranspiration and Actual Evapotranspiration estimates of Thyspunt.

Months	Jan_2008	Feb_2008	Mar_2008	Apr_2008	May_2008	Jun_2008	Jul_2008	Aug_2008	Sep_2008	Oct_2008	Nov_2008	Dec_2008	Annual PET	Annual AET:2008
PET (mm)	98.5	91.9	82.2	59.1	59.1	39.7	39.2	45.2	44.6	60.1	71.7	89.6	780.907	476.478
Months	Jan_2009	Feb_2009	Mar_2009	Apr_2009	May_2009	Jun_2009	Jul_2009	Aug_2009	Sep_2009	Oct_2009	Nov_2009	Dec_2009	Annual PET: 2009	Annual AET: 2009
PET (mm)	88.6	90.8	79.5	66.9	50.4	39.5	44.2	134.8	52.1	70.6	66.6	78.1	821.514	595.384

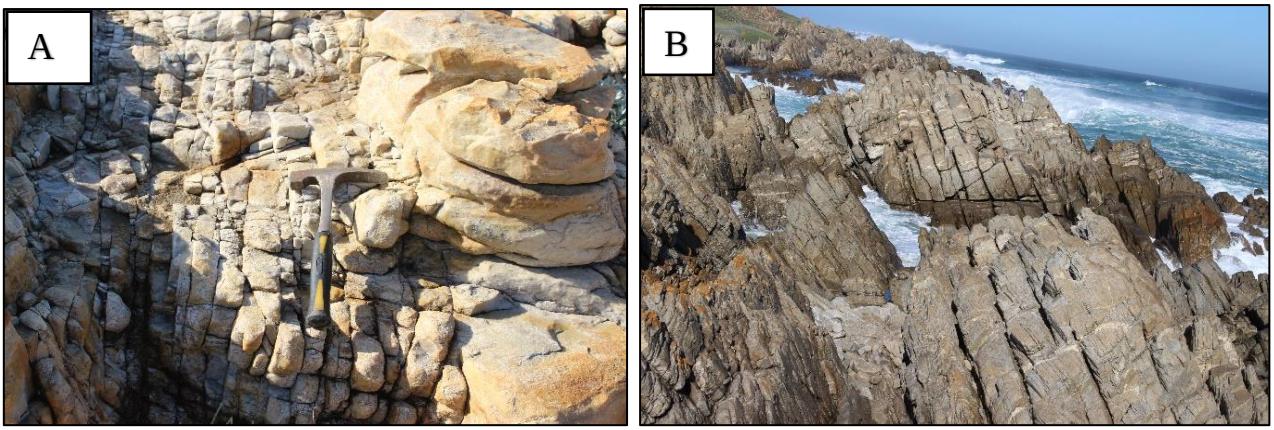

Figure 0.1. a) Highly fractured quartzite coastal outcrops of the Skurwerburg Formation in Thyspunt. b) Skurwerburg Formation quartzite along the coast (Courtesy: Prof. Tamiru Abiye).

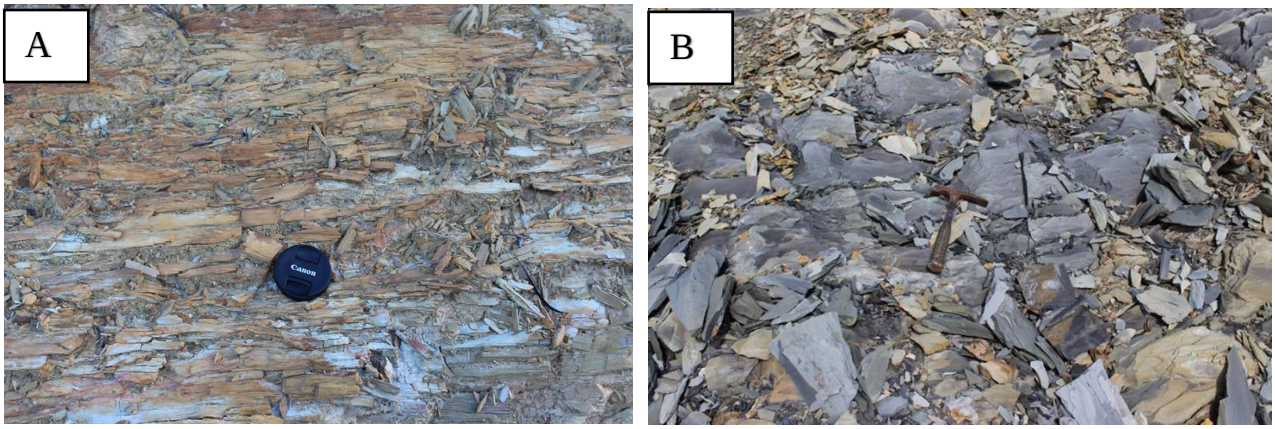

Figure 4.2. A) Ceres Subgroup shale B) Baviaanskloof Formation (Organic shale from a quarry) (Courtesy: Prof. Tamiru Abiye).

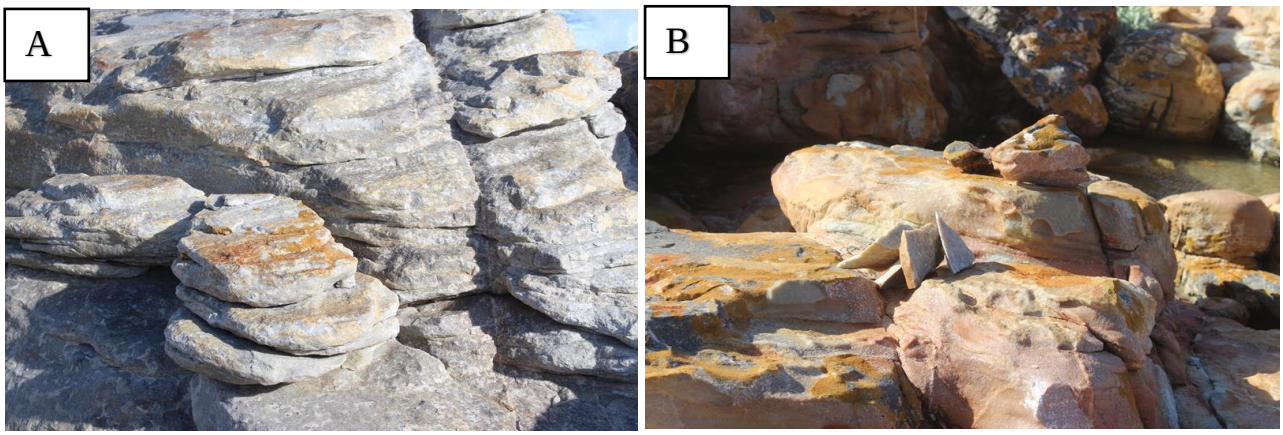

Figure 4.3. A) Peninsula Formation quartzite B) Peninsula Formation ferruginous quartzite (Courtesy: Prof. Tamiru Abiye).

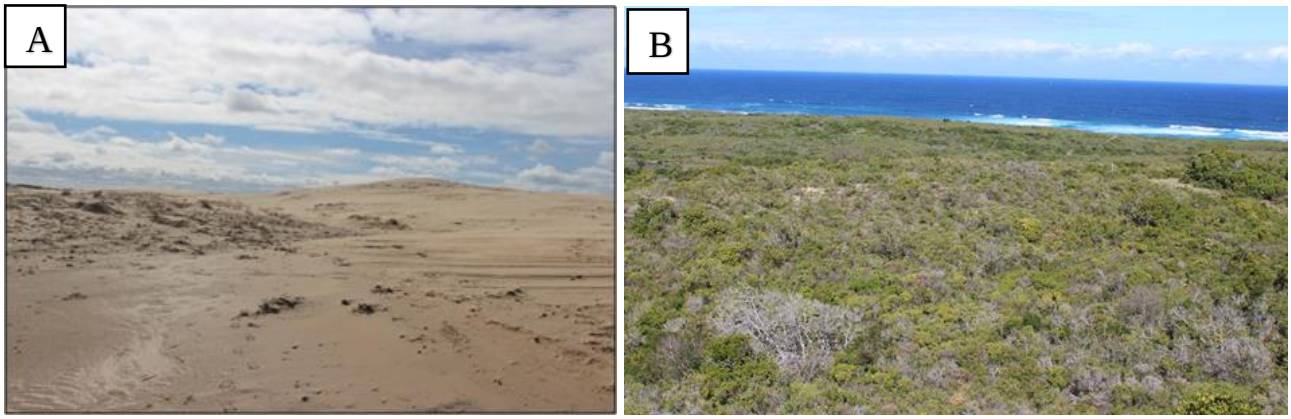

Figure 4.4. A) Extensive mobile dunes and B) The footprint area as seen from the meteorological station, covered by dunes and Fynbos vegetation (Courtesy: Prof. Tamiru Abiye).

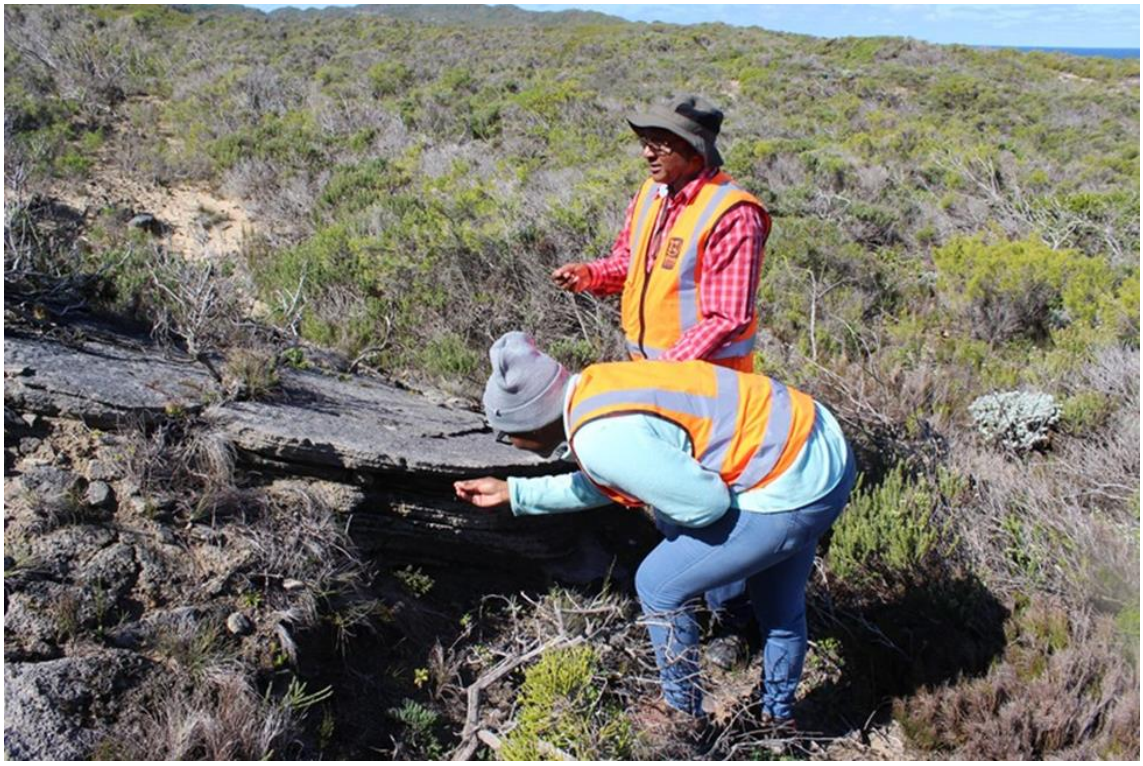

Figure 4.5. Indurated sediment of the Algoa Group (Courtesy: Prof. Tamiru Abiye)

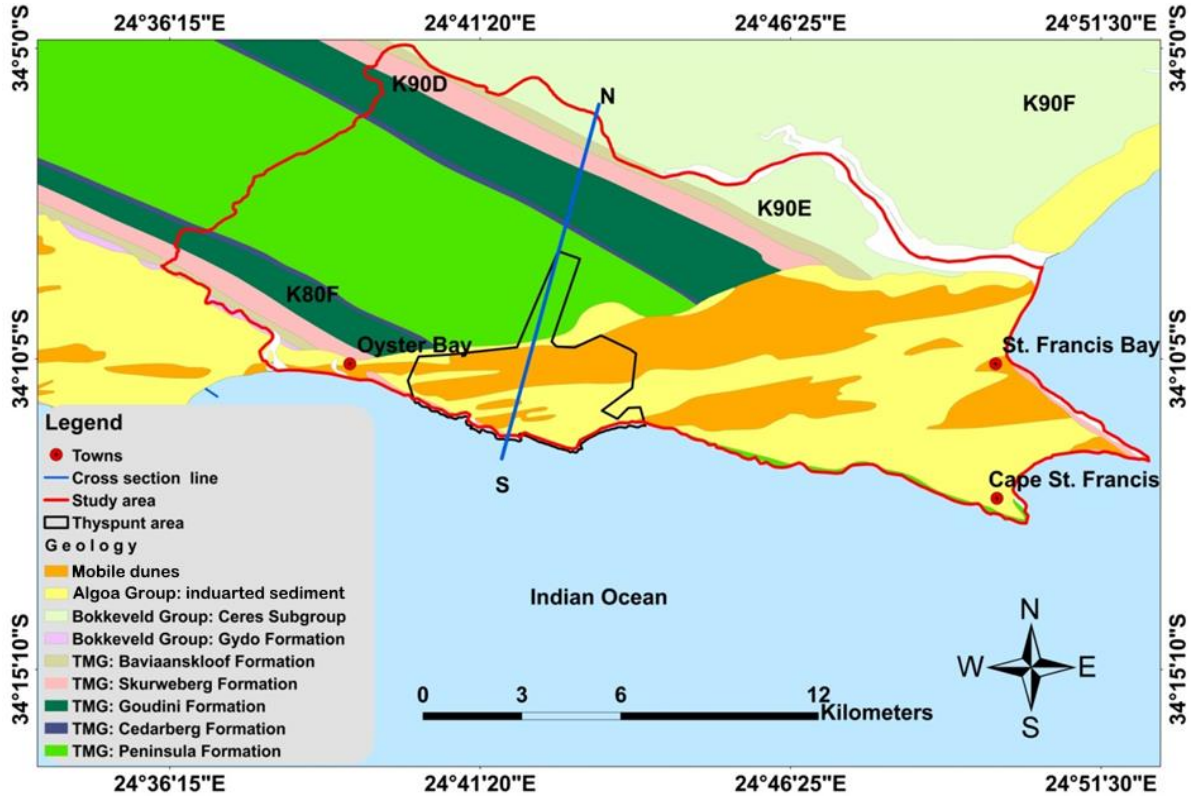

Figure 4.6. Geological map of Thyspunt area. Note N-S sectional line used for cross-section construction

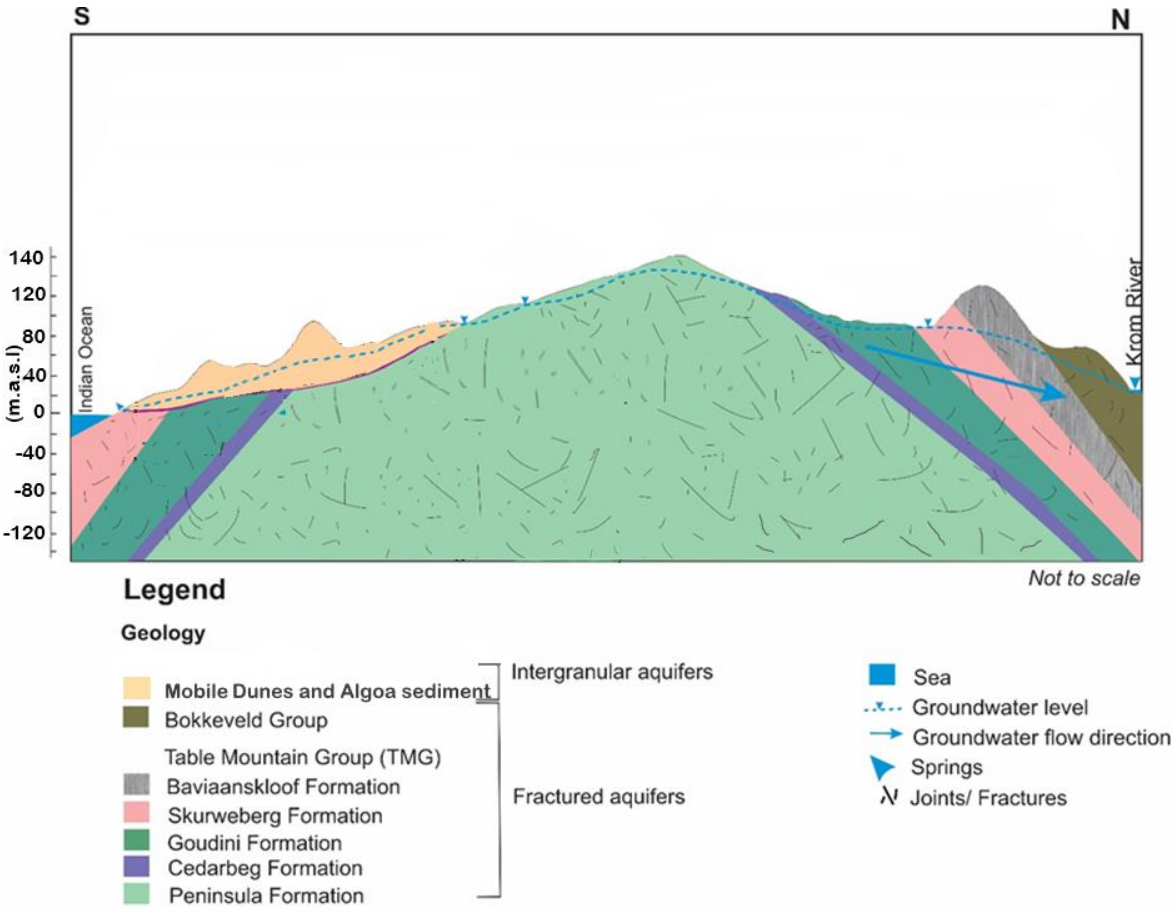

Figure 4.7. Geological cross-section from S to N direction

Field and desktop studies indicate the presence of extensive and intense folding of the rocks that expands far away from the area due to regional nature of the ductile tectonics. A regional anticline extends over the majority of the surface geology where the rocks are aligned NW-SE (Figure 4.7). The fold axis is located on the Peninsula Formation, the oldest geological unit in the area. The younging direction of the lithologies is away from the centre of the fold (Peninsula Formation). Local scale folding is indicated by the change in the dip direction of the Peninsula quartzite over a relatively small area. The quartzites dip to the southwest in Oyster Bay and Thyspunt, whilst they dip to the northeast in Cape St. Francis area. Similarly, the change in dip direction of the Goudini Formation lithologies is indicative of folding (see Table 4.2).

Table 4.2. Structural data of different geological formations in Thyspunt.

Formation	Rock type	Strike	Dip (°)	Dip direction
Skurwerburg	Quartzite	165	53	SW
Baviaanskloof	Shale	178	55	E
Peninsula	Quartzite			SW
Peninsula	Meta-sandstone			NE
Skurwerburg	Sandstone	170	54	SE
Peninsula	Quartzite	156	61	SW
Peninsula	Quartzite	171	48	SE
Peninsula	Quartzite	180	56	SW
Ceres Subgroup	Shale	179	44	NE
Peninsula	Quartzite	152	16	NE
Peninsula	Quartzite	71	12	SE
Peninsula	Quartzite	175	28	NE
Peninsula	Sandstone			SW
Skurwerburg	Quartzite	167	32	SE

4.3. Hydrogeological conditions

4.3.1 Aquifer characterisation

Two types of aquifers have been identified in the study area (Table 4.3).

Confined aquifers

Based on the position and occurrence of artesian boreholes, the confined aquifer in the area is inferred to be located within the Goudini Formation (quartzite and shale) of the TMG, and is covered by the Skurwerburg quartzite dipping to the north. Confined aquifers made of dipping quartzite also occur along the coastal part of the study area. Siltstone and /or shale of the Table Mountain Group act as confining units to the fractured aquifers, and vary in thickness. The depth to groundwater levels in the area range from 4.43 to 28.87 m.b.g.l. The confined aquifer thickness ranges between 18 and 126.96 m (Table 4.3).

Table 4.3: Aquifer properties determined from drilling logs and pumping test analyses of 11 boreholes using the Fitts Geosolutions software

Borehole ID/ Name	**Fitts Geosolutions determined aquifer properties**				**Aquifer thickness**	**Aquifer type**	**Lithostratigraphic unit**
	Transmissivity (T)	**Storativity**		**Hydraulic conductivity (K)**			
	(m2/d)	**S**	**Sy**	**(m/d)**	**(m)**		
THY-RP1	1.454	1x10-3		0.0115	126.96	Confined	TMG
THY-RP2	39.01	3.75x10-4	0.1	0.5135	75.97	Confined	TMG
THY-RP5	44.01	1.0x10-3		0.320	138	Confined	TMG
THY-RP6	37.99	5.0 x10-5		1.5829	24	Confined	TMG
THY-RP8	36.81		0.0059	0.327	112.4	Unconfined	TMG
THY-RP14	15.04	1.69x10-3		0.8356	18	Confined	TMG
THY-RP10	2.506		0.04534	0.0440	57	Unconfined	TMG
THY-RP9	4.562	3.0x10-2		0.0670	68	Confined	TMG
THY-MR2	108.3		0.116	4.4734	24.21	Unconfined	ALGOA
THY-MR5	275		1.47x10-2	19.13	12.85	Unconfined	MOBILE DUNES
THY-RP11	0.359	1.0x10-5		0.0089	40.28	Confined	TMG
THY-MR11	125.1		0.1	7.7222	16.2	Unconfined	ALGOA

The transmissivity of the confined aquifers, which is the ability of the aquifer to transmit water across its entire thickness, ranges between 0.359 and 44.01 m^2/day, indicating variable transmission properties of the aquifers commensurate with variations in thickness and hydraulic conductivity. The lowest aquifer transmissivities are determined at boreholes THY-RP1, 9, 10 and 11. At least three artesian boreholes were recorded during the fieldwork in the study area (e.g. Figure 4.8). The TMG quartzite acts as a confined aquifer, and is covered by shale. The aquifers are characterised by iron and chloride-rich water with an average discharge rate of 3500 L/hour.

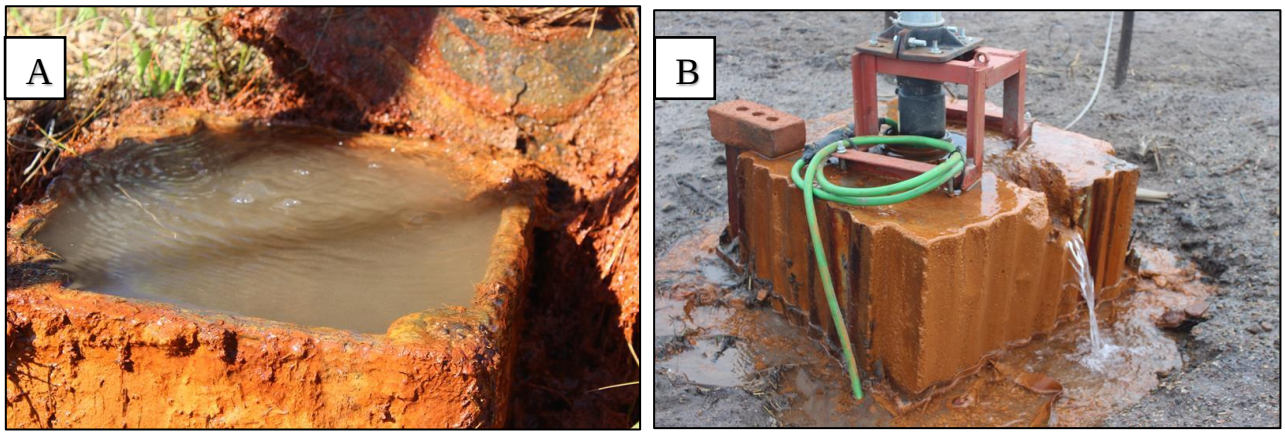

Figure 4.8. A) Artesian borehole in the area B) Iron-rich groundwater discharging from an artesian borehole (Courtesy: Prof. Tamiru Abiye).

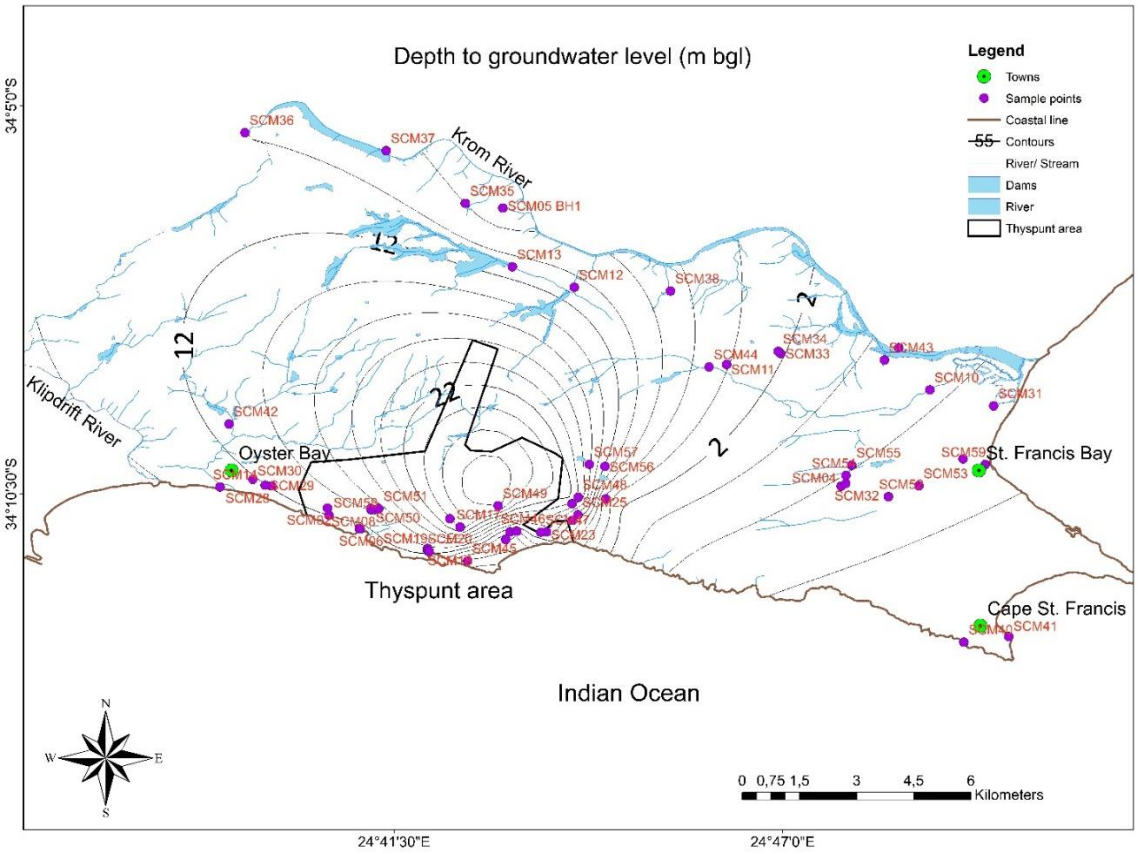

Figure 4.9. Depth to groundwater level map of Thyspunt (Courtesy: Moneri Modiba).

Table 4.3: Aquifer properties determined from drilling logs and pumping test analyses of 11 boreholes using the Fitts Geosolutions software

Borehole ID/ Name	**Fitts Geosolutions determined aquifer properties**				**Aquifer thickness**	**Aquifer type**	**Lithostratigraphic unit**
	Transmissivity (T)	**Storativity**		**Hydraulic conductivity (K)**			
	(m^2/d)	**S**	**Sy**	**(m/d)**	**(m)**		
THY-RP1	1.454	$1x10^{-3}$		0.0115	126.96	Confined	TMG
THY-RP2	39.01	$3.75x10^{-4}$	0.1	0.5135	75.97	Confined	TMG

THY-RP5	44.01	$1.0x10^{-3}$		0.320	138	Confined	TMG
THY-RP6	37.99	$5.0 x10^{-5}$		1.5829	24	Confined	TMG
THY-RP8	36.81		0.0059	0.327	112.4	Unconfined	TMG
THY-RP14	15.04	$1.69x10^{-3}$		0.8356	18	Confined	TMG
THY-RP10	2.506		0.04534	0.0440	57	Unconfined	TMG
THY-RP9	4.562	$3.0x10^{-2}$		0.0670	68	Confined	TMG
THY-MR2	108.3		0.116	4.4734	24.21	Unconfined	ALGOA
THY-MR5	275		$1.47x10^{-2}$	19.13	12.85	Unconfined	MOBILE DUNES
THY-RP11	0.359	$1.0x10^{-5}$		0.0089	40.28	Confined	TMG
THY-MR11	125.1		0.1	7.7222	16.2	Unconfined	ALGOA

Unconfined aquifers

Coastal deposits of the Algoa Group, mobile sand dunes and weathered and fractured quartzite and sandstone of TMG constitute the unconfined aquifers. These aquifers overlie the confined aquifers in certain areas and are characterised by shallow groundwater levels, with minimum depth to groundwater level of 3.5 m.b.g.l. The thickness of unconfined aquifers made of coastal deposits of Algoa Group ranges from 12.85 to 24.21 m. In contrast, unconfined aquifers composed of quartzites of the TMG are generally thicker than those of the Algoa Group and mobile dunes with thickness that vary between 57 and 112.4 m. The notable difference in aquifer thickness is likely a result of the resistant to weathering of the TMG quartzite that helps preserve the thickness of the aquifers. Moreover, the majority of the Algoa Group sediments and the mobile dunes are unconsolidated, surficial deposits and are, therefore, prone to erosion that reduced the thickness of the deposits and aquifers. Hydraulic conductivity falls between 0.0440 and 19.13 m/day. Higher values are related to the Algoa Group and dune aquifers, which could be due to porous nature of the deposits coupled with the interconnected pores that permit the flow of water through the deposits. The estimated transmissivity values for unconfined aquifers range from 36.81 to 275 m^2/day, with Algoa Group aquifers containing transmissivities of at least 108 m^2/day. This could be explained by the relatively elevated hydraulic conductivities of the dunes and Algoa Group aquifers (Table 4.3).

4.3.2 Groundwater levels and flow direction

Based on the groundwater flow direction constructed from the groundwater level map of the study area (Figure 4.10), the general groundwater flow direction is from west to east, towards the Indian Ocean. A portion of the study area acts as a recharge zone, as indicated by the diverging groundwater flow lines. This recharge area is located on the mobile dunes within the Eskom site. Two wetland systems are located around the recharge area, one of which has an elevated electrical conductivity

value of about 7040 µS/cm, which might be due to excessive evaporation and lack of dilution by groundwater. This observation, together with the isotope results indicates the dominance of regional recharge in the study area.

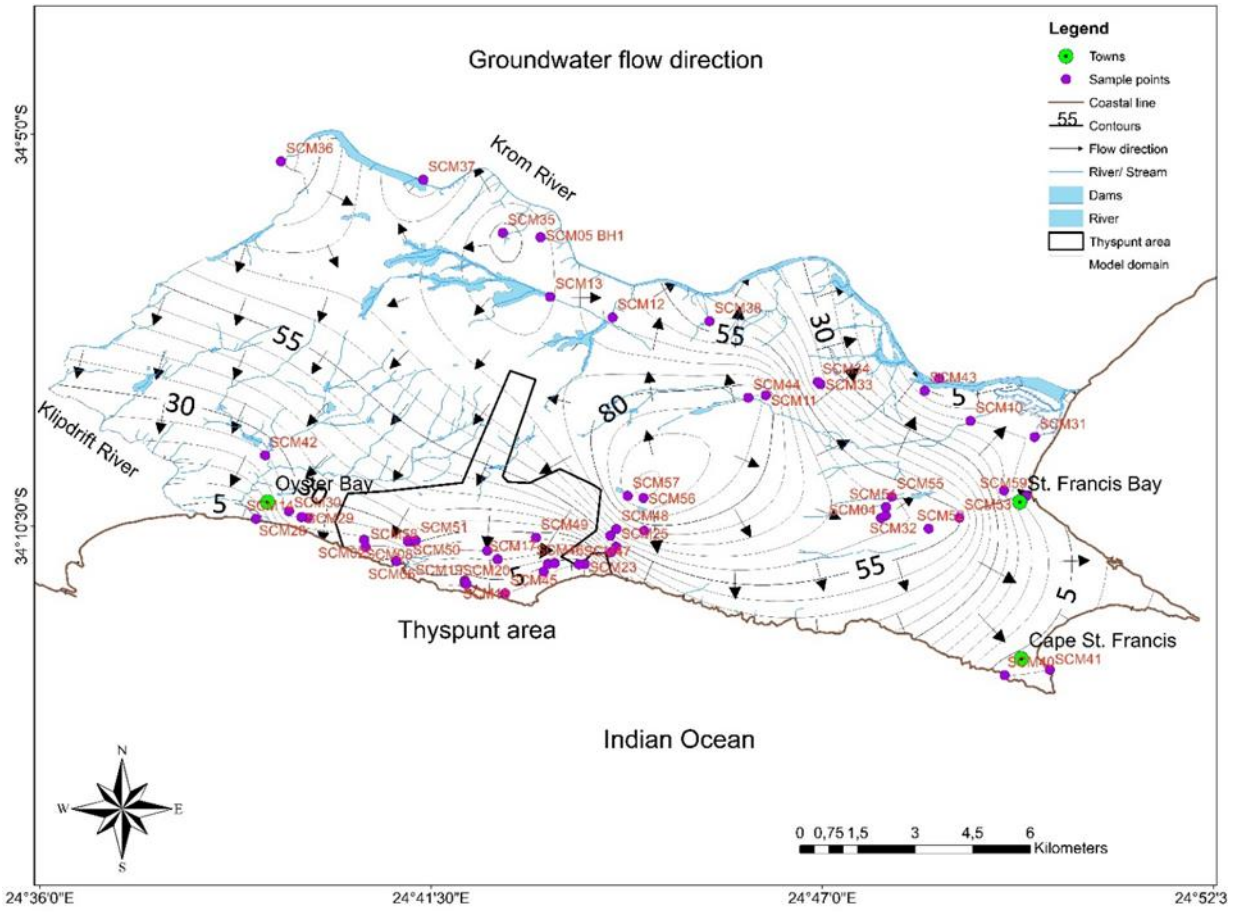

Figure 4.10. Groundwater flow direction map of Thyspunt Area (Courtesy: Moneri Modiba).

4.4. Groundwater discharge

Two types of springs exit in the area: coastal springs occur along the coastline of the study area and contact springs on and around the nuclear site. The contact springs mostly occur along the sandstone/quartzite and sand dune contacts. Figure 4.11 shows a schematic representation of a contact springs fed by wetlands and rainfall. The wetland and rainwater circulate through mobile dunes and indurated dunes and appear at the contact been the dunes and lower quartzites. In the farmlands, where sand dunes are almost non-existent, the springs occur along the sandstone/quartzite and shale contacts. Contact springs are the dominant type of spring in the study area, and occasionally form stream outlets. Coastal springs form at the intersection between the water table or potentiometric surface of the groundwater and beach/ coastal sedimentary deposits. As expected, the coastal springs dominate the coastal regions of the area, and mostly form large streams that directly discharge into the Indian Ocean. Few artificial/pseudo springs that resemble a depression spring also exists in the

area. Depression springs are springs that form where a topographical depression intersects the water table (Manga, 2001). An example of a pseudo depression spring is located at the Dune Ridge Lodge; an abandoned sand quarry is infilled with groundwater (Figure 4.12).

There is no groundwater abstraction from the boreholes on the proposed nuclear site. Groundwater is lost through surficial discharge as springs and baseflow contribution to wetlands. Numerous wetlands occur around the study area, with many wetlands concentrated on the proposed nuclear site. These wetlands exhibit variation in size, geochemistry and isotopic composition, and these are discussed in subsections 4.6 and 4.7. The bigger wetlands are perennial and supported by baseflow contributions during periods of no rainfall. Moreover, the wetlands act as sources of groundwater recharge to some of the dune aquifers, and support the contact springs around the dune deposits (Figure 4.11). Outside of the Eskom site, groundwater abstracted from boreholes is used for irrigation, livestock and domestic use.

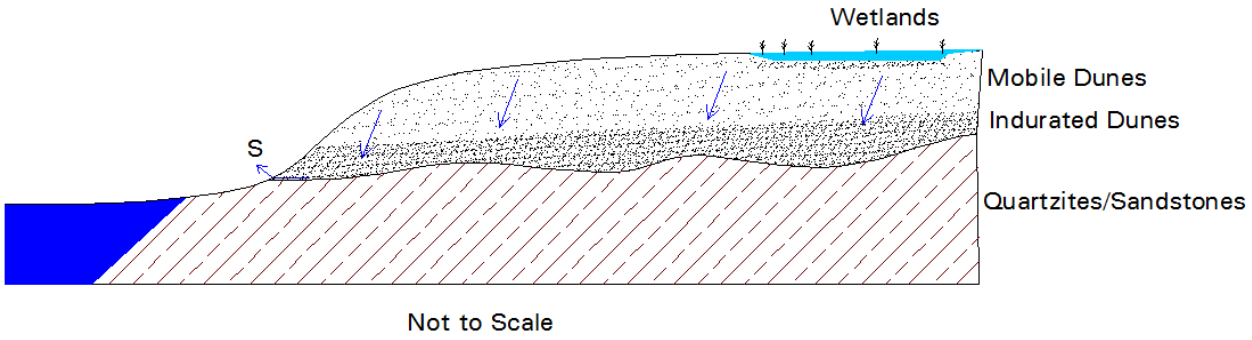

Figure 4.11. Schematic sketch representing contact spring occurrence in the area.

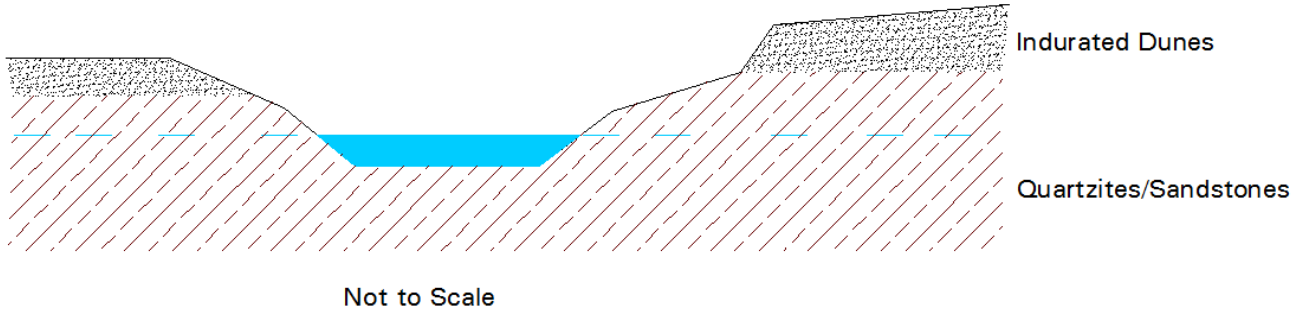

Figure 4.12. Schematic sketch representing depression spring occurrence in the area

4.5 Groundwater recharge and availability

4.5.1 Groundwater Recharge

The graphical evaluation of the water level data is presented in Figure 4.13, Figure 4.14, Figure 4.15, and Figure 4.16. Borehole THY-MR5 shows two periods of water level changes, an increase in

groundwater level from February 2009 to June 2010, and a steep decrease in groundwater level from July 2010 to December 2013. One recharge period is noted, which is February 2009 – June 2010. Annual recharge for 2009 and 2010 are 4.001 mm/year and 6.402 mm/year, respectively. Borehole THY_RP11 shows a continuous decline in groundwater levels over the two-year monitoring period. A plausible explanation for the continuous decline in groundwater level is an increase in groundwater discharge into springs or underlying aquifers, since most of the water is retained within the consolidated/indurated sand dune. Groundwater discharge through borehole abstraction is not a plausible cause of the decline in water level, since none of the boreholes in the Eskom site are pumped for any purpose. Groundwater discharge into springs and /or the leaking of the aquifers are, therefore, possible causes of the decline in groundwater levels. The lack of groundwater abstraction from all boreholes on the site eliminates the possibility of anthropogenic-related groundwater decline in the aquifer. The active dune system coupled with the windy climate of the study area create suitable conditions for continuous erosion of the local geology (especially the unconsolidated mobile dunes and Algoa Group deposits) and thus, increase the likelihood of spring formation (contact springs). As such, an increase in the number of springs may lead further groundwater decline in the absence of ample recharge.

Borehole THY_RP2 shows a cyclical variation in water table levels, and thus used to estimate recharge (Figure 4.15). Three recharge periods are noted: January - April 2012, November 2018 - April 2013 and July - August 2013. The winter recharge could represent the delayed recharge through circulation process in the unsaturated zone. Annual recharge for 2012 and 2013 is 72.18 mm/year and 70.66 mm/year, respectively. Borehole THY_MR5 shows an increase in groundwater recharge over the two-year period. In contrast, borehole THY_RP11 shows a decrease in groundwater recharge over the 2012 – 2013 period, although there is no groundwater abstraction from the boreholes. The continuous decline in water level is possibly a result of aquifer leakage that causes loss of groundwater into the underlying quartzite (fractured) aquifer, therefore, lowering the groundwater level. This is supported by the environmental isotopes results that indicate a hydraulic link between different aquifers. In addition, groundwater could be lost as discharge to springs as indicated by the strong hydraulic link between most aquifers and springs, and this is discussed in detail in subsection 4.7. The water level hydrograph in boreholes has been presented in Figures 4.13 to 4.16.

Table 4.4. WTF recharge estimation for Thyspunt for the years 2012 and 2013

Borehole	**Date**	**Δh**	**Δt (months)**	**Δh/Δt**	**Recharge (mm/year)**	**Annual Recharge (m/year)**	**Annual Recharge (mm/year)**
THY_MR5	Feb - Dec 2009	0.44	11	0.040006	0.588	2009: 0.000588	**2009: 0.588**

	Jan - June 2010	0.384	6	0.064023	0.941	2010: 0.000941	**2010: 0.941**
THY_RP2	Jan – April 2012	1.45188	4	0.36297	36.39	2012: 0.072183	**2012: 72.183**
	Nov – Dec 2012	0.71772	2	0.35899	35.9		
	Jan – April 2013	1.58628	4	0.3965	39.65	2013: 0.070657	**2013: 70.657**
	Jul – Aug 2013	0.620052	2	0.310026	31.00		

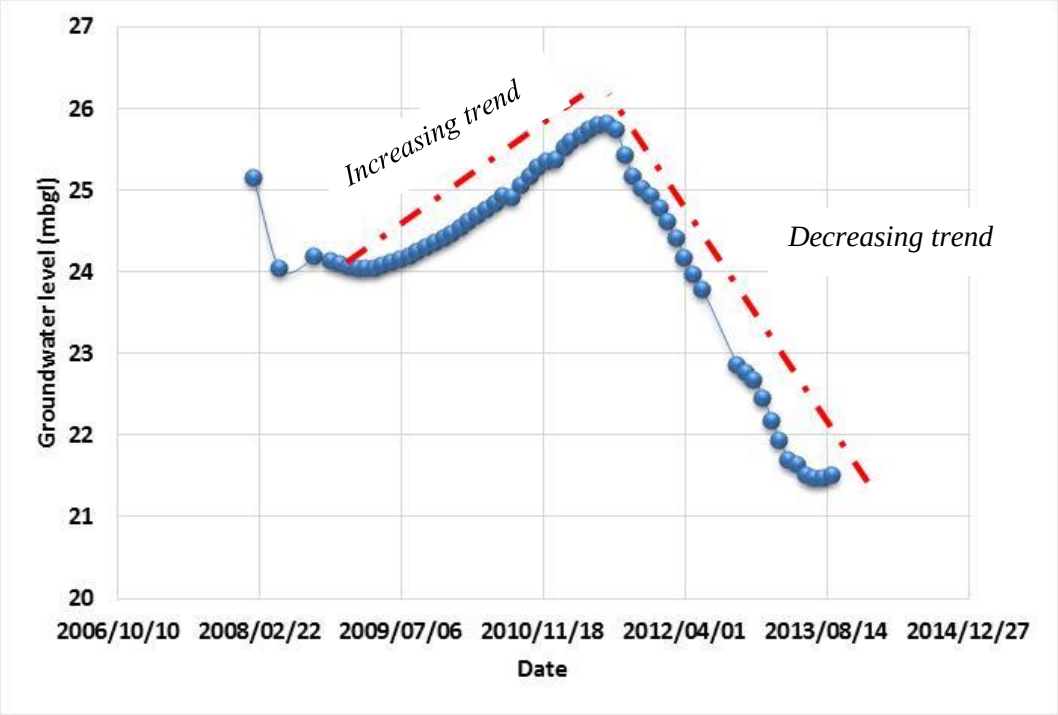

Figure 4.13. Groundwater levels measured in borehole THY_MR5

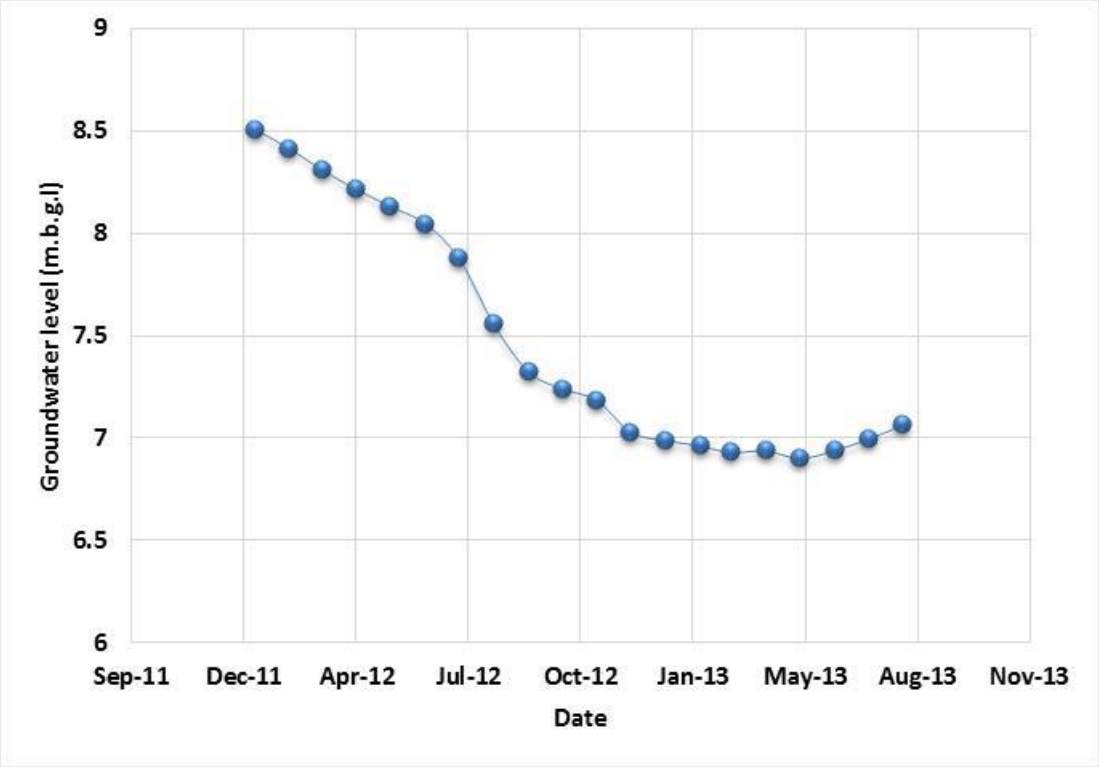

Figure 4.14. Groundwater levels measured in borehole THY_RP11

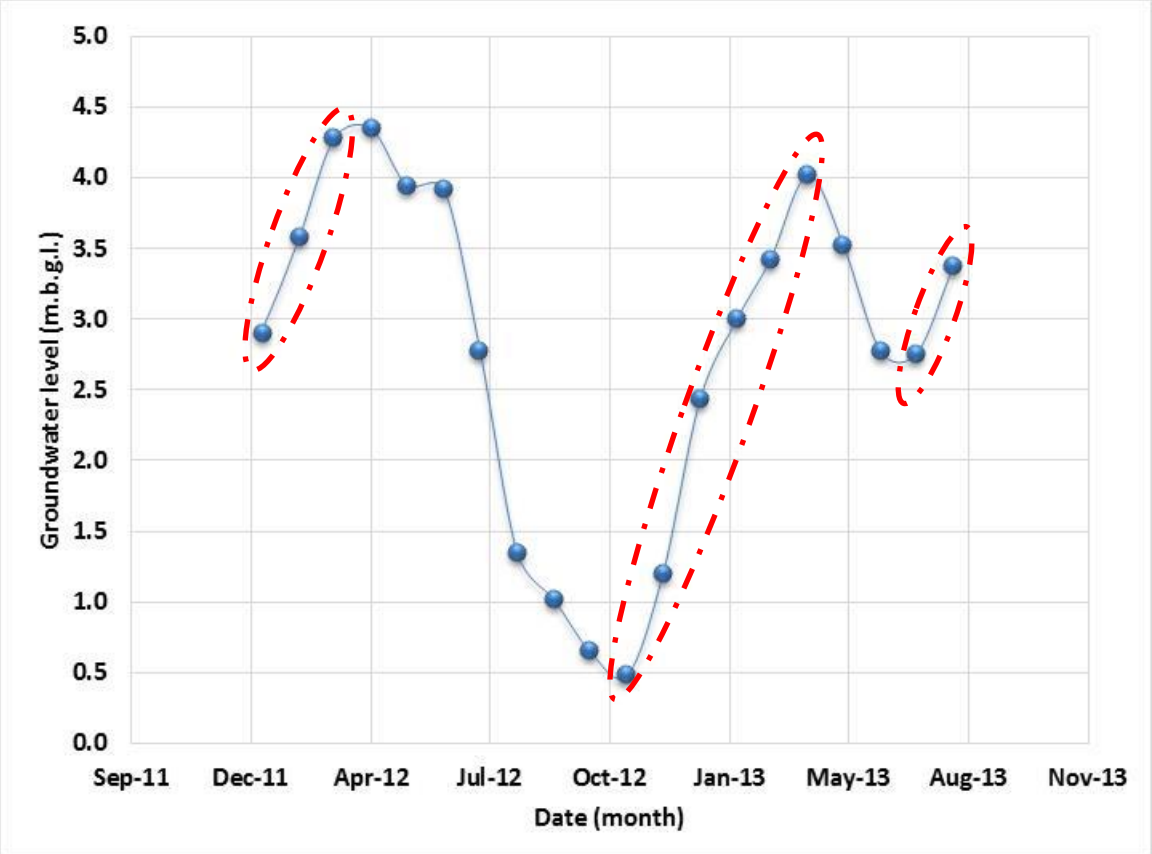

Figure 4.15. Groundwater levels measured in borehole THY_RP2. Red circles outline recharge periods

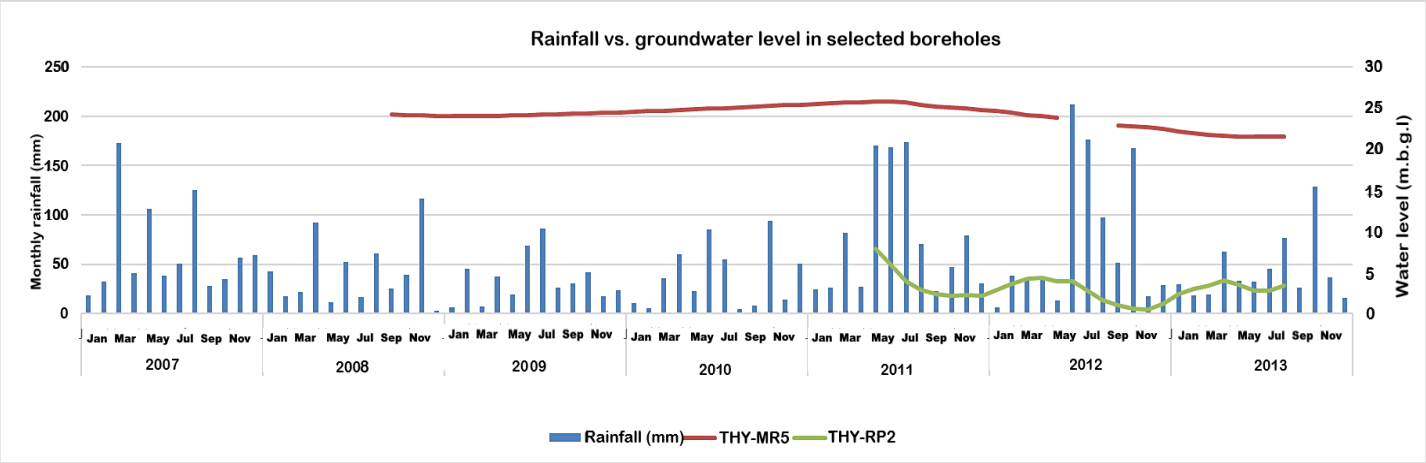

Figure 4.16. Monthly rainfall and groundwater level of THY-MR5 and THY-RP2 (Courtesy: Moneri Modiba)

4.5.2 Infiltration test

The results of the five infiltration tests are presented in Table 4.5. The infiltration rates vary across the study area. The foot print site and St. Francis Bay Park soils have the highest infiltration capacity (5.047 mm/min and 5.190 mm/min, respectively), suggesting a higher probability of recharge water and liquid pollutants to infiltrate into the soils, and possibly enter the aquifer system. This, therefore, makes the aquifers of these areas more vulnerable to potential pollution. Lower infiltration rates are encountered in the farmlands, with the lowest rate of 1.093 mm/min recorded at Rosa Farm (Figure 4.17). The working of the soils for agriculture and irrigation of the soils such that the underlying soils are near saturation are plausible explanations for the observed low infiltration rates. Soil characteristics of the study area are presented in Table 4.6. Sandy soil dominates across the study area.

Table 4.5. Infiltration test results of 5 tests from Thyspunt

Test site	**Latitude**	**Longitude**	**Altitude (m.a.s.l)**	**Soil type**	**Infiltration rate (**mm/min)	**Comments**
St. Francis Bay Park	-34.16364	024.82639	10	Sandy soil	5.047	Sparingly vegetated area
Thyspunt Site: Footprint Area	-34.17872	024.68634	54	Sandy soil	5.190	Grassy patch of land.
Thyspunt Site	-34.19150	026.71325	9	Sandy soil	4.485	Partially vegetated, organic-rich fine sand dunes.
Pennisands Farm	-34.15047	024.70840	130	Sandy soil	2.457	Grassy area adjacent to pasture field. Organic rich, fine sand substrate.
Rosa Farm	-34.10791	024.71703	56	Loamy	1.093	Worked (cultivated) soil. Test done during rainy season thus possibility of some near soil saturation prior to testing.

Table 4.6: Soil sample characteristics of 7 soil samples from Thyspunt.

Soil sample	**Sampling depth (cm)**	**Soil type**	**Infiltration rate (mm/min)**	**Remarks**
SCM_S1	30	Sandy	1.093	Dark brown, organic matter present
SCM_S2	35	Sandy	-	Dark brown, contains organic matter.
SCM_S3	40	Sandy	4,485	Brown soil with minor organic matter.
SCM_S4	35	Sandy	2.457	Organic-rich, fertilized soil.
SCM_S5	45	Sandy	5.047	Black, fine sand.

SCM_S6	100	Sandy	-	Dark brown – black soil, medium grained sandy soil
SCM_S7	130	Sandy	-	Red sandy soil. Sampled directly below SCM_S6

The results of the infiltration tests indicate that the dunes facilitate easy infiltration of any form of liquid due to high infiltration capacity. The test performed at the Thyspunt site (one at the foot print area) has the highest infiltration rate (5.19 mm/min) that can be considered as a seepage for any eventual contamination (Figure 4.18). The soils in the farmlands have been affected by agricultural activity owing to compaction and, hence, resulted in low infiltration rates. The variability in the infiltration rates could also be linked to variation in the recharge rate in the area.

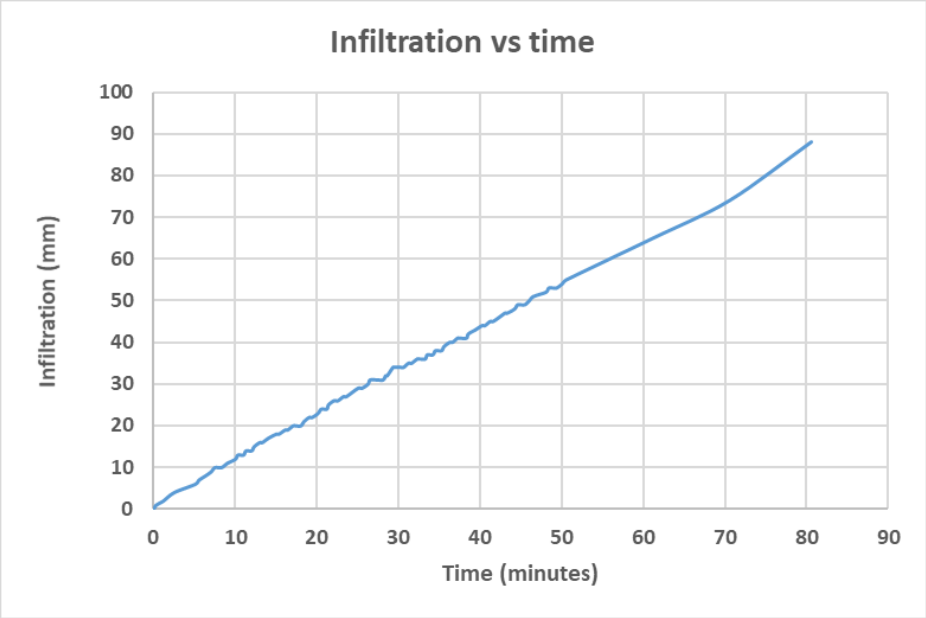

Figure 4.17. Infiltration graph of Rosa Farm

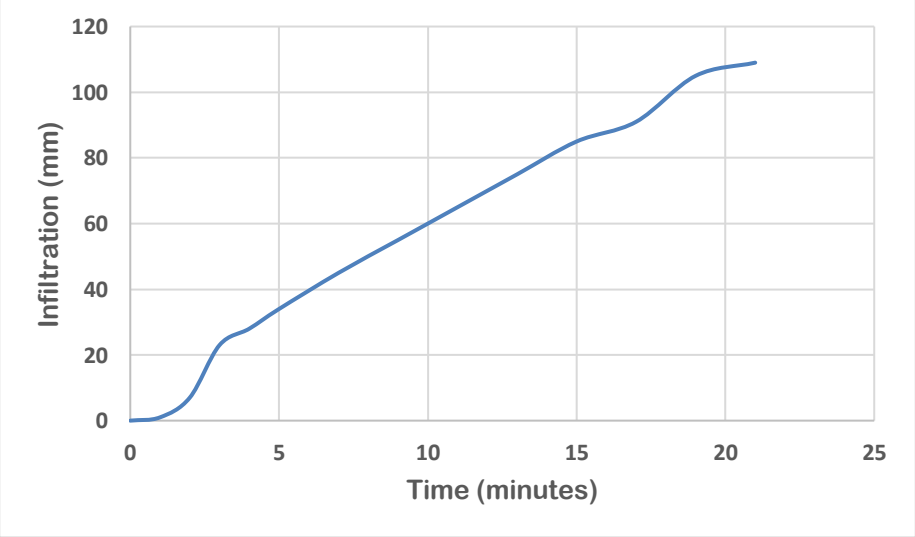

Figure 4.18. Infiltration graph of the Footprint area

4.6 Physicochemical and hydrochemistry

4.6.1 Temperature (℃)

Temperature plays an important role in the biological, physical and chemical activities of water (Christ and Wernli, 2014). Higher temperatures reduce the ability of water to dissolve gases such as O_2, N_2 and CO_2 (Christ and Wernli, 2014). High groundwater temperature could have negative impacts on the groundwater quality as it catalyses the growth of microorganisms, which may alter the groundwater odour, colour and causes corrosion problems (UNICEF, 2008). It is, therefore, desirable for groundwater to have low temperatures. The measured groundwater temperature in the area falls between 14.2 – 21.3°C (ave. 18.1°C). In contrast, the surface water temperature range is 11.5 – 19.3°C (ave. 15.4°C). The relatively low water temperatures are related to the cold season of the field campaign. Additionally, groundwater typically has lower temperatures since it is isolated from atmosphere for some time.

4.6.2 Oxidation- Reduction Potential (ORP)

The oxidation-reduction potential (ORP) is a measure of electron activity and it is used to describe how electrons are transferred between ions, molecules and atoms (Horne and Goldman, 1994). The ORP value is used to evaluate oxidation and reduction tendency of water. Groundwater and surface water with high values of ORP indicate that it has the ability to decompose plant material and organic contaminants. The high values of ORP is a sign that the water is oxidizing, and contains dissolved oxygen or oxidizing elements such as iron and manganese.

Most of the samples from the study area exist in a reducing environment, with negative ORP values that range between – 88 mV to -5 mV, indicating the deficiency of dissolved oxygen in the water. Samples SCM01, SCM05, SCM44 and SCM48 are oxidising with positive ORP values (197.7 mV, 5 mV, 98 mV and 17.6 mV, respectively). The positive ORP values of samples SCM05 and SCM48 are attributed to the elevated iron concentrations in the groundwater. The spatial distribution of ORP from the study area is indicated on Figure 4.19.

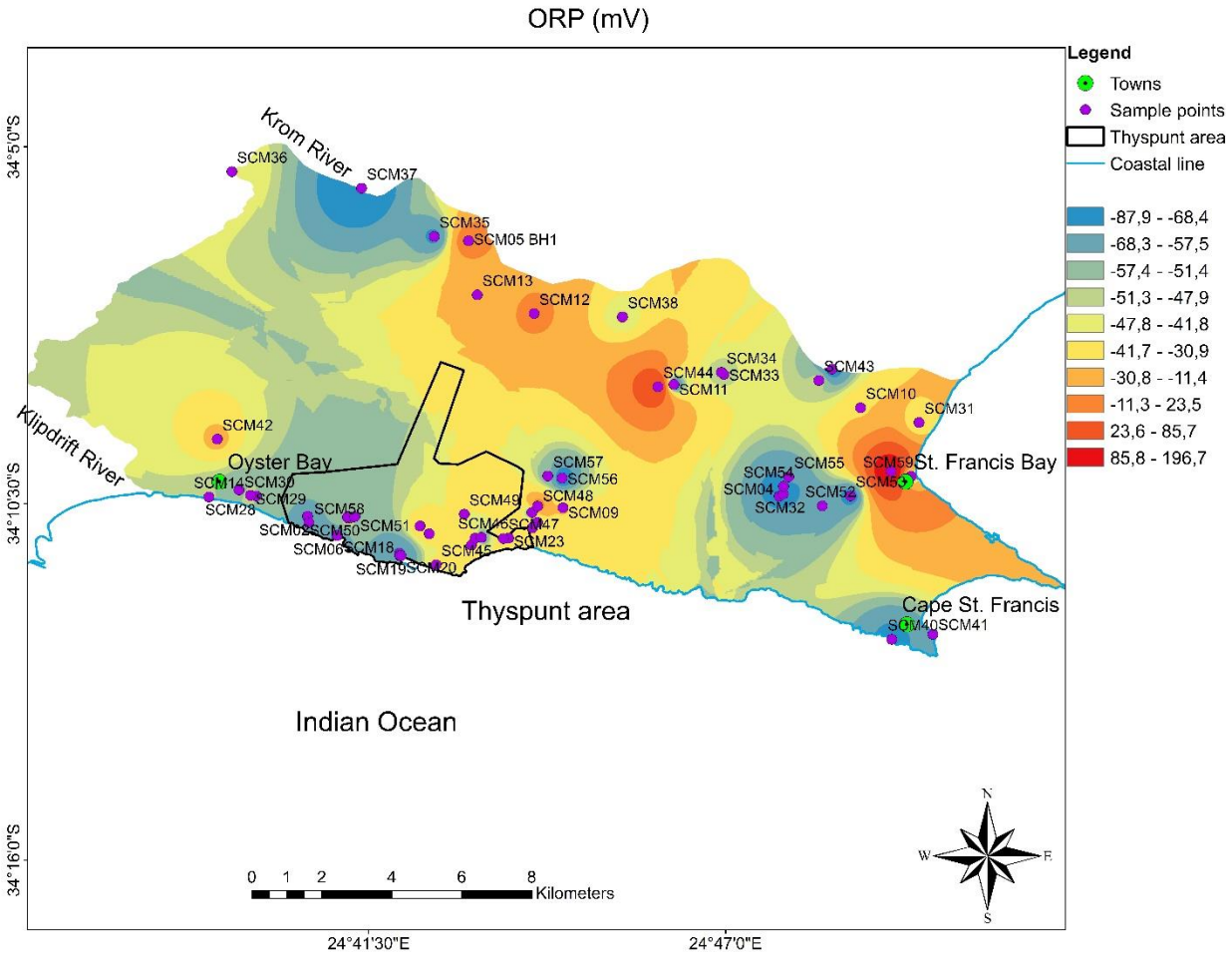

Figure 4.19. Spatial ORP map of Thyspunt (Courtesy: Moneri Modiba).

4.6.3 Hydrogen ion activity (pH)

The typical pH of groundwater systems ranges between 6 and 8.5, and normal pH for surface water is in the range of 6.5 and 8.5 (SAWQG, 1991; WHO, 2011). The measured pH values for groundwater falls between 6.14 and 8.02 (ave. 7.37), indicating circumneutral condition without extreme ranges. The slightly acidic waters are encountered in the iron-rich, artesian systems, which could be due to oxidation of sulphides or mineralised shale that released iron into the groundwater. Similarly, the pH in surface water varies from 6.75 – 8.26 (ave. 7.67) with distinct similarity to groundwater. Both surface and groundwater are dominated by weakly alkaline water type (Figure 4.20). Water acidity increases the presence and mobility of metals in water and hence facilitate contaminant migration. The high iron content in the artesian systems is made possible by the acidic groundwater and oxidising conditions and hence, the presence of numerous metals in elevated concentrations such as iron 25 µg/L, zinc 52 µg/L, barium 55 µg/L, manganese 104 µg/L, and strontium 167 µg/L.

4.6.4 Electrical conductivity (EC)

Electrical conductivity is used to account for dissolved ions in water that allow movement of electrical charge (Yilmaz and Koc, 2014). Talling and Talling (1965) proposed a water classification scheme based on the EC of water. Water with EC values less than 600 µS/cm is classified as freshwater; water E.C values of 600-6000 µS/cm is classified as moderately saline; and water with EC values greater than 6 000 µS/cm is classified as saline. The electrical conductivity of waters in the study area ranges from 286 to 7040 µS/cm, with extreme values of 35100 µS/cm for seawater. Based on the classification scheme by Talling and Talling (1965), the water in the study area is predominantly fresh water. Electrical conductivity generally shows an increasing trend towards the sea and follows the trend of the groundwater flow direction (Figure 4.21). The observed trend also indicates that the electrical conductivity of water increases along its flow path, possibly because of groundwater-rock interaction and to a lesser extent, the mixing of different waters. The low salinity in the sampled groundwater suggests the absence of seawater intrusion in the sampled aquifers.

4.6.5 Total dissolved solids (TDS)

Similar to EC, TDS represent a measure of the concentration of various inorganic salts that are dissolved in water (SAWQG, 1996). TDS is a function of numerous hydrochemical-altering processes, such as the dissolution of minerals in rocks, soil, and evaporation. Therefore, geological and mineralogical characteristics of aquifers affect TDS value. The spatial TDS distribution map is shown in Figure 4.22 The high TDS environment reflects the extent of seawater impact on the surrounding fresh water system, which is limited to the near shore areas. Water TDS generally increases towards the ocean, a trend that follows the groundwater flow direction.

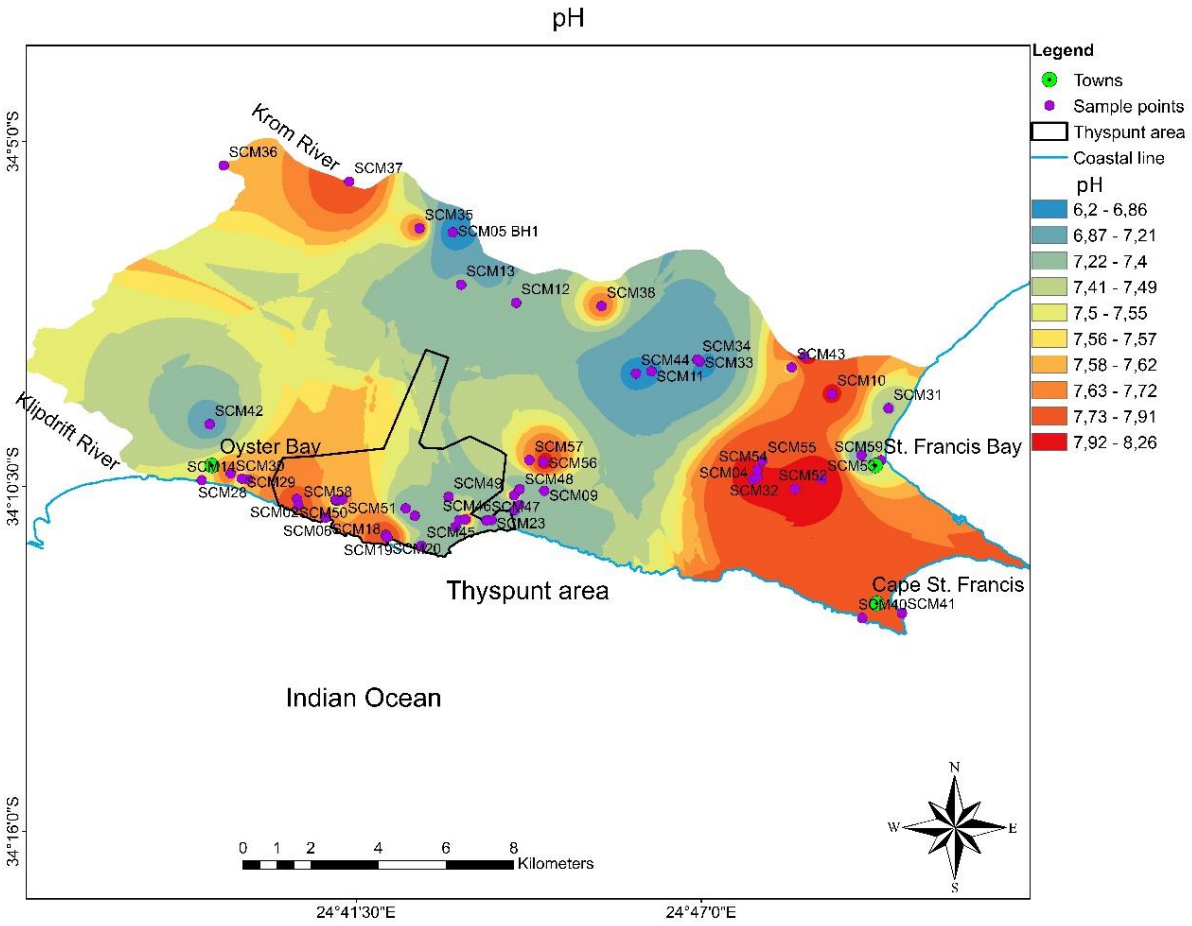

Figure 4.20. Spatial pH map of Thyspunt (Photo Courtesy: Moneri Modiba).

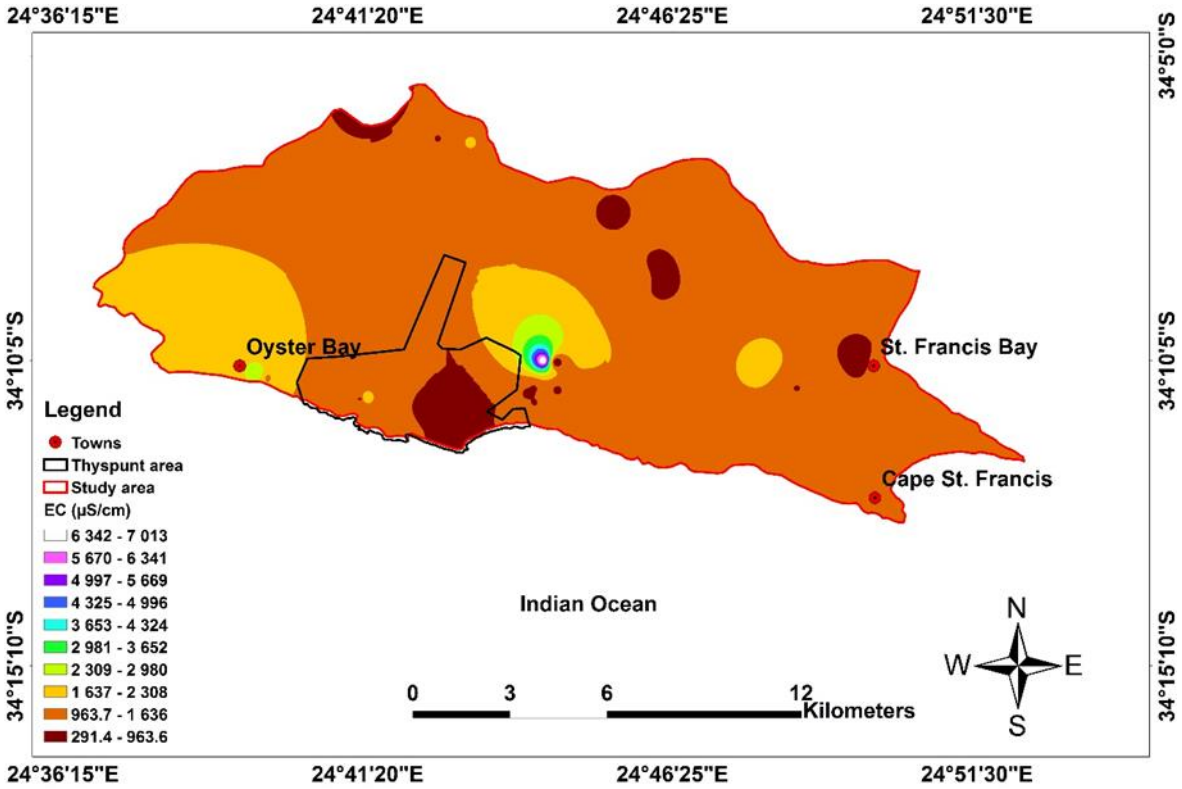

Figure 4.21. Spatial Electrical Conductivity map of Thyspunt (Courtesy: Moneri Modiba)

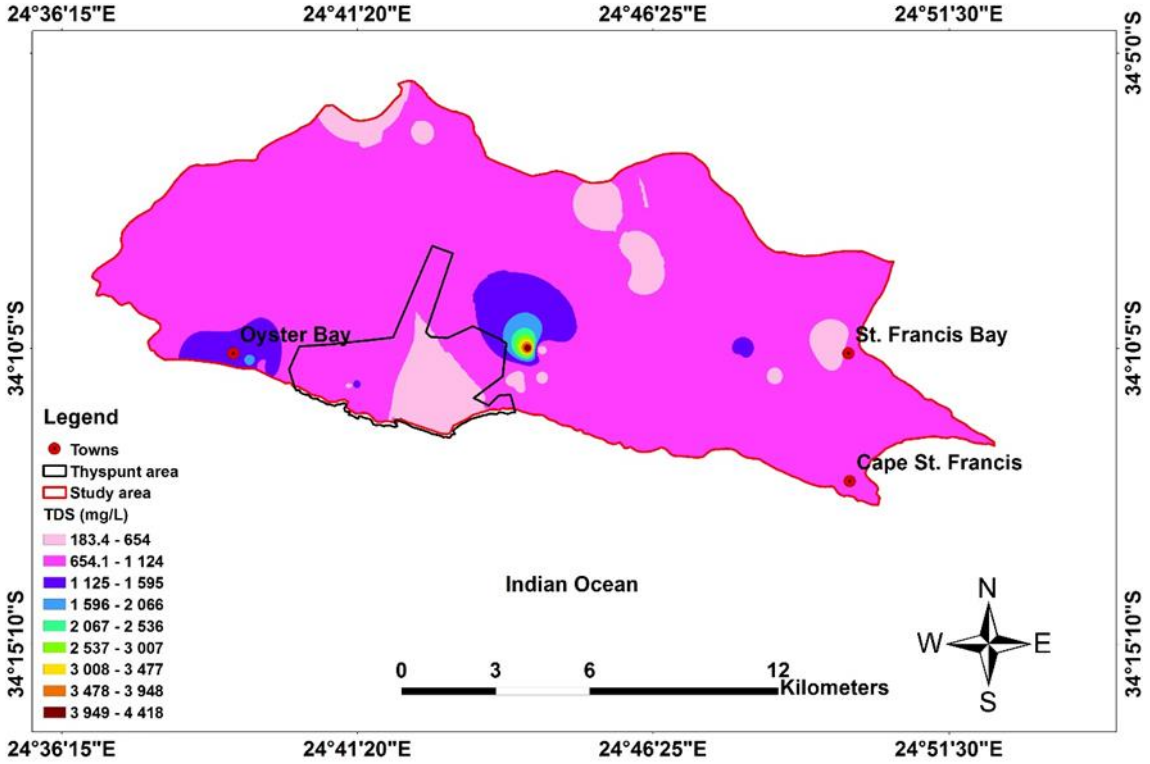

Figure 4.22. Spatial distribution map of total dissolved solids at Thyspunt (Courtesy: Moneri Modiba)

4.6.6 Hydrochemical facies

Different hydrochemical facies which were identified in the study area are depicted in Figure 4.23. The majority of groundwaters belong to the calcium-magnesium-bicarbonate facies. The highly vegetated nature of the site is a likely source of the high concentrations of bicarbonate and carbonate ions in the water, in addition to acidic rainwater (containing carbonic acid) that releases bicarbonate into infiltrating water. A probable source of the calcium and magnesium is the dissolution of carbonate cement contained in the calcareous sandstone. All spring samples and groundwater sample (SCM59) are dominated by calcium, magnesium and chloride ions, and, therefore, belong to the Ca-Mg-Cl facies. A number of possible sources of chloride could be the wet and dry deposition of chlorine from rainfall originating from the nearby sea besides the dissolution of evaporites such as halite. The observed hydrochemical facies could also be a result of the mixing between Ca-Mg-HCO_3 and Na-Cl type of water. Groundwater sample SCM47 belongs to the sodium-bicarbonate facies. The bicarbonate is possibly sourced from the soil, given the relatively shallow water table and thick nature of the vadose (unsaturated) zone. This sample also plots within the mixing region of saline and fresh water and, therefore, the mixing of water belonging to different hydrochemical facies (Ca-Mg-HCO_3 and Na-Cl) is another probable cause of the observed behaviour.

Groundwater samples SCM05, 21 and 44 (artesian borehole) belong to the sodium-chloride hydrochemical facies. Given all samples were collected from boreholes located at great distances from each other, and the lack of geochemical and isotopic correlation, it is, therefore, fair to conclude they belong to different aquifers. Chloride occurrence in the water is most likely attributed to the shale and quartzite that constitute the artesian system. Hydrochemical evolution of water in the study area is evident in Figure 4.23. The chemical evolution commences from fresh water of the calcium-magnesium-bicarbonate facies, and progressively evolves to saline water of sodium-chloride facies. The probable reactions responsible for this behaviour include water-rock interactions (including ion exchange reactions) and evaporation, and this is supported by the results of the Gibbs diagram (see Figure 4.24. The highly evolved nature of the artesian water is also likely a result of deep circulation. Deep circulating water is often subjected to different chemical and physical processes such as ion-exchange reactions during water-rock interactions. This is because deep circulating water typically has higher residence times and is, therefore, likely to undergo numerous reactions that result in the chemical evolution of the water overtime. This is supported by the residence time estimations of the artesian water which indicate a residence time of about 25 years.

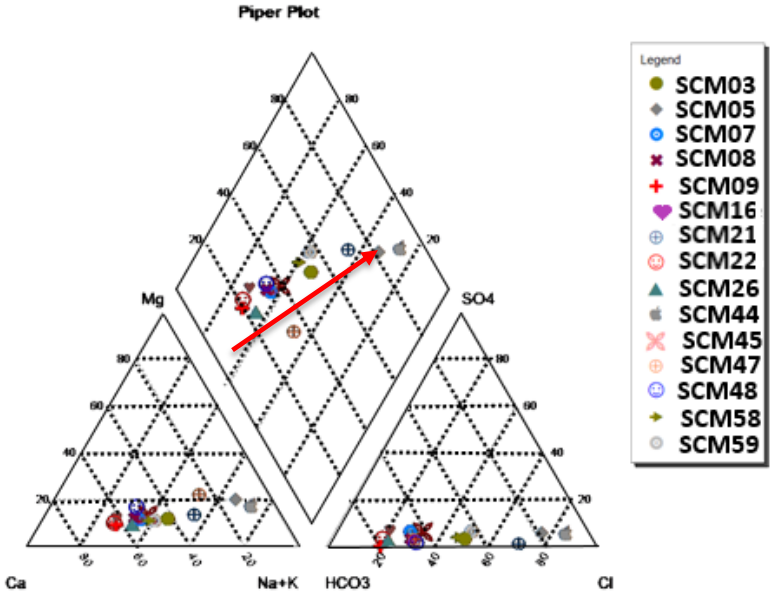

Figure 4.23. Piper plot for the Thyspunt samples. Note: Red arrow indicates direction of Hydrochemical evolution (Courtesy: Moneri Modiba)

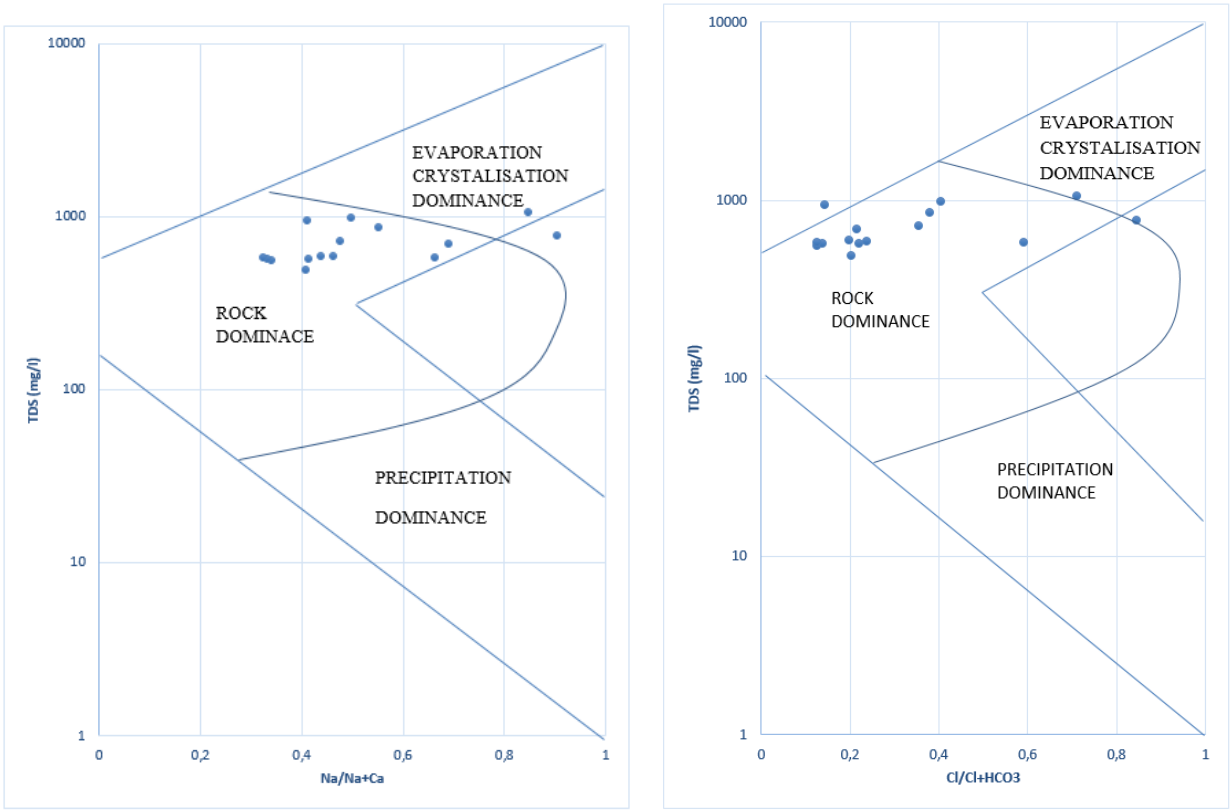

Figure 4.24. Gibbs diagrams of Thyspunt groundwater and spring samples

The water samples contain a wide variety of elements often highly toxic. Some elements such as arsenic (0.05-5.06 mg/L), iron (0.29-134.7 mg/L), cobalt (0.04-18 mg/L) and uranium (0.29-3.25 mg/L) are highly abundant, and are controlled by the geology of the area. It is alarming to record high concentration of chemical constituents presented in Table 4.7 since the geology in the area is dominated by sandstone, quartzite and shale. Geochemically, these rocks are dominated by silica (SiO_2). The primary source for such high concentration of ions and metals could be attributed to low grade metamorphism to which the local geology has been subjected to.

Major cation and metals from water samples are presented in Table 4.7 and Figure 4.25. Sodium (798.334 mg/L), boron (379.239 mg/L), strontium (1043.788 mg/L) and barium (106.353 mg/L) represent the highest average concentrations in the analysed samples. Groundwater sample SCM05 has the highest concentrations of manganese, cobalt, nickel and zinc. This borehole is located on Rosa Farm, and taps the confined aquifer composed of shale, which belongs to the Bokkeveld Group (Ceres Subgroup). Average radioactive element concentrations of lead, thorium and uranium are around 1 mg/L.

Table 4.7: Range of values for major ions and metals in water

Element	Minimum (mg/L)	Maximum (mg/L)	Mean(mg/L)
Na	35.032	10042.228	798.334
Mg	5.995	1275.914	103.845
Si	0.146	10.846	4.742
K	0.772	391.413	33.313
Ca	4.561	388.776	96.044
Li	3.192	176.499	44.46
B	11.471	4250.038	379.239
Al	4.187	93.053	20.761
V	0.009	2.06	0.369
Cr	0.221	1.191	0.565
Mn	0.63	549.193	72.27
Fe	0.296	134.686	36.782
Co	0.046	18.03	1.281
Ni	0.452	33.258	3.633
Cu	0.345	7.528	3.075
Zn	0.831	177.996	28.493
As	0.046	5.063	0.975
Se	0.007	1.683	0.396
Rb	0.531	108.697	10.787
Sr	59.227	6971.666	1043.788
Mo	0.137	9.973	2.287
Cd	0.397	0.397	0.397
Sb	0.131	1.041	0.35
Ba	6.158	1513.69	106.353
Hg	0.017	1.41	0.129

Pb	0.1	1.224	0.33
Th	0.7	14	1.685
U	0.292	3.245	1.072

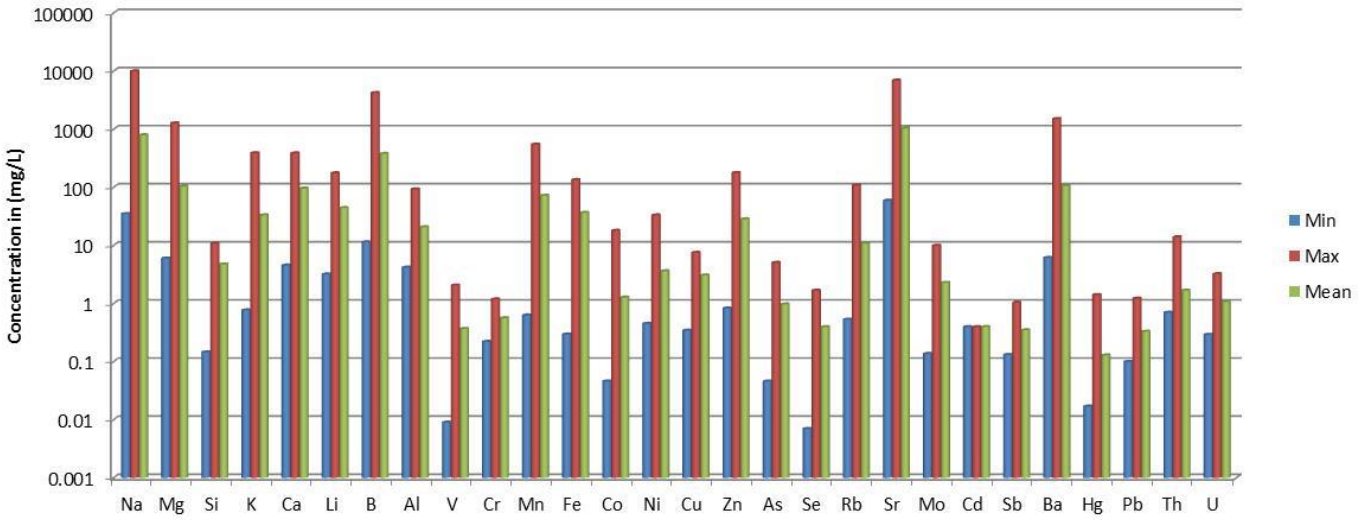

Figure 4.25. Major cations and metal concentrations of the analysed samples.

Figure 4.26. Turbid and Iron rich water from shale-confined aquifer (Courtesy: Prof. Tamiru Abiye)

Variation diagrams can be used to better understand the geochemical characteristics of water, as well as decipher the source of hydrogeochemical variation. A sodium and chloride variation diagram assists in the understanding of the relationship between the two ions (Figure 4.27). A strong correlation between the two ions suggests a common origin/ source. Given the close proximity to the ocean, sea spray is the most probable source for Na and Cl.

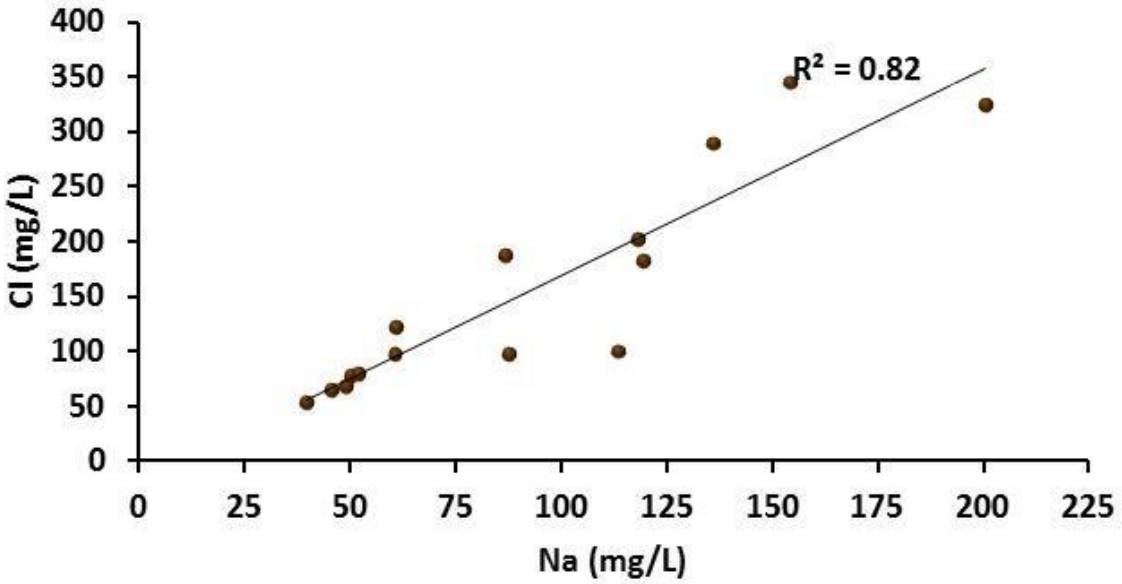

Figure 4.27. Chloride and sodium variation diagram of Thyspunt samples

A week correlation exits between the concentration of bicarbonate and chloride in the analysed samples (Figure 4.28). This suggests the presence of one of the ions has little influence on the behaviour of the other ion in water, or suggests the fact that both anions do not have common source. For example, HCO_3 could be derived from rocks and soil while Cl could be linked to the ocean.

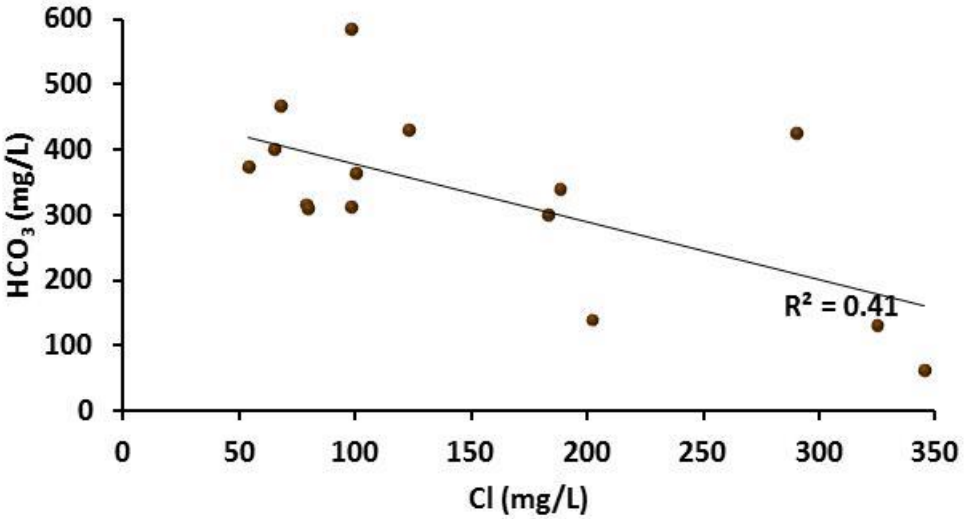

Figure 4.28. Chloride and bicarbonate variation in the Thyspunt samples

Calcium and bicarbonate exhibit moderate correlation as shown in Figure 4.29. Two possible explanations exist for this relationship. The dissolution of carbonate minerals is in part a source of the ions, but additional sources of the individual ions can also be suggested. These include the unsaturated zone (soil) and rainfall.

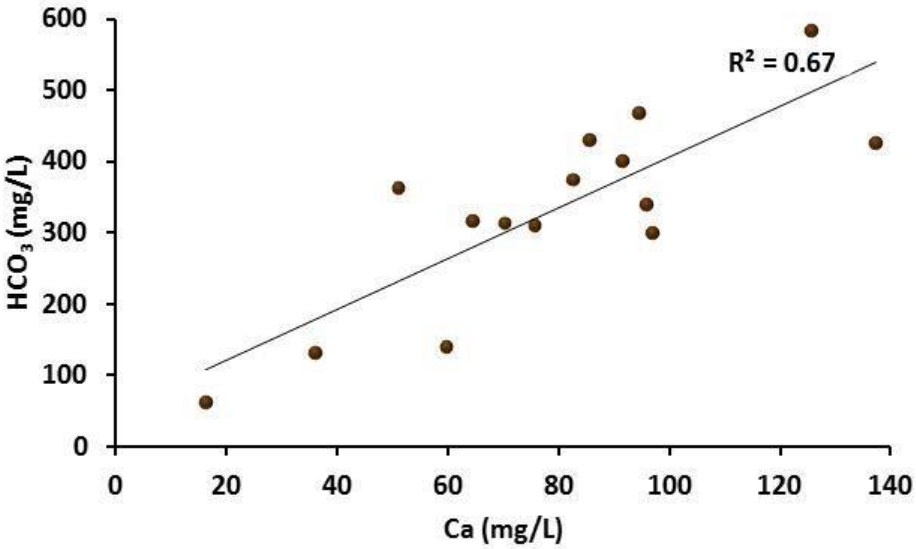

Figure 4.29. Calcium and bicarbonate variation in the Thyspunt samples

The sodium and chloride ratio is a useful tool for determining the source of the ions in water (Rajmohan and Elango, 2004). A ratio of 1 for Na/Cl measured in milli-equivalent per liter, is indicative of the dissolution of halite (Rajmohan and Elango, 2004). Eight of the fifteen samples have Na/Cl ratios less than 1, suggesting an additional source of chloride and /or the occurrence of other chemical processes such that the concentration of sodium is lowered. The dry and wet deposition of chloride sourced from the sea is an additional source of chloride. Given the close proximity of the study area to the ocean, elevated chloride concentrations are expected as wind carries the chloride and other chemical species from the ocean inland-wards (Alcala and Custodio, 2008). The presence of numerous wetlands and subsequent evaporation in the study area could also contribute to the elevated chloride concentration. The dense forest cover could also play a significant role in this regard. Plants preferentially leave behind chloride during transpiration, resulting in elevated chloride concentrations in the soil (Alcala and Custodio, 2008). Chloride is then subsequently released into groundwater. The Na/Cl ratio in seven samples is greater than 1, and this suggests the presence of certain chemical processes that increase the concentration of sodium in the water, in addition to the dissolution of evaporates (hatlite). Such processes could be ion-exchange reactions, where sodium substitutes for calcium in the water. Gibbs diagram was essential in determining the sources of chemical composition of water (Gupta *et al*., 2007). The Gibbs plot identifies three possible sources that control the hydrochemistry of waters; these are precipitation, rock weathering and evaporation. According to Figure 4.24, water-rock interaction (dissolution process) is the main control on the chemistry of most groundwater. Evaporation strongly controls the chemistry of the remaining samples.

The correlation matrix of the analysed samples is presented in Table 4.8. For the purpose of this study, variable correlation values (R) ≥ 0.5 are considered significant. A correlation strength classification based on the correlation values is proposed: r: 0.0-0.49 is weak, r: 0.50-0.69 is moderate and r: 0.80-1 is strong. A strong correlation (r=0.91) exists between sodium and chloride, suggesting a common origin/ source. Given the close proximity to the ocean, sea spray and halite dissolution are the most probable sources of Na and Cl. Calcium and bicarbonate exhibit a strong correlation, also suggesting a common source. Possible explanations for this relationship include the dissolution of carbonate minerals (such as $CaCO_3$) in the calcareous sandstones and contributions of the ions from the unsaturated zone (soil) and rainfall (wet deposition). Moderate correlation exists between EC and Na (0.79), Cl (0.69), Mg (0.64), SO_4 (0.55) and Si (0.51), and this suggests that these ions contribute to the salinization and thus electrical conductance of the water.

Interestingly, pH strongly correlates with CO_3 (0.85) and this relationship indicates the strong control of CO_3 on the water pH. This further supports the alkaline water conditions that prevail in the area. A moderate correlation (0.51) exists between Cl and SO_4, signifying a possible common source such as the abundant shale deposits in the area and to a lesser extent, dry deposition of the ions contribute both SO_4 and Cl to the water. However, the moderate correlation suggests additional sources of chloride including halite dissolution and the soil salinity. As expected, calcium strongly (0.82) correlates with total alkalinity (TAL), indicating a strong control of calcium on the alkalinity of the water.

Table 4.8: Correlation matrix of 17 physiochemical and hydrochemical variables for 15 samples

	pH	*EC*	*Na*	*K*	*Mg*	*Ca*	*Cl*	*SO4*	*HCO3*	*Si*	*Mn*	*Fe*	*NO3*	*CO3*	*F**	*Br*	*TAL***
pH	1.00																
EC	-0.11	1.00															
Na	-0.26	**0.79**	1.00														
K	-0.03	0.30	**0.58**	1.00													
Mg	-0.28	**0.64**	**0.87**	**0.79**	1.00												
Ca	**0.53**	0.15	-0.36	-0.44	-0.41	1.00											
Cl	-0.22	**0.69**	**0.91**	0.34	**0.68**	-0.31	1.00										
SO4	-0.02	**0.55**	0.40	0.19	0.32	0.09	**0.51**	1.00									
HCO3	0.31	-0.07	**-0.59**	-0.35	-0.44	**0.82**	**-0.64**	-0.15	1.00								
Si	**-0.54**	**0.51**	**0.51**	0.27	**0.60**	-0.24	0.40	0.34	-0.18	1.00							
Mn	**-0.56**	0.43	**0.68**	**0.63**	**0.81**	**-0.60**	0.45	0.11	**-0.51**	**0.70**	1.00						
Fe	-0.12	-0.09	-0.21	-0.08	-0.19	0.13	-0.33	-0.14	0.27	0.10	-0.10	1.00					
NO3	0.11	0.41	0.33	0.18	0.33	0.30	0.47	**0.71**	0.02	0.13	0.01	-0.37	1.00				
CO3	**0.85**	0.08	-0.16	-0.15	-0.21	**0.56**	-0.09	0.02	0.38	-0.23	-0.46	-0.19	0.11	1.00			
F*	0.04	**0.51**	0.35	0.26	0.22	0.18	0.34	0.39	0.05	0.02	0.20	0.02	0.32	0.05	1.00		
Br	-0.21	0.22	0.26	0.18	0.11	-0.25	0.26	0.41	-0.36	0.15	0.30	0.35	-0.04	-0.28	**0.63**	1.00	

TAL**	0.31	-0.07	**-0.59**	-0.35	-0.44	**0.82**	**-0.64**	-0.15	1.00	-0.18	-0.51	0.27	0.02	0.39	0.05	-0.36	1.00

Note: N=15; significant correlation: R≥0.50.

4.7. ENVIRONMENTAL ISOTOPES

The stable isotope results for 59 water samples are presented in Figure 4.30. The analysed samples plot within two classification fields. The first filed is the condensation field, and is indicated by isotopic compositions that plot above the meteoric water line (MWL). The second field is the evaporation field, which is characterised by isotopic signatures that plot below the MWLs.

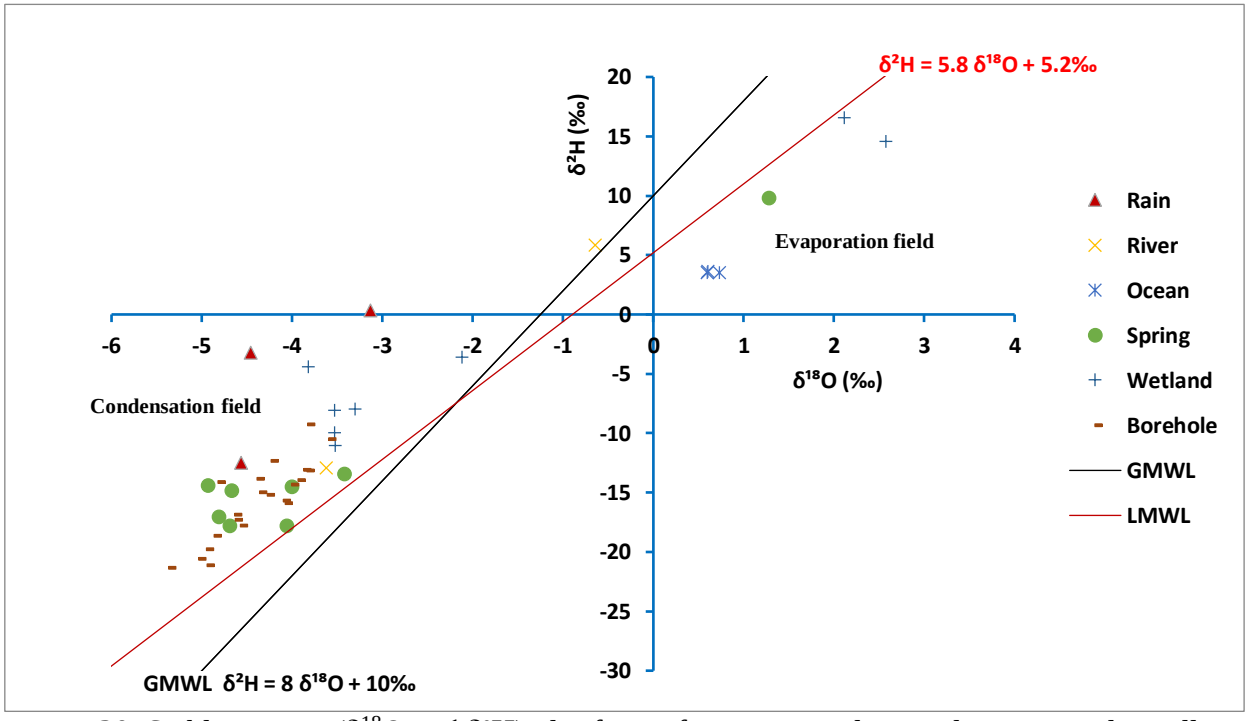

Figure 4.30. Stable isotope ($\delta^{18}O$ and $\delta^{2}H$) plot for surface water and groundwater samples collected around Thyspunt.

All analysed groundwater samples contain depleted isotope signature. This suggests that the groundwater was recharged during colder season or by moisture sourced from high latitude environment. Most of the groundwater and spring water samples have similar isotopic compositions, suggesting the springs and boreholes are tapping the same aquifers. Similarities in the isotopic compositions of some of the groundwater suggests a link between the different aquifers. This link could be a result of the leaking of groundwater from the upper, unconfined, intergranular aquifers into the lower fractured aquifers. This is further substantiated by the decline in groundwater levels of some of the aquifers in the absence of any groundwater abstraction. The wetland samples show a great variation in isotopic composition, suggesting hydraulic disconnection of the wetland systems. Wetland samples SCM12, 24, 43, 53, 54, 55 and 56 have depleted isotope signatures, indicating the wetlands contain water sourced from high latitude moisture source or have direct hydraulic link with

groundwater. In contrast, wetland samples SCM34 and 53 have enriched isotope signatures and plot within the evaporation field. This is likely a result of a separation of the wetlands from the groundwater systems and extensive evaporation effect. These wetlands are located on top of the mobile dunes, and hence, are well exposed for evaporation to occur.

The groundwater samples are depleted in heavy isotopes, even though these samples were collected relatively close to the ocean. This, therefore, suggests that the moisture source of the recharging zone is located inland, such that the rain that falls in the recharging areas is depleted in heavy isotopes. This observation also suggests that the quartzite aquifers along the coast have not been impacted by seawater which is often contain highly enriched stable isotopes. This observation is further supported by the groundwater flow lines, which indicate inflow of groundwater outside of the study area, thus suggesting the presence of an inland recharge area (Figure 4.13). Samples SCM23 (groundwater) and SCM43 (wetland) are isotopically similar, suggesting a possible hydraulic link between some wetland water and groundwater. The two samples were collected at close proximity to each other, therefore, substantiating the possibility of a hydraulic link. This confirms the fact that highly depleted rainfall feeds the wetlands, which instead infiltrate into the aquifers All rain samples display condensation and local moisture recycling signature with slightly elevated ^{2}H content. The seawater and some wetlands are plotted in the evaporation field. None of the groundwater samples have isotope signatures similar to the sea water, including boreholes in the foot print area. This in general supports that there is no seawater intrusion in any of the sampled aquifers. Two of the seven wetlands samples have an evaporation signature, suggesting the wetlands have been subjected to evaporation extreme evaporation without any contact with groundwater. One spring located on Linderhof property (-34.094; 024.68982), (SCM38) has an evaporation signature, plotted above the seawater, suggesting that the source of the spring water is evaporation pan/ small periodic wetland located nearby, which was subjected to extreme evaporation. All other spring samples have depleted isotope signatures, suggesting the source of the spring water was recharged from a moisture originating from high latitude regions or recharged during a colder season.

4.7.1. Deuterium excess (d)

Deuterium excess (*d- excess*) is used to determine the source of the moisture from which a cloud was formed and generated rainfall. The deuterium excess is determined according to the equation of local meteoric water line:

$$d = \delta D - 5.7 * \delta^{18}O$$

The deuterium excess values are presented Table 4.9. Deuterium excess values range between -0.71 and 22.64 ‰. The broad range in deuterium excess is indicative of the presence of numerous moisture

sources, as indicated by the different clusters in Figure 4.31. All rain samples have the highest deuterium excess values (SCM01, 02 and 04), suggesting a local moisture source. Given the close proximity of the study area to the ocean, the ocean is the most probable source of the local moisture.

Spring samples have deuterium excess values that range between 5.8 and 14.2‰. The relatively broad range suggests that several moisture sources of the groundwater feeding the springs exist. The springs with lower deuterium excess values indicate regional circulation of the moisture from which the spring water originated such as sources from high latitude environment.

Table 4.9: Deuterium excess values of 54 water samples.

Sample Name	Water source	D excess	$\delta^{2}H$ (‰)	$\delta^{18}O$ (‰)
SCM01	Rain	22.648	-3.25	-4.47
SCM02	Rain	18.502	0.31	-3.14
SCM03	Spring	6.459	-13.40	-3.42
SCM04	Rain	13.994	-12.51	-4.57
SCM05 BH1	Borehole	9.770	-21.37	-5.37
SCM05-BH1.1	Borehole	6.176	-22.37	-4.92
SCM07	Borehole	8.866	-13.98	-3.94
SCM08	Borehole	8.946	-14.32	-4.01
SCM09	Borehole	9.614	-15.19	-4.28
SCM10	River	8.093	-12.91	-3.62
SCM11	Spring (interflow)	10.872	-17.06	-4.82
SCM12	Wetland	10.499	-9.99	-3.53
SCM15	Borehole	8.949	-19.78	-4.95
SCM16	Borehole	8.602	-20.61	-5.04
SCM17	Borehole	7.552	-21.12	-4.94
SCM18	Ocean water	-0.712	3.51	0.73
SCM19	Spring	5.793	-17.79	-4.07
SCM21	Borehole	9.114	-13.15	-3.84
SCM22	Borehole	12.216	-12.36	-4.24
SCM23	Borehole	10.325	-10.53	-3.60
SCM24	Wetland	9.408	-11.05	-3.53
SCM25	Tap water	7.375	-8.50	-2.74
SCM26	Borehole	10.302	-15.00	-4.36
SCM27	Spring	9.415	-17.80	-4.69

SCM28	Spring	14.226	-14.42	-4.94
SCM29	Borehole	9.592	-18.64	-4.87
SCM30	Spring	12.302	-14.80	-4.67
SCM31	Borehole	7.783	-15.89	-4.08
SCM32	Tap-Borehole	8.175	-19.22	-4.72
SCM33	Artesian BH	8.779	-17.77	-4.58
SCM34	Wetland	4.288	16.54	2.11
SCM36	Wetland	11.283	-9.45	-3.57
SCM37	Municipal dam	5.109	6.02	0.16
SCM38	Spring	2,427	9,81	1.27
SCM39	Estuary	2,262	8,46	1.07
SCM40	Ocean water	0,097	3,52	0.59
SCM41	Ocean water	0,159	3,64	0.60
SCM42	stream	9,579	5,83	-0.65
SCM43	Wetland	7,918	-10,94	-3.25
SCM44	Artesian BH	9,716	-17,13	-4.63
SCM45	Borehole	9,573	-17,31	-4.64
SCM46	Borehole	11,603	-13,86	-4.39
SCM47	Borehole	10,048	-16,85	-4.64
SCM48	Borehole	13,822	-14,14	-4.82
SCM50	Borehole	12,921	-9,30	-3.83
SCM51	Borehole THY-RP5-M2	9,337	-13,13	-3.87
SCM52	Natural pond	-0,344	14,58	2.57
SCM53	Flooded quarry	5,016	17,26	2.11
SCM53	Pond	12,616	-11,18	-4.10
SCM54	Wetland	8,694	-3,60	-2.12
SCM55	Pond	17,761	-4,43	-3.83
SCM56	Wetland	11,163	-8,00	-3.30
SCM57	Spring	12,390	-8,10	-3.53
SCM58	Borehole	8,733	-14,51	-4.01
SCM59	Borehole	8,107	-15,70	-4.10

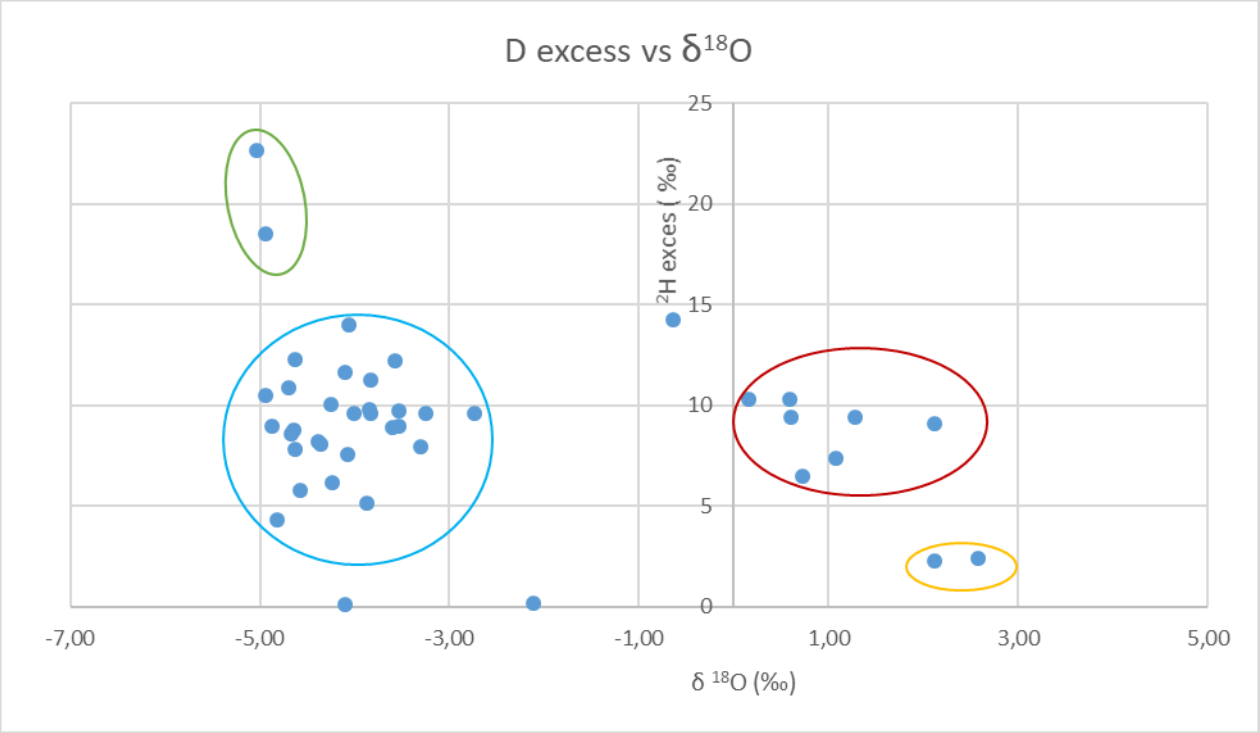

Figure 4.31. Scatter plots of $\delta^{18}O$ and deuterium excess. Note the circles mark different clusters that represent different moisture sources including mixing.

4.7.2. Tritium, ^{13}C and ^{14}C

Tritium analyses enable the determination of the mean residence time of water in the subsurface. The residence times for different samples are presented in Table 4.10. The calculated mean residence times range between 5.92 (borehole THY-MR5) to 49.71 years (Borehole NEW U1), with a mean residence time of 18.46 years. The shortest residence time of 5.92 years suggests that the aquifer is highly permeable that allows rapid recharge. The majority of the sampled groundwater has been in circulation for at least 18 years, and hence suggesting that groundwater circulation is a slow process that takes time. This also indirectly indicates the residence time of any contaminants that can potentially enter the aquifer.

Like tritium, ^{14}C can be used as a geochronological tool to determine the mean residence time of groundwater (Clark and Frtiz, 1997). However, ^{14}C only determines long-term residence times (hundreds to thousands of years). The ^{14}C and ^{13}C results are presented in Table 4.10. Groundwater sample SCM09 has a mean residence time of 430 ±5 years and is located in the footprint area. The relatively long residence time signifies that the groundwater was recharged long time ago and was in circulation from the nearby highland areas. Additionally, the long residence time could be an indication of the occurrence of deep circulating groundwater. It is worth noting that the difference in

the Tritium and ^{14}C ages from the same sample indicates that the groundwater is a result of mixing of water with variable tritium and ^{14}C content (Bethke and Johnson, 2008). The estimated mean residence time for groundwater sample SCM33 is 980 ±5 years, signifying that the water entered the groundwater system several centuries ago. This sample represents an artesian system and the long residence time could be an indication of the deep circulation and confinement of groundwater. This is further supported by the highly evolved nature of the water in the artesian system as noted from the Piper plot. Groundwater sample SCM45 has the longest mean residence time of 1000 ±10 years and is, therefore, classified as old water.

The evolution and sources of dissolved inorganic carbon (DIC) in groundwater can be traced using ^{13}C (Fritz *et al.*, 1988). $\delta^{13}C$ in the three groundwater samples ranges from -18. 81 to -10. 90 ‰ (Table 4.10). Sample SCM09 has $\delta^{13}C$ of -12.34 ‰. The depleted $\delta^{13}C$ value, coupled with the very low aqueous sulphate concentration (0.2 mg/L) suggest the source of the DIC is possibly sulphate reduction (Fritz *et al.*, 1988). Sample SCM33 has highly depleted $\delta^{13}C$ value of -18.81 ‰. Possible sources of the carbon in groundwater could be sulphate reduction, since saline, deep circulating water are typically characterised by depleted $\delta^{13}C$ contents (Fritz *et al.*, 1988). $\delta^{13}C$ content in sample SCM45 is -10.90 ‰, and this is characterised of carbon sourced from the dissolution of calcite. This is further supported by the elevated bicarbonate content (314.1 mg/l) in the water. Additionally, carbonates in form of calcite cement are present in the local geology, hence the occurrence of bicarbonates in the groundwater.

Table 4.10: Groundwater residence time

Sample	**Water source**	**Tritium (T.U)**	**Residence Time (years)**	**^{13}C (‰)**	**^{14}C Mean Residence Time (years)**
SCM01	Rain	3.2	0.00		
SCM07	Borehole	1.0	20.86		
SCM08	Borehole	1.0	20.86		
SCM09	Borehole	0.8	24.86	-12.34	430 ±5
SCM15	Borehole	2.0	8.43		
SCM16	Borehole	1.8	10.32		
SCM17	Borehole	2.3	5.92		
SCM21	Borehole	1.3	16.15		
SCM22	Borehole	1.5	13.59		
SCM23	Borehole	0.7	27.25		

SCM26	Borehole	1.9	9.35		
SCM29	Borehole	0.8	24.86		
SCM31	Borehole	2.2	6.72		
SCM33	Artesian Borehole	1.0	20.86	-18.81	980 ±5
SCM44	Artesian Borehole	0.8	24.86		
SCM45	Borehole	1.0	20.86	-10.90	1000 ±10
SCM46	Borehole	1.6	12.43		
SCM47	Borehole	0.2	49.71		
SCM48	Borehole	1.0	20.86		
SCM50	Borehole	0.8	24.86		
SCM51	Borehole	0.8	24.86		
SCM58	Borehole	0.8	24.86		
SCM59	Borehole	1.7	11.34		

The spatial distribution of tritium in the study area is Figure 4.33. Lower tritium concentrations are mostly encountered closer to the coast. This observation indicates a long residence time of the water in the aquifers. Additionally, the general groundwater flow direction is towards the ocean, thus groundwater closer to the coast is more likely to have higher residence time. Higher tritium concentrations are mostly located in the north and north-eastern regions of the study area.

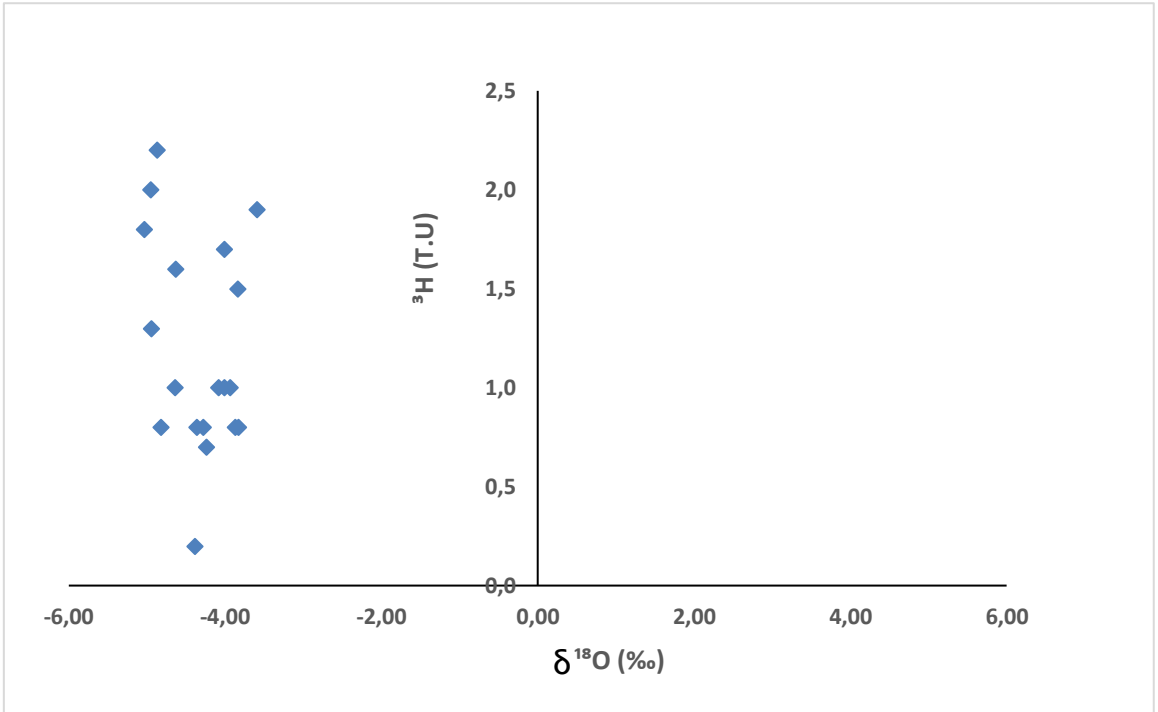

Figure 4.32. Scatter plot of $\delta^{18}O$ and tritium.

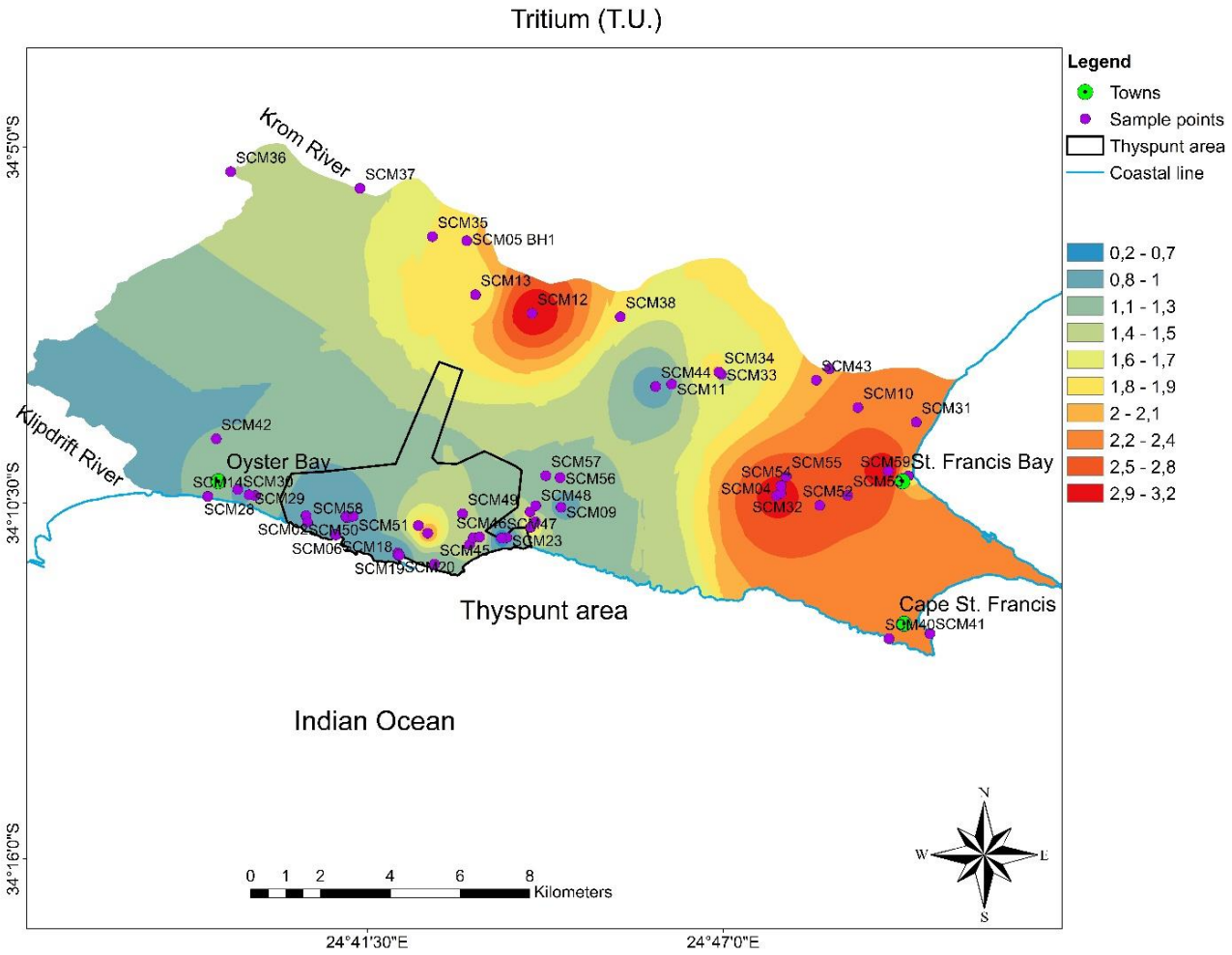

Figure 4.33. Tritium spatial distribution map of Thyspunt.

4.8. BACKGROUND CHEMISTRY: ROCK, SOIL AND WATER

Rock description and classification are presented in Table 4.11. The lithological description and geochemical analysis results are presented in Table 4.12 and Figure 4.34, respectively. The results indicate that the rock outcrop represented by shale (samples SCM_R4.1, SCM_R4.2 and SCM_R8) generally contain elevated concentrations of toxic metals. Samples SCM_R4.1 and SCM_R4.2 represent shale from the Ceres Subgroup from a quarry site located at S34.10228; E024.71935 that supplies construction material for roads. On the other hand, shale from the Baviaanskloof Formation (sample SCM_R8) was sampled along a road-cut between St. Francis Bay and Oyster Bay (S34.14334; E024.80683). Similarly, one coastal quartzite sample SCM_R1 (S34.18314; E024.68345) from the Skurwerburg Formation has elevated values of toxic metals. All other samples have considerably lower concentrations.

The rocks also contain high concentration of radioactive elements such as Lead (1.6-20 ppm), Thorium (0.5-22 ppm), Uranium (0.2-2.6 ppm) and Cobalt (0.7-9 ppm). Highly elevated concentrations of Lead in the order of 23.053 and 17.865 ppm were measured in the Ceres Subgroup shales (S34.10228; E024.71935) and Baviaanskloof Formation shale (S34.14334; E024.80683), respectively. The highest uranium and thorium concentrations (2.673 and 22.132 ppm, respectively) are measured in the Eskom site in the Skurwerburg Formation quartzite (S34.18314; E024.68345). Higher uranium and thorium concentrations (2.617 and 15.572 ppm, respectively) are also contained within the Ceres Subgroup shales.

Table 4.11: Petrographic descriptions of 12 rock samples from Thyspunt.

Sample	Rock type	Grain size	Mineralogy	Remarks
SCM_R1	Quartzite	Crystalline	Predominantly quartz	• Light – dark grey on fresh surface • Highly fractured • Cross-bedded • Quartz veins present • Sub-vertical orientation
SCM_R2	Sandstone	Medium –coarse grained (1-2.6mm)	Mostly quartz	• Ferruginous • Iron-rich cement • Well-sorted • Highly weathered and fractured.

SCM_R3	Sandstone	Fine-medium grained	Mostly quartz	• Ferruginous • Iron-rich cement • Well-sorted • Highly weathered and fractured.
SCM_R4.1	Shale	Very fine-grained (<<1mm)	Clay minerals	• Grey colour • Rich in organic matter • Well-developed bedding planes • Highly fractured. orthogonal fractures well developed on rocks
SCM_R4.2	Shale	Very-fined grained (<<1mm)	Clay minerals	
SCM_R5	Quartz vein	Crystalline	Predominantly quartz	• Infills fractures on quartzite • White on fresh and weathered surface
SCM_R7	Sandstone	Medium-grained (1-1.5mm)	Predominantly quartz	• Well sorted. • Iron-rich as indicated by rusty weathering colour.
SCM_R8	Shale	Very fine-grained (<<1mm)	Clay minerals	• Well-developed plane beds • Light tan colour • Orthogonal fractures dominant • Evidence of ancient water movement indicated by white, dust-sized compact sediment (possibly clay). • Overlain by sand dunes.
SCM_R9	Quartzite	Crystalline	Predominantly quartz	• Highly fractured • Preserved cross-bedding • Orthogonal fractures dominant (trend NE-SW) and mainly host quartz veins, • Presence of iron as indicated by iron-staining

SCM_R10	Quartzite	Crystalline	Predominantly quartz	• Highly fractured, orthogonal fractures dominant • Iron-poor • Located next to SCM_R9 on Cape St Francis coast. • Dip differently to SCM_R9 thus small-scale folding.
SCM_R11	Quartzite	Crystalline	Predominantly quartz	• White on fresh surface • Overlain by sand dunes.

Table 4.12 Geochemical results from rock samples

ppm	SCM-R1	SCM-R2	SCM-R3	SCM-R4.1	SCM-R4.2	SCM-R5	SCM-R6	SCM-R7	SCM-R8	SCM-R9	SCM-R10	SCM-R11
Li	3,657	1,198	0,858	113,9	69,65	1,225	0,942	4,927	62,09	0,697	0,387	0,422
P	108,01	87,971	40,259	1313,67	427,507	24,831	39,922	73,308	675,025	24,165	18,78	16,061
Sc	2,465	0,676	0,443	7,186	18,29	0,076	0,917	1,143	10,222	0,281	0,247	0,633
Ti	4994,299	777,758	710,162	5807,993	5919,963	183,649	1734,357	1191,608	4422,372	212,971	189,144	717,048
V	21,234	12,104	3,977	179,907	164,559	1,722	8,337	8,98	143,221	2,88	2,167	7,098
Cr	24,013	8,294	5,431	102,349	108,344	3,787	7,49	15,522	79,033	3,114	2,134	6,765
Co	3,81	2,504	1,532	9,098	5,354	2,304	1,516	1,716	8,414	1,288	0,706	1,002
Ni	9,674	7,596	4,663	38,294	24,165	6,777	4,456	5,941	34,163	4,092	2,143	2,872
Cu	65,495	8,056	4,877	29,719	36,789	6,722	7,35	7,631	59,232	4,576	2,709	3,957
Zn	17,585	8,269	4,048	110,221	86,906	33,408	7,13	4,093	69,981	5,897	2,206	3,562
Ga	5,122	2,343	1,041	26,292	30,509	0,605	1,537	1,542	22,435	0,869	0,627	1,276
Rb	34,278	10,371	6,089	99,068	207,541	1,233	9,218	5,353	129,801	4,647	3,712	6,488
Sr	12,904	6,095	8,239	72,187	94,208	6,415	14,89	10,163	26,842	6,963	4,117	3,153
Y	13,376	4,462	2,233	15,324	23,809	0,51	4,473	8,553	19,086	2,973	2,237	1,677
Zr	349,776	112,828	82,767	171,796	177,679	11,941	251,605	216,659	141,797	29,399	32,06	76,736
Nb	16,388	2,597	2,149	21,402	21,961	0,689	5,321	4,874	15,221	1,017	0,578	1,759
Ba	195,734	57,034	43,627	289,42	638,949	24,635	56,761	31,008	454,068	24,674	20,344	41,181
Sn	1,957	0,68	0,463	6,48	7,599	0,397	0,717	0,809	3,928	0,265	0,17	0,288
Cs	0,633	0,182	0,131	12,667	16,823	0,04	0,222	0,132	9,346	0,077	0,063	0,088
La	42,626	8,702	5,532	51,987	79,916	1,598	13,035	11,897	50,09	6,21	6,141	6,873
Ce	84,43	19,85	12,54	102,4	160,5	2,988	25,14	24,16	103,4	13,91	12,16	13,96
Pr	9,372	1,853	1,151	11,43	19,92	0,378	2,657	2,523	12,19	1,388	1,133	1,202
Nd	35,92	6,895	4,163	43,92	78,86	1,57	10,11	9,595	48,16	5,461	4,285	4,105
Sm	6,269	1,199	0,746	7,792	15,42	0,347	1,79	1,802	9,139	1,021	0,838	0,637
Eu	0,65	0,177	0,114	1,416	2,717	0,08	0,157	0,293	1,653	0,162	0,145	0,075
Gd	5,759	1,157	0,692	6,68	11,50	0,318	1,665	1,862	7,339	0,997	0,826	0,703

Tb	0,625	0,149	0,086	0,702	1,166	0,035	0,184	0,255	0,831	0,122	0,099	0,081
Dy	3,063	0,853	0,468	3,447	5,488	0,159	0,919	1,613	4,218	0,668	0,514	0,402
Ho	0,519	0,165	0,087	0,608	0,936	0,022	0,17	0,328	0,757	0,12	0,094	0,068
Er	1,449	0,488	0,262	1,813	2,808	0,059	0,513	0,951	2,122	0,319	0,241	0,182
Tm	0,205	0,073	0,04	0,254	0,396	0,006	0,078	0,078	0,32	0,048	0,037	0,027
Yb	1,305	0,577	0,269	1,643	2,573	0,047	0,554	0,554	2,185	0,322	0,244	0,194
Lu	0,212	0,071	0,045	0,247	0,398	0,007	0,101	0,152	0,317	0,048	0,038	0,032
Hf	9,946	3,316	2,376	4,993	5,079	0,324	7,053	6,042	4,103	0,915	0,958	2,249
Ta	1,195	0,196	0,129	1,471	1,51	0,027	0,375	0,342	1,128	0,061	0,028	0,131
W	0,521	0,122	0,094	1,361	1,327	0,07	0,277	0,29	1,265	0,235	0,053	0,073
Pb	15,02	4,34	4,471	20,96	23,05	3,155	5,988	4,887	17,86	1,611	2,547	3,386
Th	22,13	2,471	1,803	7,037	15,57	0,439	5,286	2,722	10,26	0,93	0,813	1,444
U	2,673	0,556	0,658	2,622	2,617	0,116	1,101	0,744	2,495	0,264	0,24	0,307

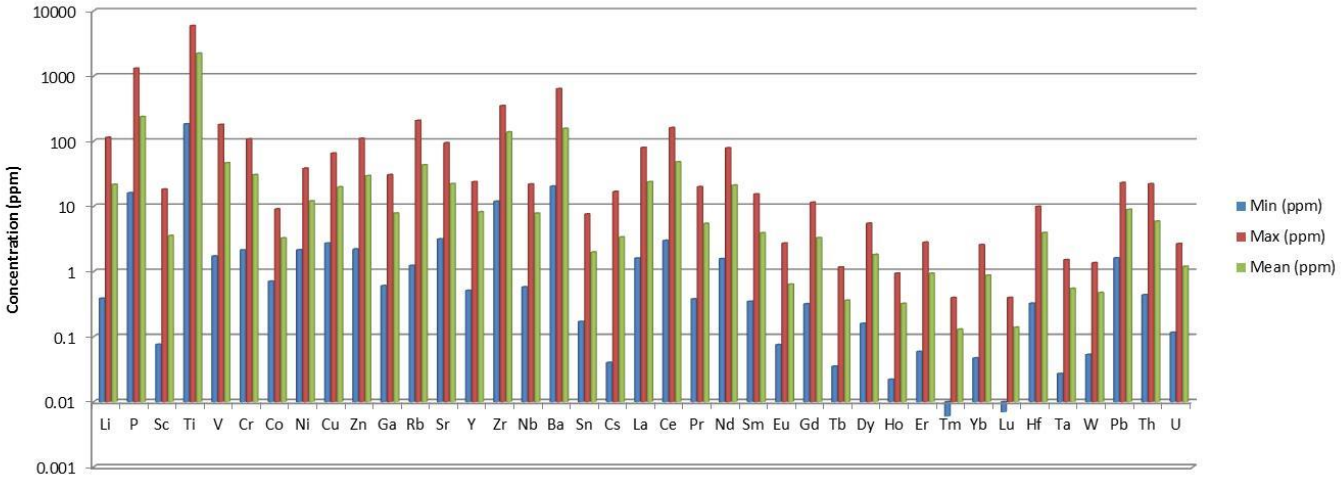

Figure 4.34. Metal concentration in rock samples from Thyspunt**.**

Major cation and metal concentrations of the analysed soil samples are presented in Table 4.13 and Figure 4.35. All soil samples contain substantially elevated concentrations of titanium (ave. 1838.395 ppm) and Zirconium (ave. 160.692 ppm), relative to all other analysed metals (see Table 4.13). This is especially the case for soil sample SCM-S2 (S34.10791; E024.71703) obtained from the Rosa Farm. Toxic metals such as Lead (2.812 - 4.037 ppm), Thorium (1.633 -3.371) and Uranium (0.707-1.741) were also detected in the soil samples. Soil sample SCM-S3 (sampled from a densely vegetated area at the Eskom site, S34.19152; E024.71235) contains elevated phosphorus concentration (2285.409 ppm). Phosphorus is likely sourced from the bacteria-aided decomposition of plant material. An additional source of phosphorus could be the adsorption of fertilizer and manure phosphorus onto the soil grains, since the area is characterised by extensive agricultural activities and cattle farming. The sampling point is located downstream of the surrounding farmlands, and thus leaching of phosphorus from the farm soils can increase phosphorus concentration of the downstream

soils through adsorption. The finding indicates that the background concentrations of all radioactive and toxic metals are high.

Table 4.13: Geochemical results for soil samples

ppm	SCM-S1	SCM-S2	SCM-S3	SCM-S4	SCM-S5	SCM-S6	SCM-S7
Li	6,79	6,997	3,281	15,569	5,954	7,826	15,509
P	96,697	42,201	2285,409	434,935	115,016	52,518	241,622
Sc	1,009	1,017	1,03	1,093	0,977	1,3	1,131
Ti	2064,547	2193,412	1429,792	1885,264	1906,139	1658,987	1730,623
V	11,406	10,488	9,705	16,384	9,713	10,438	16,528
Cr	7,523	7,649	12,33	10,298	15,455	10,931	10,526
Co	0,576	0,747	1,134	0,514	0,413	0,738	0,491
Ni	1,031	1,285	4,88	2,504	1,206	3,236	2,713
Cu	2,782	2,697	4,401	3,21	2,418	1,922	2,753
Zn	6,995	6	9,65	16,996	8,17	5,595	13,29
Ga	1,619	1,432	0,993	2,454	1,412	1,607	2,448
Rb	10,409	8,835	8,472	12,714	9,659	4,931	12,499
Sr	11,993	9,103	276,37	12,612	14,666	5,311	11,555
Y	6,719	5,977	9,985	6,732	4,459	5,686	5,271
Zr	211,637	245,996	55,407	229,075	134,3	126,758	121,67
Nb	6,179	6,367	5,178	5,726	5,464	5,761	5,357
Ba	47,322	41,935	27,359	35,577	36,379	18,295	32,509
Sn	0,485	0,557	0,48	0,734	0,397	0,507	0,974
Cs	0,54	0,438	0,364	1,138	0,481	0,502	1,121
La	7,882	9,882	11,471	6,629	14,081	4,825	7,367
Ce	17,285	21,76	23,751	14,012	30,366	22,87	16,757
Pr	1,745	1,977	2,552	1,468	3,119	0,936	1,635
Nd	6,808	7,587	10,764	5,841	12,421	3,558	6,338
Sm	1,328	1,387	2,08	1,097	1,999	0,73	1,182
Eu	0,24	0,204	0,406	0,196	0,26	0,155	0,208
Gd	1,529	1,466	2,28	1,203	1,813	1,078	1,206
Tb	0,223	0,19	0,286	0,184	0,192	0,157	0,162
Dy	1,352	1,131	1,623	1,19	0,936	1,064	1,013
Ho	0,262	0,229	0,314	0,259	0,172	0,221	0,207
Er	0,718	0,644	0,815	0,74	0,49	0,588	0,583
Tm	0,115	0,105	0,114	0,121	0,071	0,096	0,093
Yb	0,782	0,765	0,728	0,889	0,487	0,645	0,671
Lu	0,127	0,123	0,108	0,142	0,077	0,102	0,107
Hf	5,965	6,902	1,491	6,101	3,592	3,875	3,497
Ta	0,445	0,457	0,332	0,392	0,361	0,395	0,402
W	0,323	0,416	0,352	0,421	0,306	0,467	0,358
Pb	4,037	4,034	3,065	3,32	2,821	2,812	3,229
Th	2,91	3,371	1,633	2,201	2,985	1,96	2,237
U	1,056	1,076	1,741	0,918	0,707	0,756	0,768

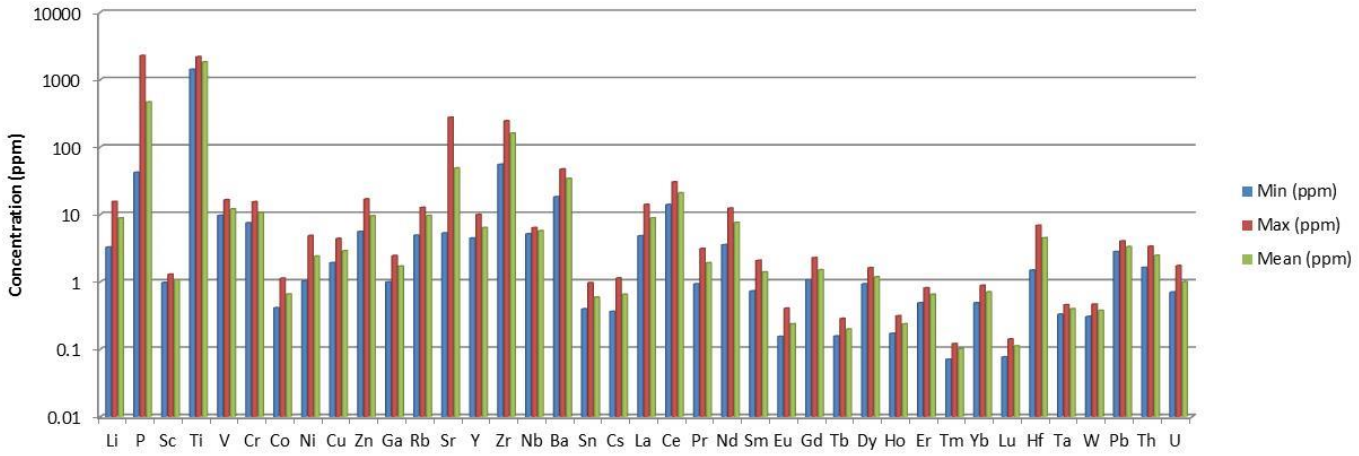

Figure 4.35**.** Metal concentrations in soil samples from Thyspunt**.**

4.9. BASELINE RADIATION

4.9.1. Naturally Occurring Radioactive Materials (NORM) in water

Eight water samples were analysed for different radionuclides, namely ^{238}U, ^{235}U, ^{234}U, ^{226}Ra, ^{224}Ra, ^{223}Ra, ^{90}Sr, gross alpha and beta activities. The location of the water samples is presented in Figure 4.36. All but strontium-90 radionuclides were present in detectable concentrations and are presented as activity concentrations (Table 4.14). ^{238}U is the parent to all measured radionuclides and is present in relatively elevated activity concentrations (17.6 – 5060 Bq/L). The presence of ^{238}U implies that there is a high potential for encountering some progenies of ^{238}U in the water, hence, the water exists under potentially hazardous radionuclide conditions. The measured ^{238}U concentrations (17.6 - 5060 Bq/L) are exceptionally higher than the NORM value of 0.03 Bq/L (Ojovan and Lee, 2014). Groundwater sample (SCM08) located in the Eskom Site (S34.1786; E24.68713) has the highest ^{238}U activity concentration (5060 Bq/L). Therefore, groundwater in this particular site is highly susceptible to further radionuclide contamination emanating from the radioactive decay of ^{238}U.

Less harmful isotopes of radium (^{226}Ra, ^{224}Ra and ^{223}Ra) were detected in the analysed samples. All water samples contain ^{226}Ra and ^{224}Ra concentrations above the WHO guideline level of 1 Bq/L. A wide range of gross alpha (11-379 Bq/L) and gross beta (-390 – 24000 Bq/L) activities exist in the water samples. The highest gross beta activity was detected in the ocean water (SCM 40 and 41), 24000 Bq/L and 20900 Bq/L, respectively. This is expected as the ocean contains a variety of radionuclides that emit beta particles during radioactive decay. In contrast, the highest alpha activity

was detected in groundwater sample SCM08, which is mostly attributed to the elevated uranium and radium concentrations (see Figure 4.37).

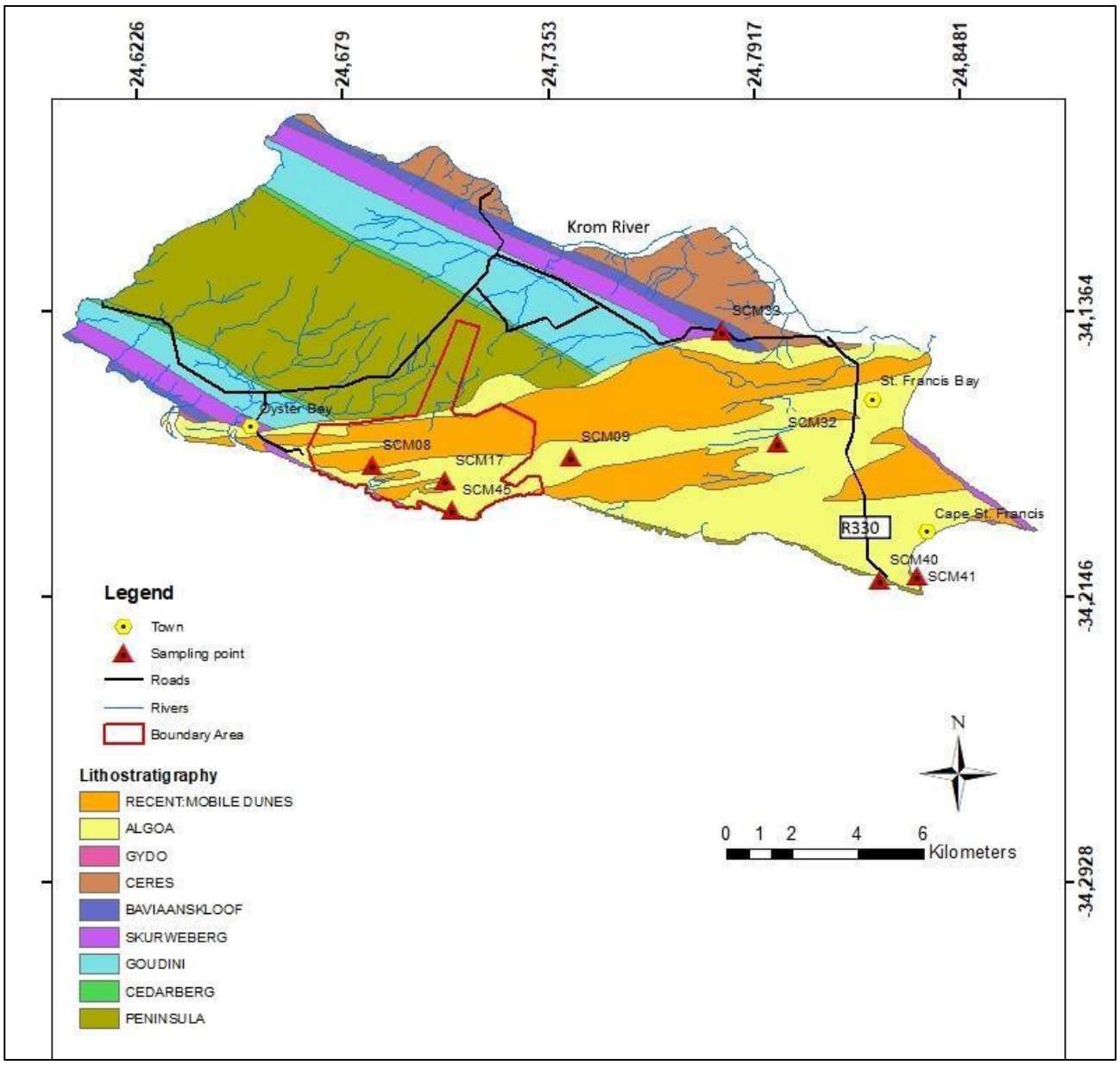

Figure 4.36. Water sample location for radionuclide measurement

Table 4.14: Activity concentration (Bq/L) in water from the Thyspunt area.

Sample code	**^{238}U**	**^{235}U**	**^{234}U**	**^{226}Ra**	**^{224}Ra**	**^{223}Ra**	**Gross Alpha**	**Gross Beta**	**Sr-90**
SCM33	17.6	0.809	12.7	147	16.6	-0.84	283	-32	<MDA
SCM41	52.3	2.41	65.5	4.7	5	5.33	340	20900	<MDA
SCM40	48.3	2.23	45.4	6.38	2.3	-2.5	11	24000	<MDA

SCM45	77.1	3.55	94.6	68.4	12.2	-5.1	336	631	<MDA
SCM17	39.6	1.82	43.9	1.1	7.16	5.8	56	100	<MDA
SCM32	42.5	1.96	55.3	24.1	7.24	0.7	137	130	<MDA
SCM08	5060	233	4830	114	10.6	-3.1	379	-200	<MDA
SCM09	85.5	3.98	77,5	6.4	5.4	2.8	51	-390	<MDA

Table 4.15: Range of values for activity concentration in water from the Thyspunt area.

Radionuclide	**Minimum (Bq/L)**	**Maximum (Bq/L)**	**Mean (Bq/L)**
^{238}U	17.6	5060	677.863
^{235}U	0.809	233	31.220
^{234}U	12.7	4830	653.113
^{226}Ra	1.1	147	46.510
^{224}Ra	2.3	16.6	8.313
^{223}Ra	-5.1	5.8	0.386
Gross Alpha	11	379	199.125
Gross Beta	-390	24000	5642.375
^{90}Sr	<MDA	<MDA	<MDA

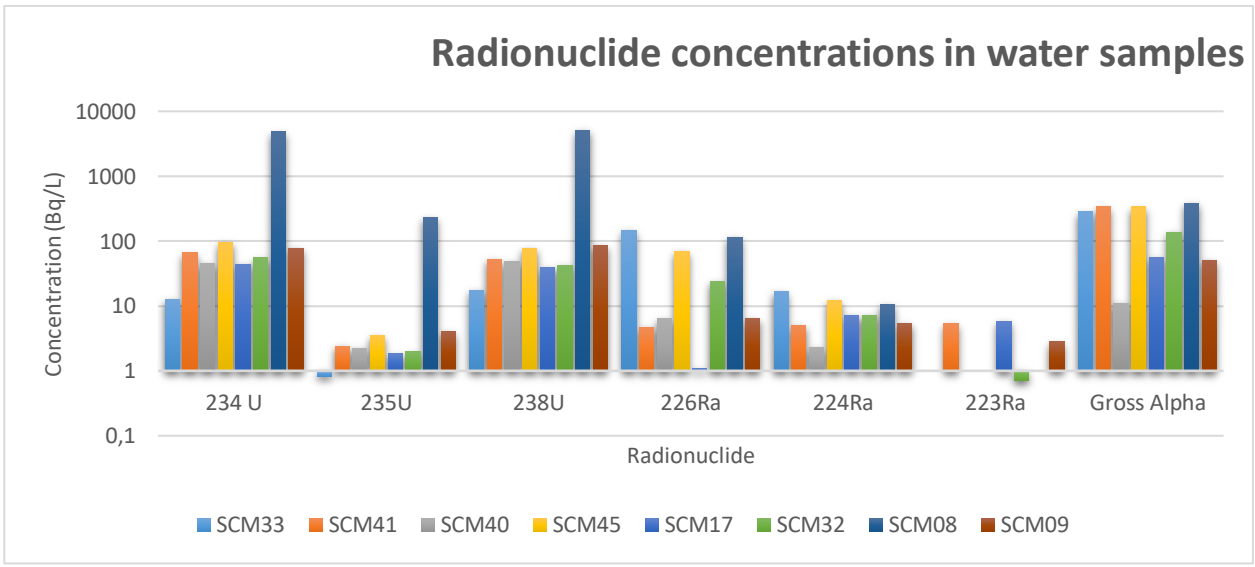

Figure 4.37. Radionuclide concentrations in water samples from the Thyspunt area

4.9.2. Tritium concentration in surface water, groundwater and sea water

Tritium sampling points are presented in Figure 4.38. The tritium results for the analysed water samples range between 0.00236 (groundwater) and 0.03776 Bq/L (rain), with the average tritium concentration of 0.01702 Bq/L (Table 4.16). Groundwater samples from boreholes and springs generally contain lower tritium concentrations with a range of 0.00236 to 0.02714 Bq/L. On the other hand, the rainfall samples contain the highest concentration of tritium, ranging between 0.03422 and 0.03776 Bq/L. This is because tritium is sourced from the atmosphere and is introduced into the groundwater system when it is dissolved in the rain. The spatial distribution of tritium in the study area is presented in Figure 4.39. Lower tritium concentrations are mostly encountered closer to the coast whilst higher tritium concentrations are mostly located in the north and north-eastern regions of the study area. This observation mimics the general ocean-ward water flow direction, thus, tritium concentration generally lowers along the flow path.

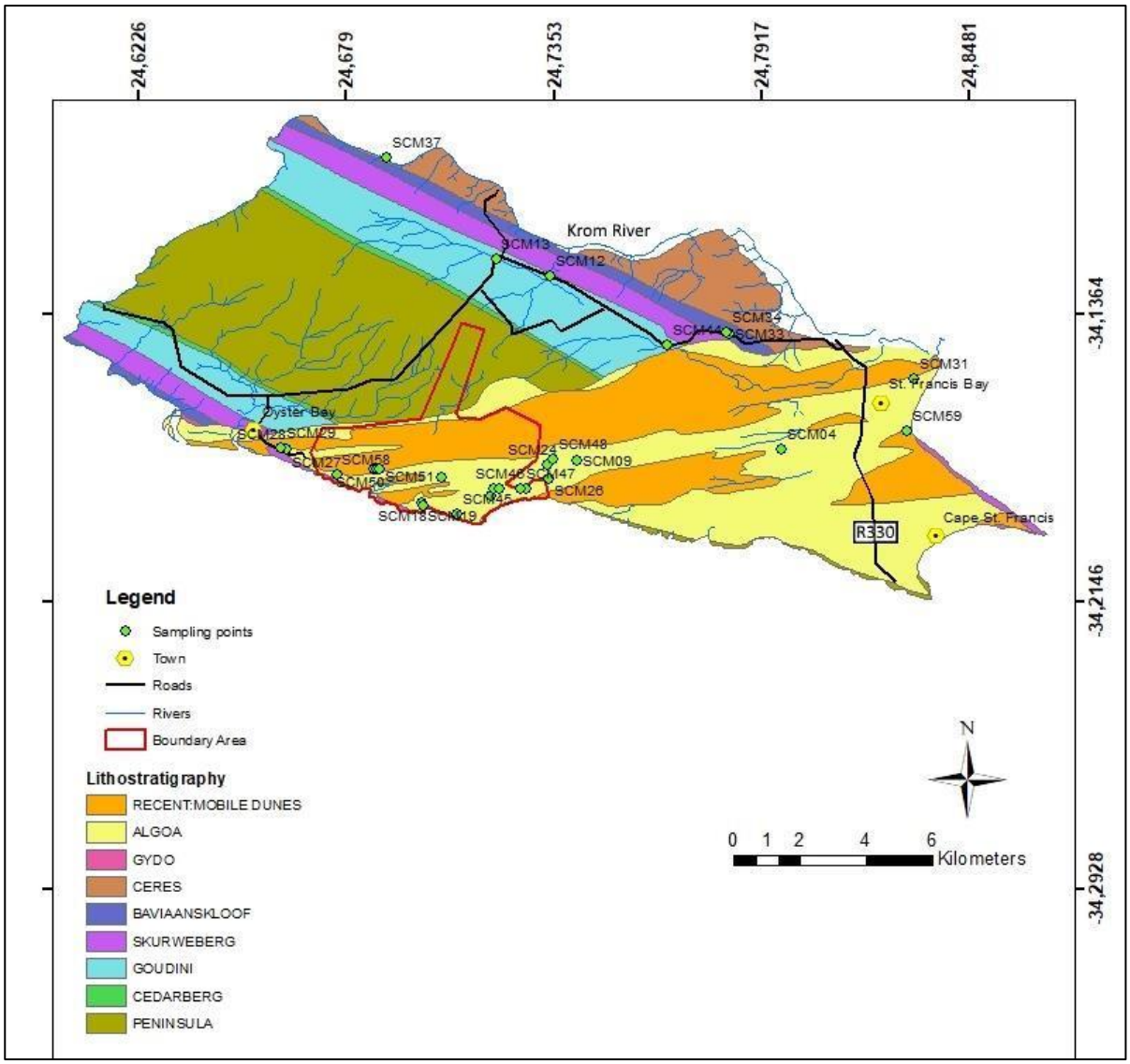

Figure 4.38. Tritium sampling positions

Table 4.16. Tritium concentration in water sampled from the Thyspunt area.

Sample code	**Water source**	Tritium (T.U)	**Tritium (Bq/L)**
SCM01	Rain	3.2 ± 0.4	0.03776
SCM04	Rain	2.9 ± 0.4	0.03422
SCM07	Borehole	1.0 ± 0.3	0.0118
SCM08	Borehole	1.0 ± 0.3	0.0118
SCM09	Borehole	0.8 ± 0.2	0.00944
SCM12	Wetland	3.1 ± 0.4	0.03658
SCM13	Wetland	1.7 ± 0.3	0.02006
SCM15	Borehole	2.0 ± 0.3	0.0236
SCM16	Borehole	1.8 ± 0.3	0.02124
SCM17	Borehole	2.3 ± 0.2	0.02714
SCM18	Ocean	0.7 ± 0.2	0.00826
SCM19	Spring	0.7 ± 0.3	0.00826
SCM21	Borehole	1.3 ± 0.3	0.01534
SCM22	Borehole	1.5 ± 0.2	0.0177
SCM23	Borehole	0.7 ± 0.3	0.00826
SCM24	Wetland	1.7 ± 0.3	0.02006
SCM26	Borehole	1.9 ± 0.3	0.02242
SCM27	Spring	1.5 ± 0.3	0.0177
SCM28	Spring	1.3 ± 0.3	0.01534
SCM29	Borehole	0.8 ± 0.2	0.00944
SCM31	Borehole	2.2 ± 0.3	0.02596
SCM33	Artesian borehole	1.0 ± 0.3	0.0118
SCM34	Wetland	2.3 ± 0.3	0.02714
SCM37	Dam	1.5 ± 0.3	0.0177
SCM44	Borehole	0.8 ± 0.2	0.00944
SCM45	Borehole	1.0 ± 0.3	0.0118
SCM46	Borehole	1.6 ± 0.3	0.01888
SCM47	Borehole	0.2 ± 0.2	0.00236
SCM48	Borehole	1.0 ± 0.3	0.0118
SCM50	Borehole	0.8 ± 0.2	0.00944
SCM51	Borehole	0.8 ± 0.2	0.00944
SCM58	Spring	0.8 ± 0.2	0.00944
SCM59	Borehole	1.7 ± 0.3	0.02006

Minimum		0.2	**0.00236**
Maximum		3.2	**0.03776**
Mean		1.4	**0.01702**

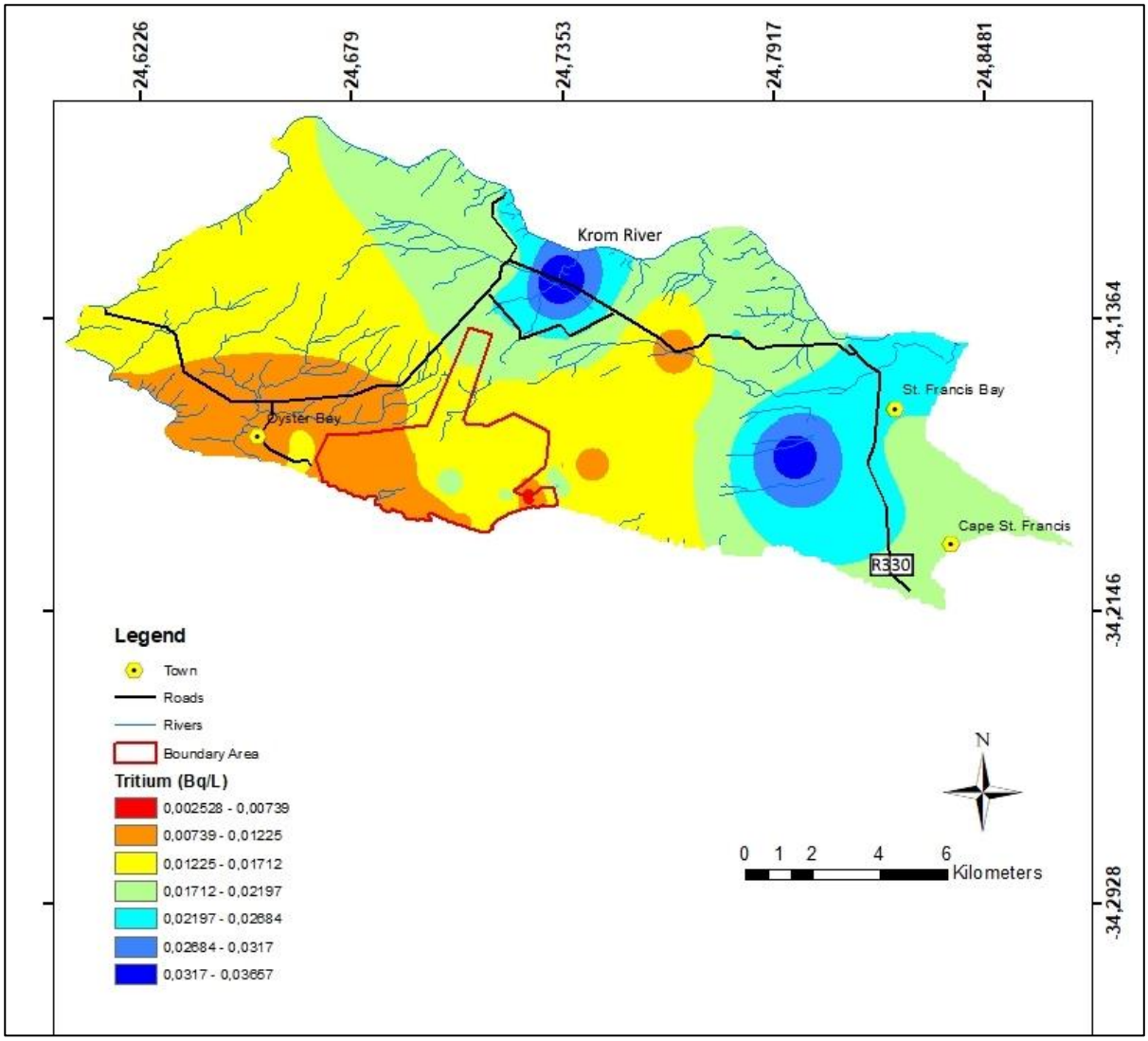

Figure 4.39. Spatial distribution map of Tritium in the Thyspunt area

4.9.3. Uranium, thorium and lead concentrations in water

The Uranium (U), Thorium (Th) and Lead (Pb) concentrations in twenty-seven water samples are presented in Table 4.17 with the respective locations in Figure 4.40. The uranium concentration ranges between 0.292 (in spring) and 3.254 µg/L (in boreholes), (ave.1.072 µg/L). All but four groundwater samples contain uranium concentration less than 0.3 µg/L. Groundwater samples, SCM09, SCM29, SCM45 and SCM46, contain uranium concentrations of 1.56, 1.03, 3.25 and 1.10 µg/L, respectively. These are, however, below the WHO drinking water guideline of 15 µg/L (WHO, 2003). Additionally, the uranium concentrations are well below the DWAF target water quality limit

of 70 µg/L (DWAF, 1996). A uranium concentration proportion map is presented in Figure 4.41. The uranium concentration is generally higher in water sampled closer to the coast, and is lower in water sampled in the inland areas.

The Thorium concentrations were <7 µg/L in all surface water and groundwater samples, excluding seawater samples, with concentrations of 14 µg/L. This is also represented in the thorium concentration proportion map in Figure 4.42. Lead concentration in the analysed samples ranges from 0.10 to 1.22 (groundwater) µg/L (ave. 0.34 µg/L). Sample SCM45 contains the highest lead concentration, which is located within the footprint area. Interestingly, seawater sample (SCM 18) contains lead concentration that is below the detection limit. The reported lead concentrations are considerably below the WHO guideline limit of 10 µg/L in drinking water (WHO, 2003). The lead concentration proportion map presented in Figure 4.43. Unlike the uranium map (Figure 4.38), there is no clear relationship between lead concentration and location of the water source.

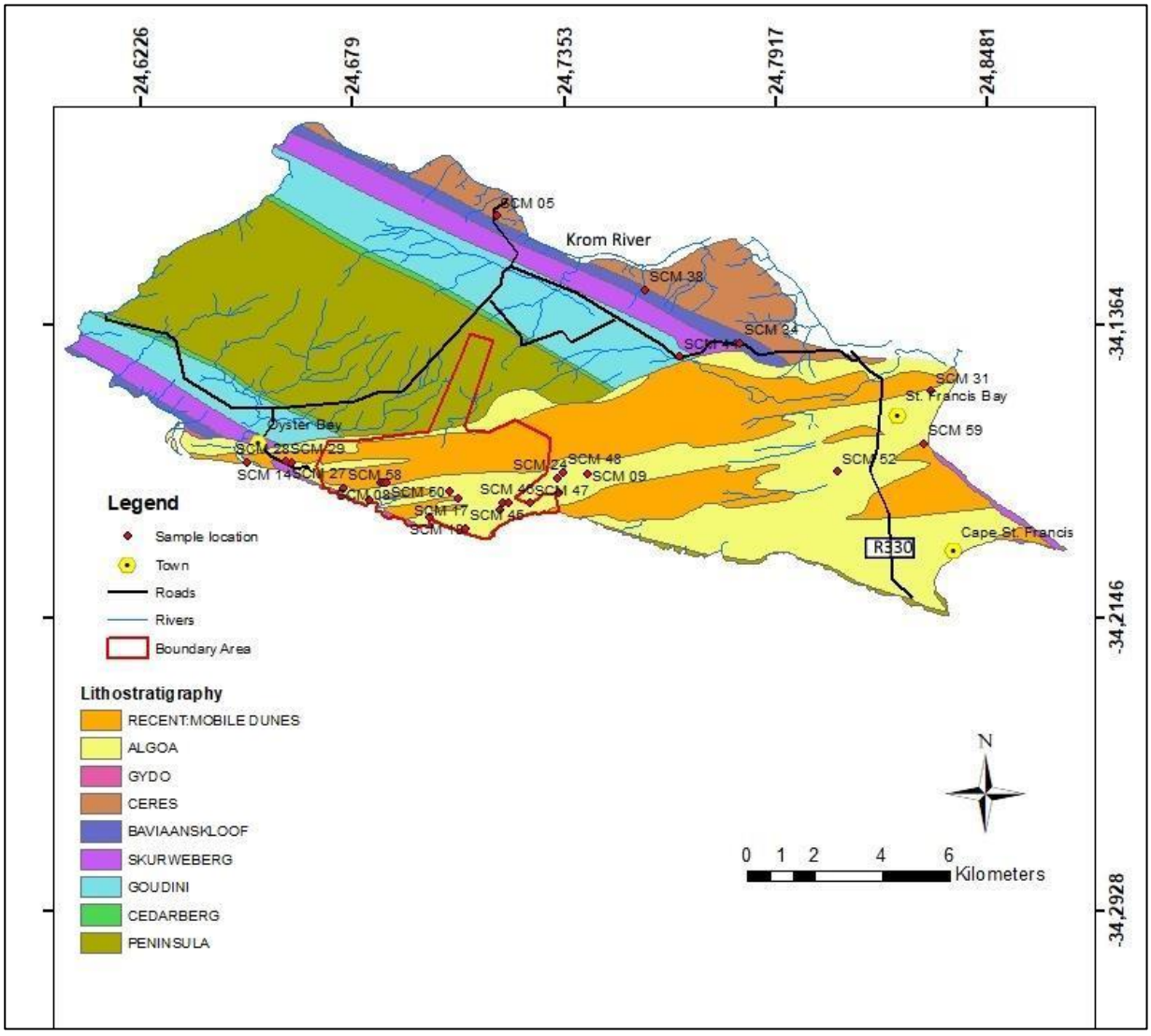

Figure 4.40. Sample locations of uranium, lead and thorium water samples.

Table 4.17. Range of values of radioactive trace metals in water samples from Thyspunt

Sample code	**Lead (µg/L)**	**Thorium (µg/L)**	**Uranium (µg/L)**
SCM 03	<0.1	<0.7	<0.3
SCM 05	0.27	<0.7	<0.3
SCM 07	1.05	<0.7	<0.3
SCM 08	0.28	<0.7	1.56
SCM 09	0.37	<0.7	<0.3
SCM 14	0.22	<14	<5.3
SCM 16	0.10	<0.7	0.36
SCM 17	<0.1	<0.7	0.37
SCM 18	<LOD	<14	<5.3
SCM 21	0.14	<0.7	<0.3
SCM 22	<0.1	<0.7	<0.3
SCM 24	<0.1	<0.7	<0.3
SCM 26	0.23	<0.7	<0.3
SCM 27	<0.1	<0.7	<0.3
SCM 28	0.16	<0.7	<0.3
SCM 29	0.31	<0.7	1.03
SCM 31	<0.1	<0.7	<0.3
SCM 34	0.21	<0.7	<0.3
SCM 38	<0.1	<0.7	<0.3
SCM 44	0.29	<0.7	<0.3
SCM 45	1.22	<0.7	3.25
SCM 46	0.13	<0.7	1.10
SCM 47	0.29	<0.7	<0.3
SCM 48	<0.1	<0.7	<0.3
SCM 50	0.17	<0.7	<0.3
SCM 52	0.17	<0.7	<0.3
SCM 58	<0.1	<0.7	0.29
SCM 59	<0.1	<0.7	0.62
Minimum	**0.10**	**0.7**	**0.29**
Maximum	**1.22**	**14.00**	**<5.3**
Average	**0.33**	**1.193**	**1.07**

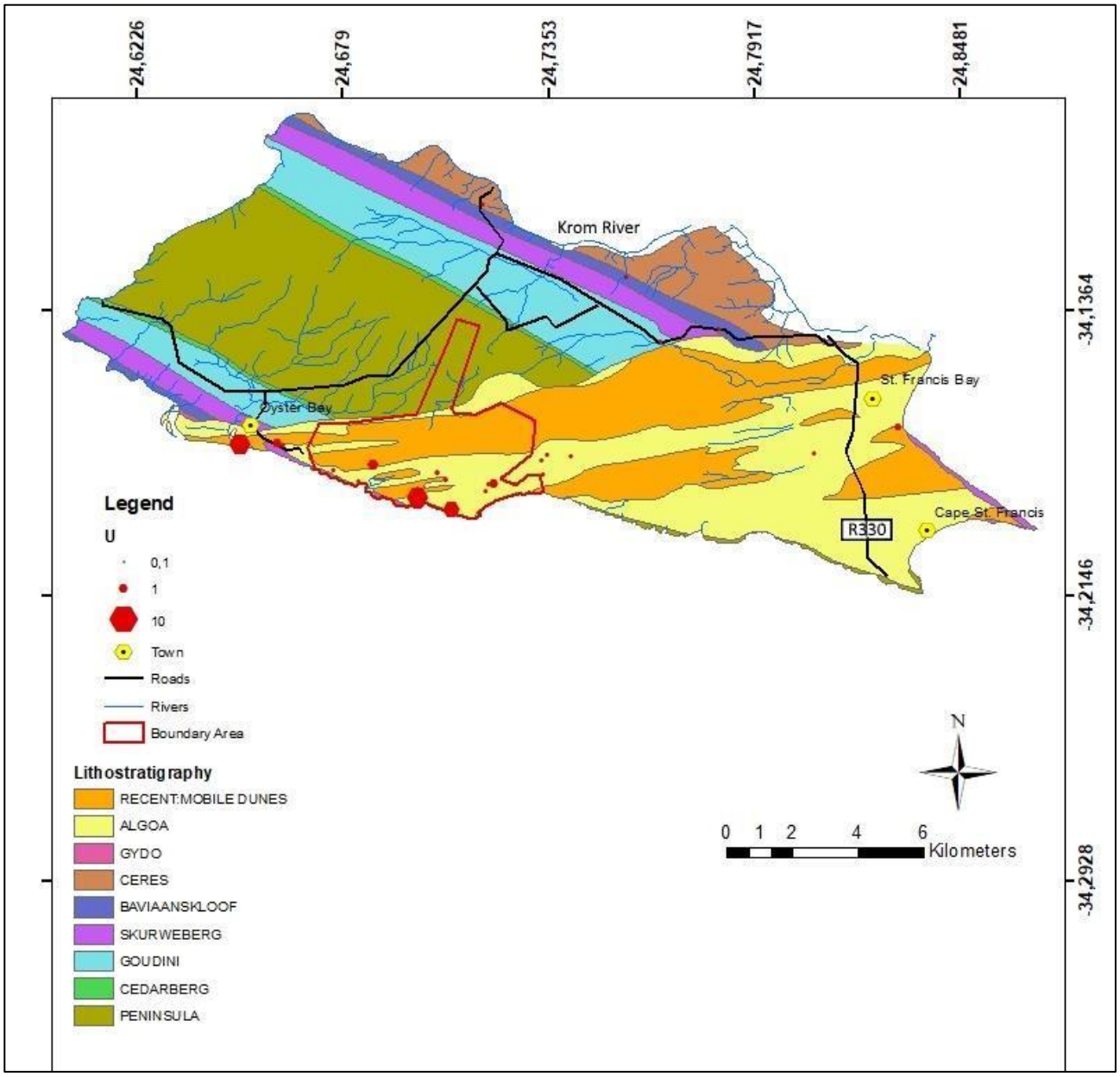

Figure 4.41. Uranium concentration proportion map (units: ppm).

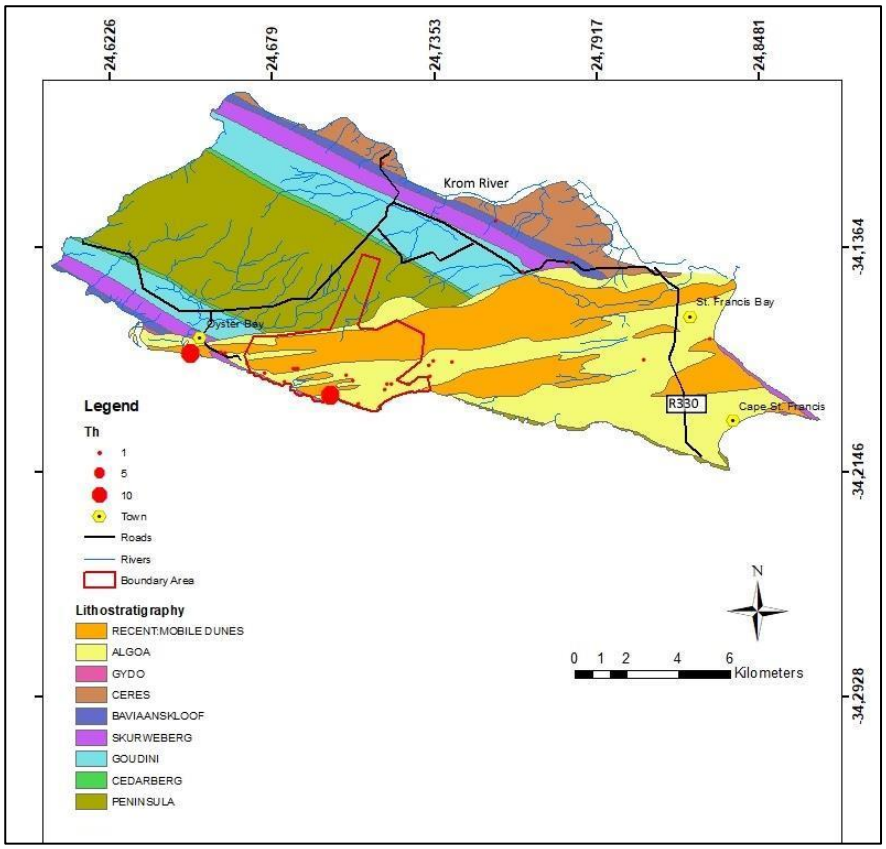

Figure 4.42. Thorium concentration proportion map (Units: ppm).

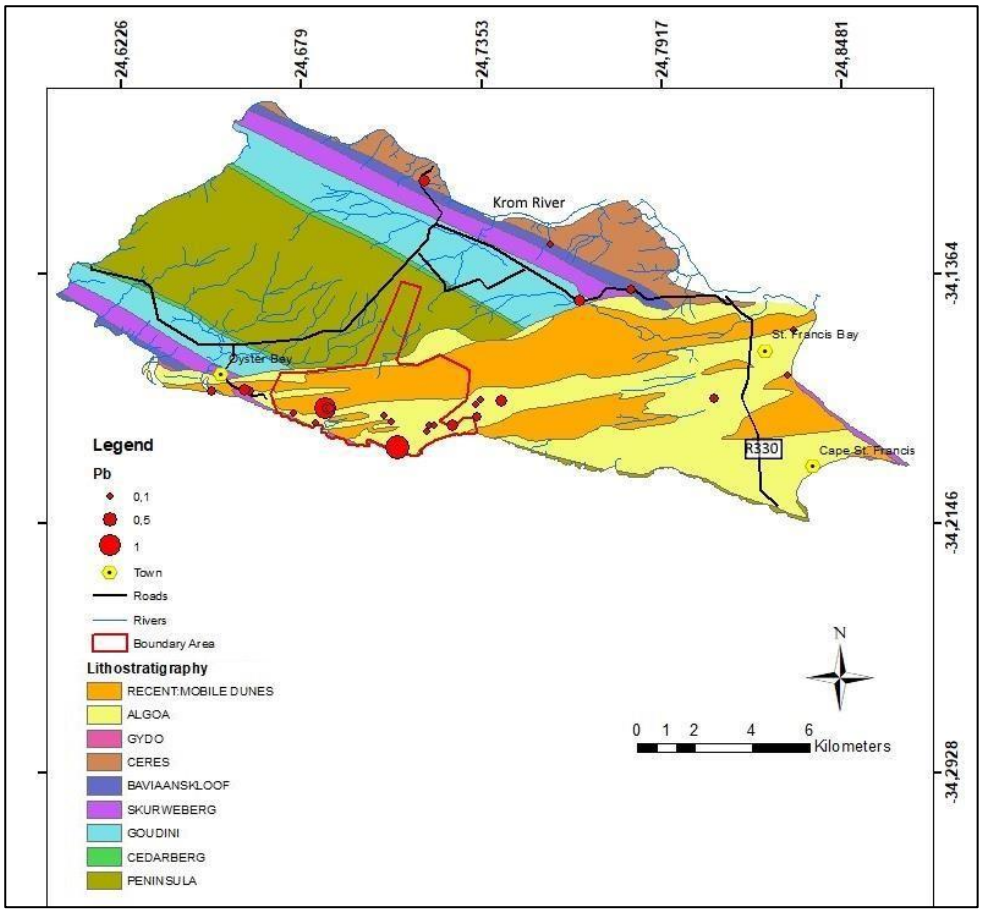

Figure 4.43. Lead concentration proportion map (units: ppm).

4.9.4. NORM in soils

The radionuclide analyses for the five soil samples are presented in Table 4.18. All the measured radionuclides have a relatively narrow range as indicated in Figure 4.44. The highest and lowest activity concentrations of ^{238} U and its first progeny, ^{235}U are in soil samples SCM-S3 (23.8 and 1.1 Bq/kg) and SCM-S5 (11.1 and 0.509 Bq/kg), respectively. Both soils are organic-rich, fine-grained sandy soils. Additionally, soil sample SCM-S3 has the highest activity concentrations of ^{234}U, ^{226}Ra ^{210}Pb, ^{235}U, ^{232}Th, ^{40}K, ^{90}Sr and Gross beta activity (see Table 4.18). Soil sample SCM-S3 was collected from the footprint area, where some of the unconfined aquifers of the Algoa Group sediments are located. The soil in this area therefore, could pose a pollution risk to the underlying aquifers through natural leaching process.

^{228}Ra ranges between 12.1 Bq/kg (SCM-S4) and 23.9 Bq/kg (SCM-S3), with a mean activity concentration of 15.64 Bq/kg. In contrast, ^{226}Ra activity concentration ranges from 17.4 Bq/kg (SCM-S4) to 38.8 Bq/kg (SCM-S3) with the mean of 23.38 Bq/kg. Although the two radium isotopes exhibit similar chemical behaviour, the difference in concentrations could be a result of two things:

1) ^{228}Ra has a shorter half-life (5.75 years) than ^{226}Ra (1622 years) and, therefore, persists less in the environment (Cothern and Rebers, 1990).

2) The two radioisotopes have different parents, thus, their concentrations are largely dependent on the parent's concentration. The lowest (9.7 Bq/kg) and highest (12.6 Bq/kg) activity concentrations of ^{232}Th, were noted in soil samples SCM-S4 and SCM-S3, respectively, and this is similar to ^{228}Ra, the progeny of ^{232}Th. All but soil sample SCM-S3, have ^{210}Pb activity concentrations that are below the minimum detectable amount (MDA).

Table 4.18: Radionuclide concentration in soils from the Thyspunt area (activity concentration).

Sample code	**^{238}U (Bq/kg)**	**^{235}U (Bq/kg)**	**^{234}U (Bq/kg)**	**^{228}Ra (Bq/kg)**	**^{226}Ra (Bq/kg)**	**^{232}Th (Bq/kg)**	**^{228}Th (Bq/kg)**	**^{210}Pb (Bq/kg)**	**^{40}K (Bq/kg)**	**^{90}Sr (Bq/kg)**	**Gross Alpha**	**Gross Beta**
SCM-S5	11.1	0.509	11.2	13.8	20.1	12.2	17.4	<MDA	57.4	6	24	140
SCM-S3	23.8	1.1	24	14.8	38.8	12.6	18.2	39	67.3	6.01	-140	184
SCM-S1	14.9	0.688	15.1	23.9	22.3	11	30.1	<MDA	50.7	5.6	300	143
SCM-S6	12.6	0.58	12.7	13.6	18.3	11.7	14.1	<MDA	18.3	5.47	85	75.9
SCM-S4	11.8	0.543	11.9	12.1	17.4	9.7	13.7	<MDA	39.2	1.6	83	112
Minimum	11.1	0.509	11.2	12.1	17.4	9.7	13.7	<MDA	18.3	1.6	-140	75.9
Maximum	23.8	1.1	24	23.9	38.8	12.6	30.1	39	67.3	6.01	300	184
Mean	14.84	0.684	14.98	15.64	23.38	11.44	18.7	39	46.58	4.936	70.4	130.98

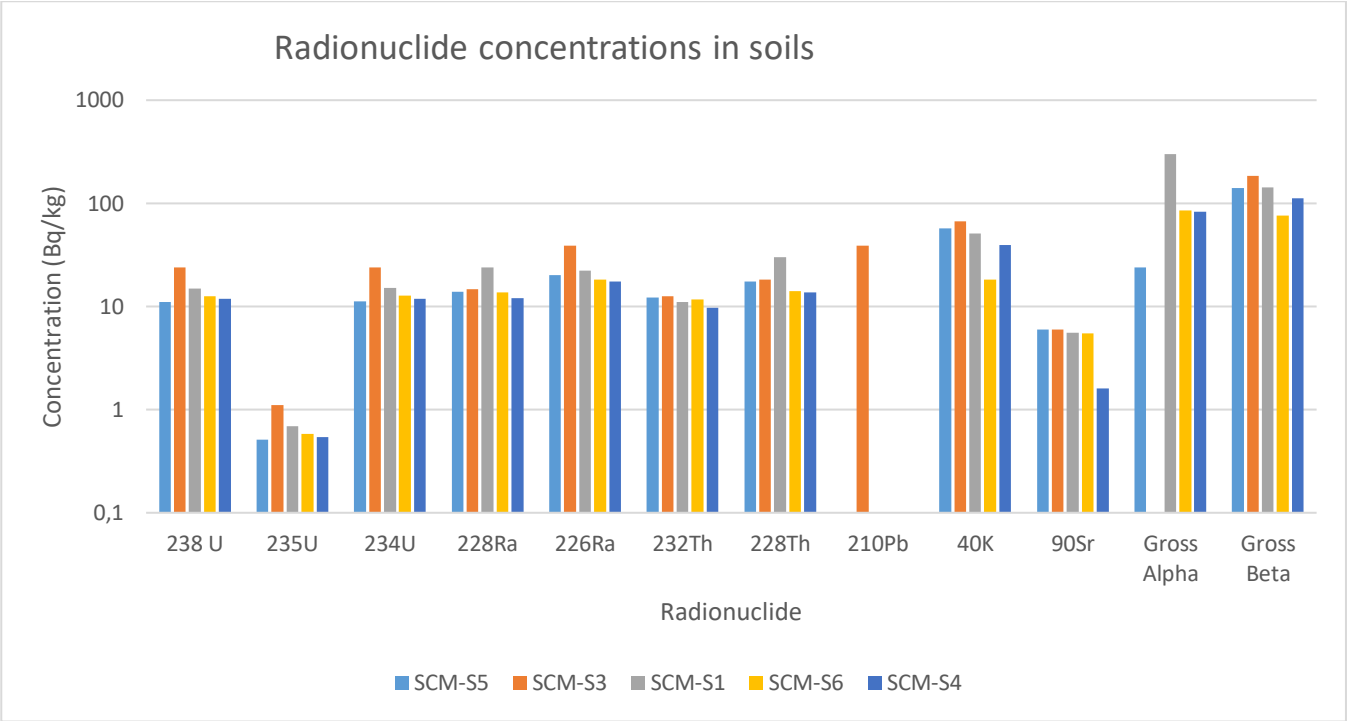

Figure 4.44. Radionuclide concentrations in soil samples from the Thyspunt area

4.9.5. Uranium, thorium and lead concentrations in soil

The radioactive trace metal concentrations in soils from the ICP-MS analysis are presented in Table 4.19. Uranium concentration in soils show a narrow range between 0.707 ppm (SCM-S5) and 1.741 ppm (SCM-S3), (ave.1.003 ppm). The uranium-rich soil sample SCM-S3 is located in the footprint area. The geology around the footprint area is characterised by elevated concentrations of uranium and hence, the local geology could be a source of the elevated uranium concentration in the soil. All other samples exhibit similar uranium concentrations that are slightly lower than that of SCM-S3, as indicated on the uranium proportion map in Figure 4.45. Lead concentration in the soils ranges from 2.812 ppm (SCM-S6) to 4.037 ppm (SCM-S1) (ave. 3.331 ppm). The soil sample SCM-S1 was sampled from a shale quarry, where Baviaanskloof Formation shales dominate (Table 4.11). Additionally, the radioactive decay of uranium and thorium in both the soil and substratum could contribute to the lead concentration in the sampled soil. Figure 4.46 shows that higher lead concentrations in soils exist where shale dominates the underlying geology. The thorium concentration range is 1.633 (SCM-S3) to 3.371 ppm (SCM-S2). Sample SCM-S2 is from outside Rosa Farm, an area dominated by thorium and uranium-rich sandstones and shales of the TMG. The elevated thorium concentration is likely a result of the local geology that is possibly the parent rock of the soil. Interestingly, soil sample SCM-S3 has the lowest concentration of thorium and lead, although it has the highest concentration of the parent element, uranium. Higher thorium concentrations appear to be in areas dominated by shale lithologies (Figure 4.47).

Table 4.19: Radioactive trace metal concentration in soils from Thyspunt

Sample Code	Pb (ppm)	Th (ppm)	U (ppm)
SCM-S1	4.037	2.91	1.056
SCM-S2	4.034	3.371	1.076
SCM-S3	3.065	1.633	1.741
SCM-S4	3.32	2.201	0.918
SCM-S5	2.821	2.985	0.707
SCM-S6	2.812	1.96	0.756
SCM-S7	3.229	2.237	0.768
Minimum	2.812	1.633	0.707
Maximum	4.037	3.371	1.741
Average	3.331	2.471	1.003

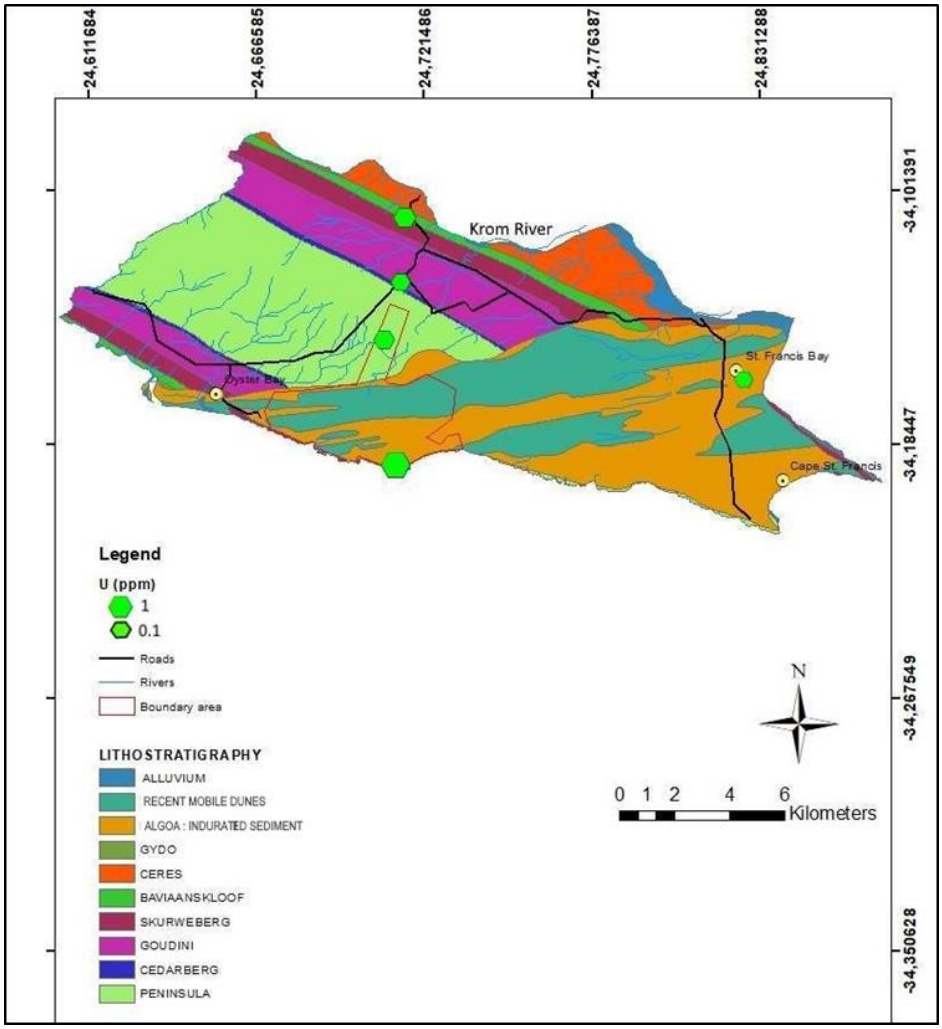

Figure 4.45: Uranium concentration proportion map

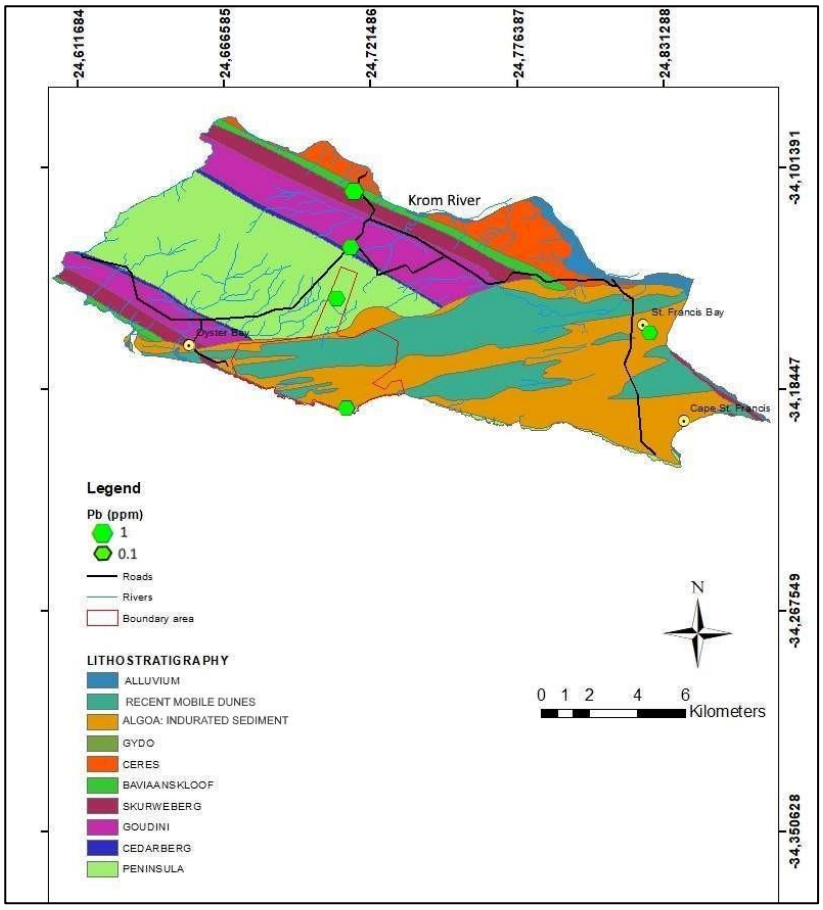

Figure 4.46: Lead concentration proportion map (Units: ppm).

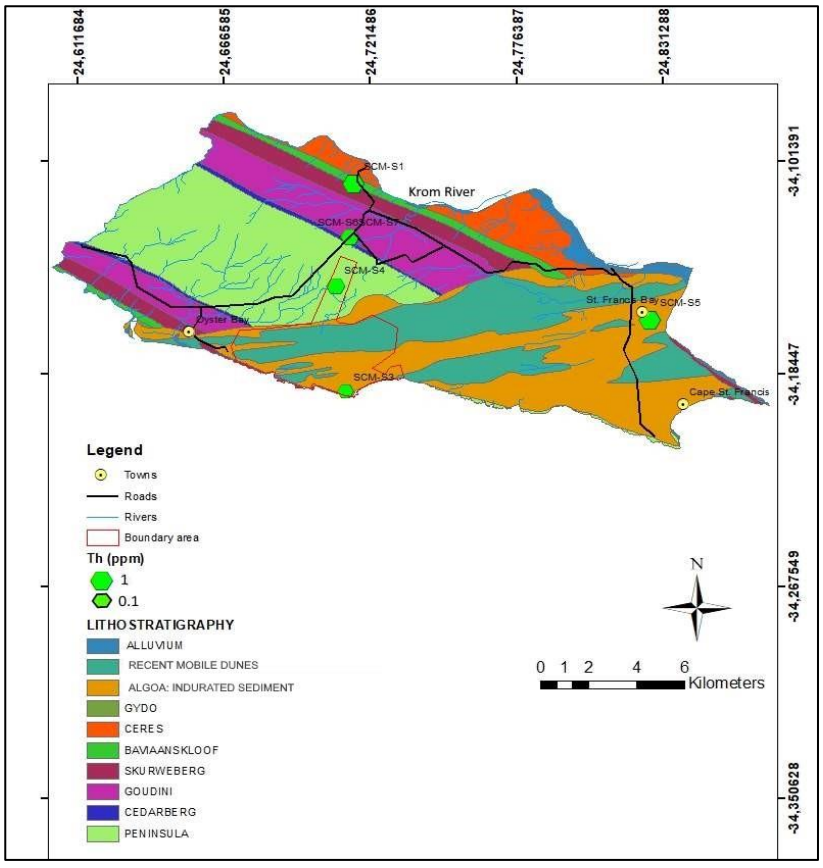

Figure 4.47: Thorium concentration proportion map

4.9.6. NORM in rocks

The NORM results for the six rock samples are presented in Table 4.20. A broad range of activity concentrations is evident in all the measured radionuclides. ^{238}U, the parent radionuclide, ranges between 1.06 Bq/kg (quartz vein) and 35.2 Bq/kg (quartzite), with the highest concentrations in the Skurwerburg Formation quartzite (S34.18314; E024.68345). A similar range was observed for ^{234}U (1.07 – 35.5 Bq/kg), the first uranium progeny of ^{238}U. Although quartz vein was sampled from the same area (footprint area) within the quartzite, the difference in radionuclide chemistry was attributed to the difference in the sources of the fluids that crystallized as a vein. The Skurwerburg Formation quartzite contains the highest activity concentrations of ^{238}U, ^{234}U, ^{226}Ra ^{210}Pb, ^{235}U, ^{232}Th and Gross alpha activity as presented in Figure 4.48. This quartzite acts as one of the productive aquifers in the area, and therefore, poses a great risk to the quality of the groundwater in the area with respect to radionuclides.

^{228}Ra is a highly toxic radionuclide and ranges between 10 and 83.3 Bq/kg in the sampled rocks. The Skurwerburg Formation quartzite has the highest concentration of ^{228}Ra and, therefore, poses a great risk to the groundwater quality and to some extent, the environment. This risk is further compounded by the emission of Radon (^{222}Rn), a radiogenic product of ^{228}Ra (and uranium) that is released into the water and air during radioactive decay (Ojovan and Lee, 2014). Elevated ^{228}Ra concentrations (72 Bq/kg) are also observed in sample SCMR4, a shale from the Bokkeveld Group's Ceres Subgroup. The shale outcrop also contains the highest concentration of ^{40}K (1050 Bq/kg), which is above the average NORM value of 800 Bq/kg. Additionally, shale has the highest gross beta activity of 1330, and this is largely attributed to elevated concentrations of ^{228}Ra and ^{40}K. The shale outcrop generally contains elevated concentrations of the radionuclides (Figure 4.48) and is, therefore, potentially detrimental to the environment. This is especially true because the shale sample was collected from a quarry pictured in Figure 4.49. The emission of radon from the radium and uranium also potentially poses a risk to the environment if the shale is used in any activity at the ESKOM site that could potentially mask any oversight during the power station operation

Table 4.20: Radionuclide concentration in rocks from the Thyspunt area

Sample code	**^{238}U**	**^{235}U**	**^{234}U**	**^{226}Ra**	**^{210}Pb**	**^{232}Th**	**^{228}Ra**	**^{228}Th**	**^{40}K**	**Gross Alpha**	**Gross Beta**
SCM-R10	4.59	0.211	4.63	6.24	<MDA	4.22	<MDA	4.9	41,5	190	85.5
SCM-R4	34.1	1.57	34.4	26.6	<MDA	63.7	72	86.5	1050	130	1330
SCM-R5	1.06	0.049	1.07	3.15	<MDA	0.84	<MDA	<MDA	<MDA	390	15
SCM-R3	5.57	0.256	5.61	7.06	<MDA	7.51	10	9.2	43,2	564	92,7

SCM-R1	35.2	1.62	35.5	38.3	62,5	65.7	83.3	108	281	654	599
SCM-R2	5.06	0.233	5.1	9.32	<MDA	8.6	<MDA	7.3	35,9	59	98.7
Minimum	1.06	0.049	1.07	3.15	62,5	0.84	10	4.9	35,9	59	15
Maximum	35.2	1.62	35.5	38.3	62,5	65.7	83.3	108	1050	654	1330
Average	14.26	0.657	14.39	15.11	62,5	25.095	55.1	43.18	290,32	331.167	370.15

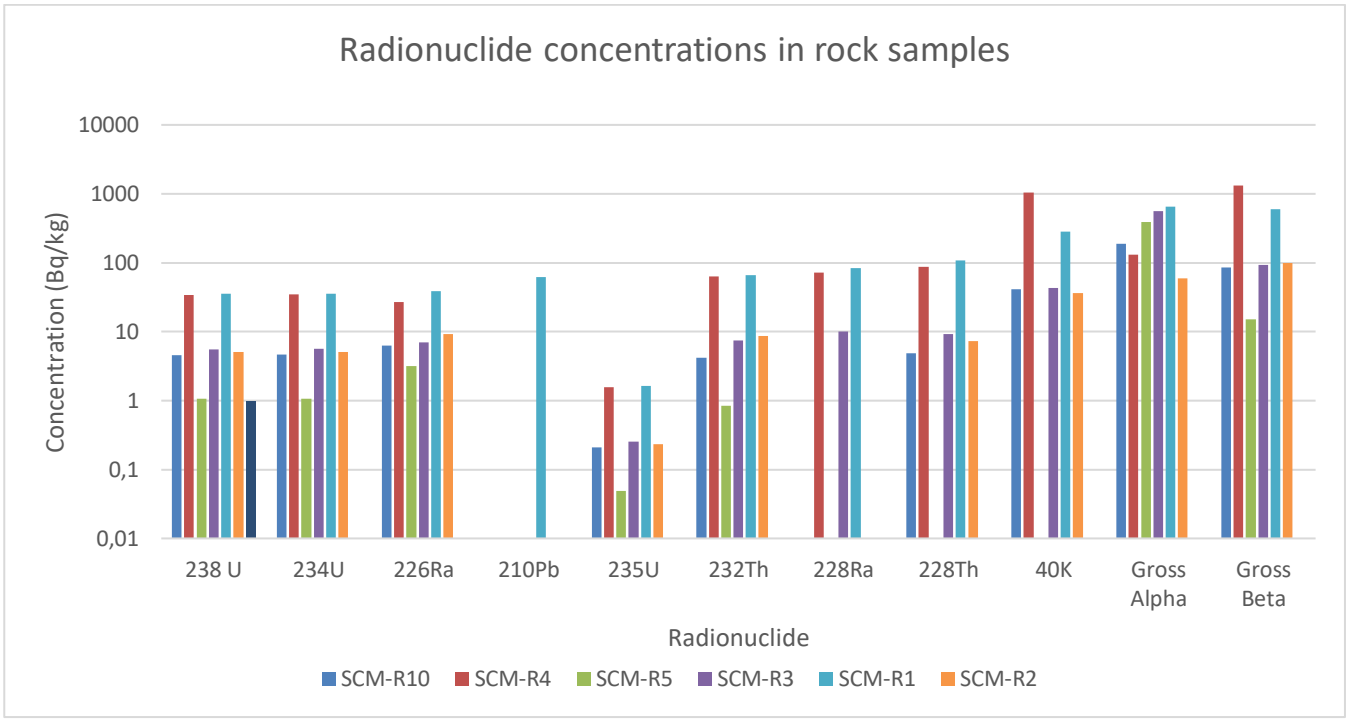

Figure 4.48. Radionuclide concentrations in rock samples from the Thyspunt area

Figure 4.49. Organic shale outcrop in the quarry site (Courtesy: Prof. Tamiru Abiye)

4.9.7. Lead, uranium and thorium concentrations in rocks

The radioactive trace metal concentrations in rocks from the ICP-MS analyses are presented in Table 4.21. The sampling locations of the analysed rocks are presented in Figure 4.50. The results indicate that lead concentrations range between 1.611 (quartzite) and 23.053 (shale) ppm (ave. 9.425 ppm). The lead-rich shale belongs to the Bokkeveld Group's Ceres Subgroup, and was sampled from the shale quarry (S34.18314, E024.68345). The shale sample (SCM-R8) from the Baviaanskloof Formation also contains elevated lead concentration in the range of 17.865 ppm. The elevated lead concentrations are most likely a result of the radioactive decay of uranium and thorium in the host rocks. The lead concentration proportion map indicates the elevated concentrations in shale and low concentrations in quartzite, with the exception of the Skurwerburg Formation quartzite (Figure 4.51).

The concentration of uranium in the sampled rocks ranges between 0.116 (quartz vein) and 2.673 (quartzite) ppm. The uranium-rich quartzite is from the Skurwerburg Formation, which is characterised by elevated uranium concentrations. Shale samples SCM-R4 (Ceres Subgroup) and SCM-R8 (Baviaanskloof Formation) also exhibit elevated concentrations of uranium, which is 2,622 ppm and 2.495 ppm, respectively. A uranium concentration proportion map is presented in Figure 4.52. Elevated uranium concentrations are mainly encountered in shales located in the north /north-western sections of the study area. Thorium concentrations range from 0.439 (quartz vein) to 22.132 (quartzite) ppm, and mean concentration of 6.677 ppm. The thorium-rich quartzite belongs to the Skurwerburg Formation. Shale samples (SCMR4 and R8) also contain elevated concentrations of thorium (15.572 and 10.26 ppm respectively), a progeny of the radioactive decay of uranium. This is further supported by the elevated uranium concentrations in the aforementioned shale samples. A thorium concentration proportion map is presented in Figure 4.53. Like the other radionuclides, high thorium concentrations are encountered in the Skurwerburg Formation, Baviaanskloof Formation and Ceres Subgroup.

Table 4.21: Radioactive trace metal concentration in rocks from Thyspunt

Sample	Pb (ppm)	Th (ppm)	U (ppm)
SCM-R1	15.02	22.132	2.673
SCM-R2	4.34	2.471	0.556
SCM-R3	4.471	1.803	0.658
SCM-R4.1	20.961	7.037	2.622
SCM-R4.2	23.053	15.572	2.617
SCM-R5	3.155	0.439	0.116
SCM-R6	5.988	5.286	1.101
SCM-R7	4.887	2.722	0.744

SCM-R8	17.865	10.26	2.495
SCM-R9	1.611	0.93	0.264
SCM-R10	2.547	0.813	0.24
SCM-R11	3.386	1.444	0.307
Minimum	**1.611**	**0.439**	**0.116**
Maximum	**23.053**	**22.132**	**2.673**
Mean	**9.425**	**6.677**	**1.227**

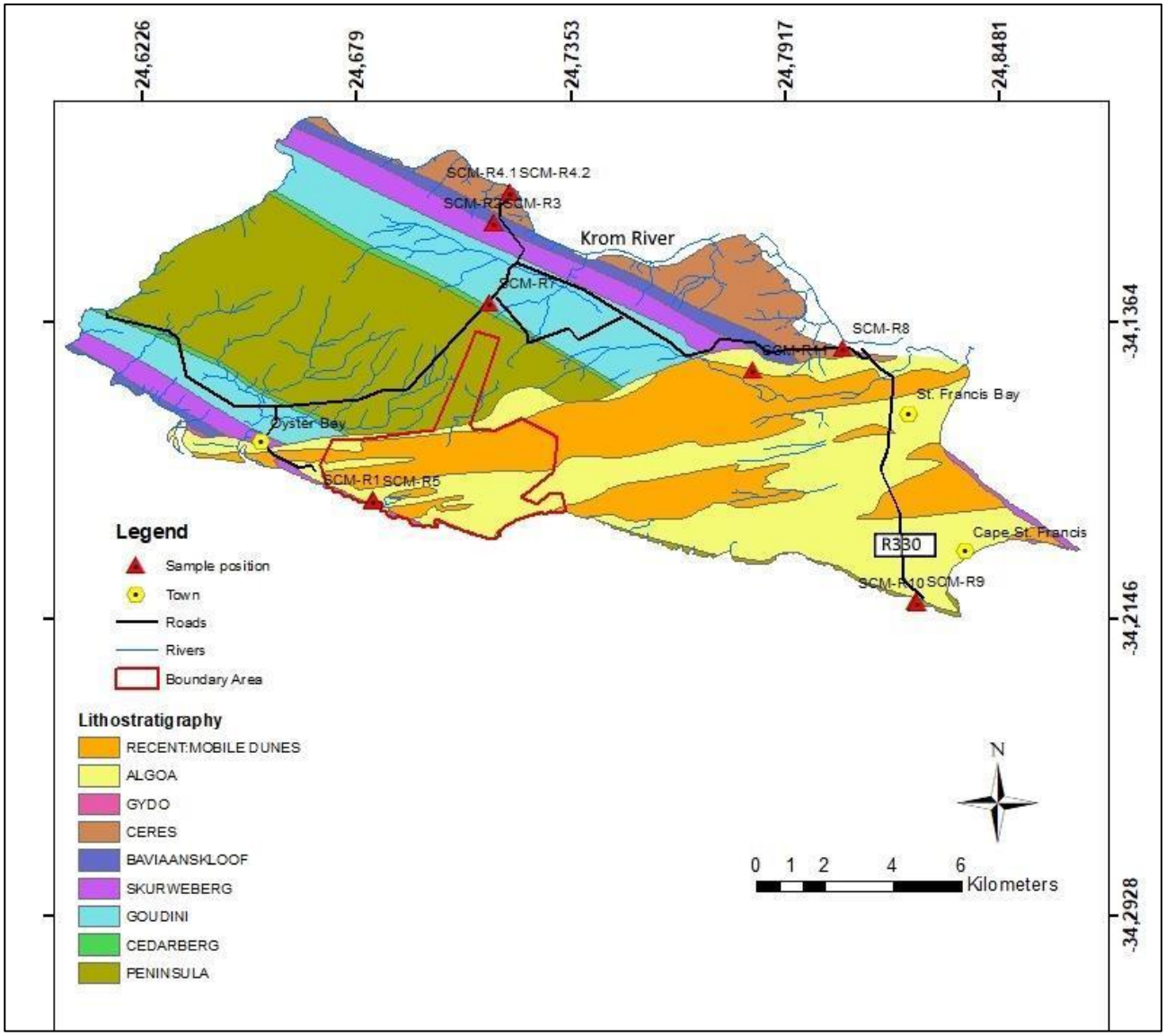

Figure 4.50: Rock sampling points in the Thyspunt area

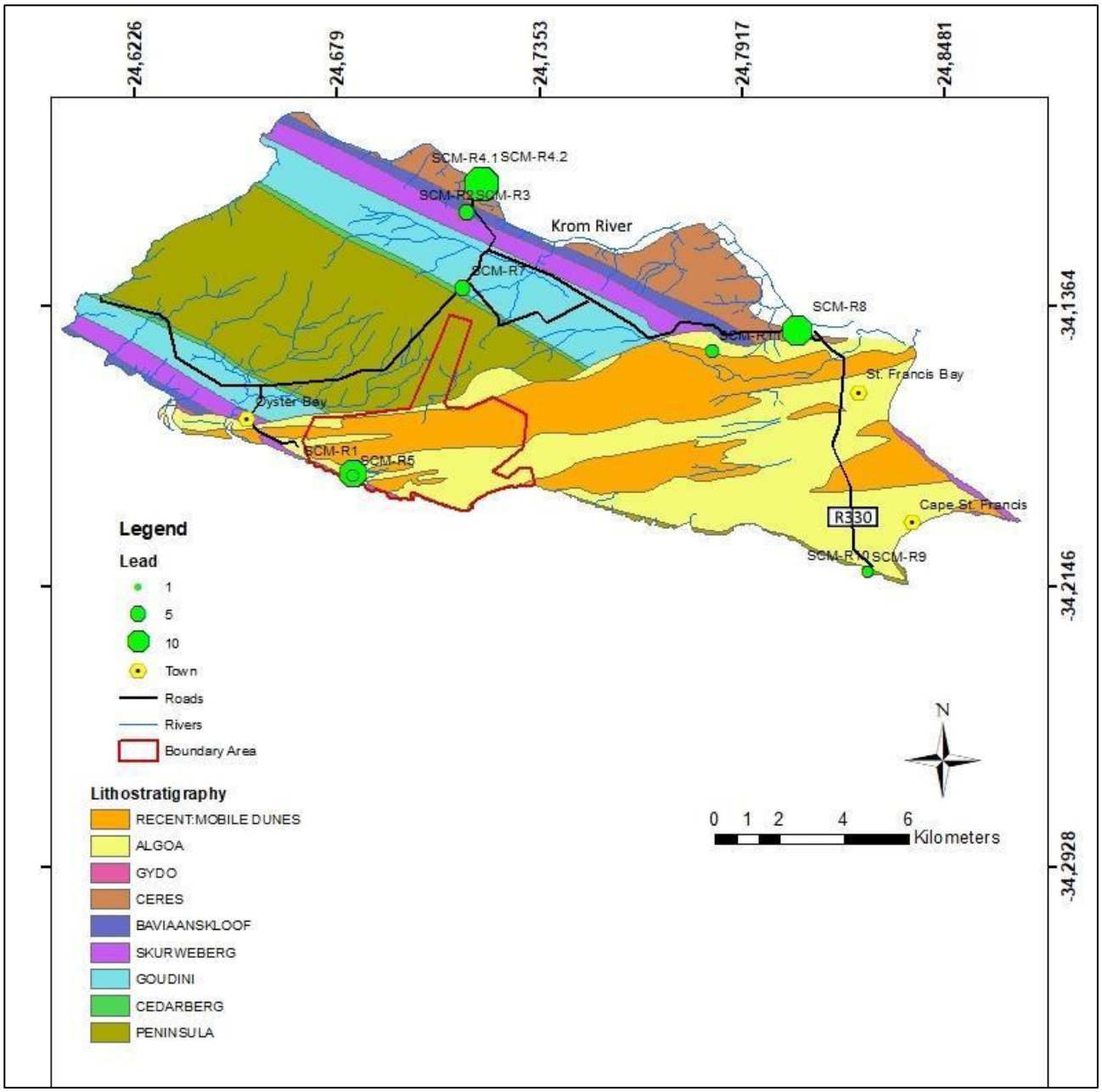

Figure 4.51. Lead concentration proportion map (Units: ppm).

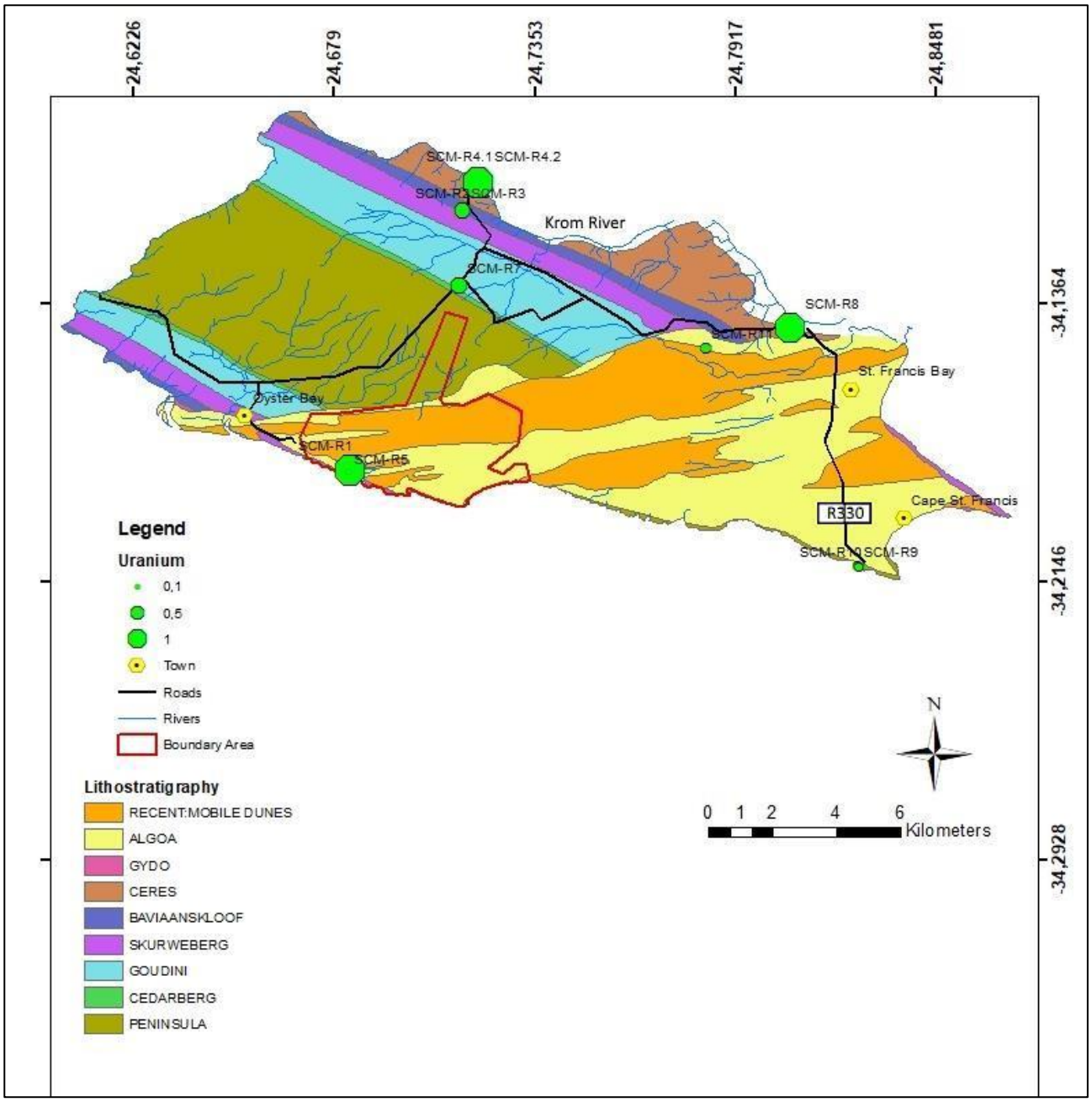

Figure 4.52. Uranium concentration proportion map (units: ppm).

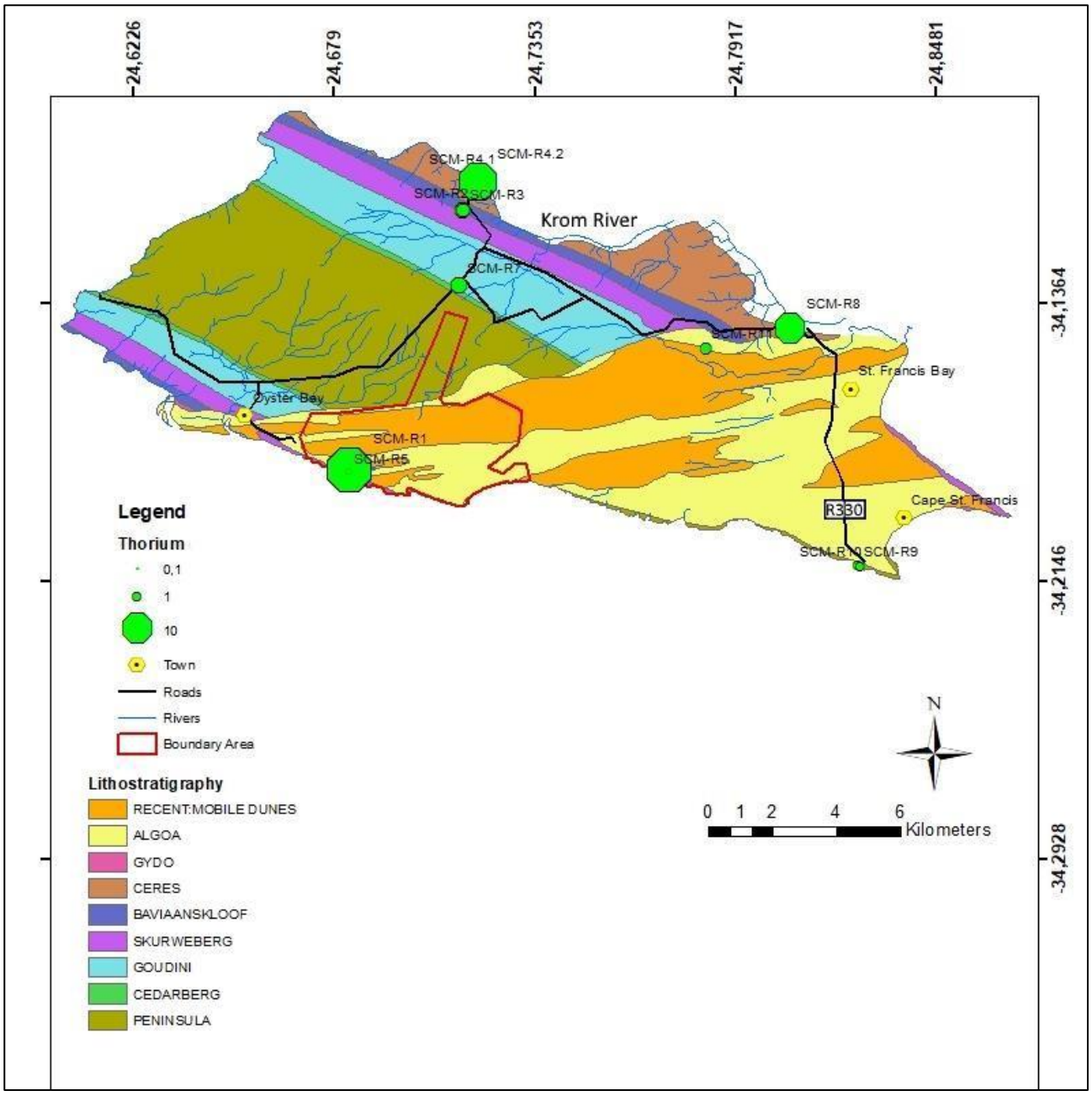

Figure 4.53. Thorium concentration proportion map (Units: ppm).

4.9.8. Effective dose in water

Human beings are constantly subjected to background radiation emanating from both natural and anthropogenic sources. According to the IAEA (1996), about 80% of the total radiation that a person is exposed to annually is sourced from NORM radiation. The study of natural/background radioactivity is, therefore, of paramount importance as it provides information about the current levels of potentially harmful radionuclides that are present in the environment or tissues of living creatures (Al-Kharouf *et al.*, 2008). Additionally, understanding of the radionuclide behaviour provides information that can serves as the base for radioactivity assessment and monitoring. This can further be used for policy-making and protection of living organisms and the environment as a whole. One

way in which the extent to which human being are affected by radiation energy is determined is through the effective dose. According to the ICRP Publication 119 (2012), effective dose is defined as the sum of the weighted equivalent doses in all tissues and organs of the body. Effective dose is given by the expression (ICRP, 2012):

$$E\ (Sv/l) = eA \qquad (Equation\ 5)$$

Where:

E is the effective (Sv/L or Sv/kg)

e is the effective dose conversion factor (Sv/Bq)

A is the activity concentration (Bq/kg or Bq/L)

^{238}U, ^{235}U, ^{234}U, ^{226}Ra, ^{224}Ra and ^{223}Ra activity concentrations were determined in eight unfiltered, raw water (groundwater, spring and ocean samples) that were collected with 1 L high density plastic bottle. Boreholes were purged from 5 to 10 minutes before sampling. The activity concentrations of the eight water samples are presented in Table 4.22. Ingestion effective dose conversion factors from the ICRP Publication 119 were used in calculating the effective doses. The publication presents male and female effective dose conversion factors for all uranium radioisotopes, and therefore, effective doses for both males and females were determined. This is because there are slight differences in the response of males and females to radiation. Only male ingestion effective doses for ^{226}Ra, ^{224}Ra and ^{223}Ra were determined, since the publication only presents male dose conversion factors.

Results

For the purpose of this report, effective dose was calculated in µSv/L or µSv/kg. Ingestion male and female effective doses are presented in Table 4.22 and 4.23 respectively. The effective doses from the ingestion of ^{238}U in males ranges between 0.13376 and 38.456 µSv/L, with a mean effective dose of 4.5942 µSv/L. The highest effective dose is related to groundwater sample SCM08, located in the Eskom Site. The lowest effective dose is associated with groundwater sample SCM33, from an iron-rich, artesian system. The effective dose for female ^{238}U ranges between 7.744×10^{-7} and 0.00022264 µSv/L, with a mean effective dose of 2.9826×10^{-5} µSv/L. Like the male effective dose for ^{238}U, the highest female effective dose for ^{238}U is associated with groundwater sample SCM08, while the lowest effective is associated with groundwater sample SCM33. The difference in effective doses between the two genders is a result of the difference in effective dose coefficients, which is higher for female. The male effective dose for ^{235}U ranges between 6.71×10^{-9} and 1.93×10^{-6} µSv/L, and an average effective dose of 2.31×10^{-7} µSv/L. In contrast, female effective dose for ^{235}U ranges between

6.71 x10^{-9} and 1.93 x10^{-6} µSv/L, with an average effective dose of 2.31 x10^{-7} µSv/L. Like ^{238}U, the highest effective dose is related to groundwater sample SCM08. Additionally, the lowest ^{238}U male effective dose is related to the groundwater sample SCM33 from an artesian system. ^{234}U male effective dose ranges from 1.05 x10^{-7} to 4.01 x10^{-5} µSv/L, with a mean effective dose of 4.83 x10^{-6} µSv/L. In contrast, for female the ^{234}U effective dose ranges from 1.05 x10^{-7} to 4.01 x10^{-5} µSv/L, and a mean effective dose of 4.83 x10^{-6} µSv/L. Similar to other uranium isotope effective doses, the highest effective dose is related to groundwater sample SCM08, while the lowest effective dose is related to groundwater sample SCM33. Sample SCM08 yields the highest effective dose for all the uranium isotopes and, therefore, humans should be cautioned against the use of this water.

Radium isotopes, particularly ^{226}Ra and ^{228}Ra are the most radiotoxic and hazardous radionuclides when ingested, and this is because of the behavioural similarities it has with calcium. Therefore, once ingested, it can assimilate into the bones (Altıkulac *et al.*, 2015). The ^{226}Ra effective dose for male is in the range of 3.08 x10^{-7} and 4.12 x10^{-5} µSv/L, with an average effective dose of 1.16 x10^{-5} µSv/L. Groundwater sample SCM17 from the Eskom site yields the lowest effective dose in males. This is likely a result of the relatively low Radium-226 content in the aquifer (sand dune) from which the groundwater was sampled. Interestingly, the highest effective dose is related to groundwater sample SCM33 from an artesian system. Although groundwater sample SCM17 has the lowest ^{238}U effective dose, this groundwater has elevated ^{226}Ra effective dose. This is possibly a result of the oxic nature of the groundwater that promotes ^{226}Ra solubility and mobility in water. ^{238}U and ^{226}Ra have different chemical properties and thus, their mobility and solubility in water vary. Additionally, ^{226}Ra has a higher effective dose coefficient than ^{238}U. Extreme caution therefore, should be taken regarding the ingestion of this groundwater since the samples were collected from household boreholes. The ^{224}Ra effective doses for male range from 1.5 x10^{-7} to 1.08 x10^{-6} µSv/L, with a mean dose of 4.97 x10^{-7} µSv/L. The highest effective dose is associated with groundwater sample SCM33, and is attributed to the elevated ^{224}Ra concentration in water. Interestingly, ocean sample SCM440 has the lowest ^{224}Ra effective dose and this is a result of the low (2.4Bq/L) ^{224}Ra concentration. Since ocean water typically contains relatively elevated concentrations of trace elements, the analysed ocean water contains low concentrations of ^{224}Ra. ^{223}Ra effective doses in males range between 7 x10^{-8} and 5.8 x10^{-7} µSv/L. Although lower values are reported in the table, these values are negative and are a result of the negative ^{223}Ra concentrations. These values have therefore been disregarded, as they are a result of analytical/machine error. The highest ^{223}Ra effective dose is associated with groundwater sample SCM17 from the Eskom Site. Although this sample has the highest effective dose of ^{223}Ra, it is the smallest effective dose relative to all other radionuclides' maximum effective doses. This is because ^{223}Ra is a member of the uranium-235 decay series, and therefore, seldom occurs in the environment in high concentrations.

Table 4.22: Male ingestion effective dose in eight water samples

Sample code	**e^{238}U (µSv/L)**	***$e^{235}U$* (µSv/L)**	***$e^{234}U$* (µSv/L)**	**e^{226}Ra (µSv/L)**	***$e^{224}Ra$* (µSv/L)**	***$e^{223}Ra$* (µSv/L)**
SCM33 (Groundwater)	0.13376	6.71×10^{-9}	1.05×10^{-7}	4.12×10^{-5}	1.08×10^{-6}	-8.4×10^{-8}
SCM41(Ocean water)	0.39748	2×10^{-8}	5.44×10^{-7}	1.32×10^{-6}	3.25×10^{-7}	5.33×10^{-7}
SCM40 (Ocean water)	0.36708	1.85×10^{-8}	3.77×10^{-7}	1.79×10^{-6}	1.5×10^{-7}	-2.5×10^{-7}
SCM45 (Groundwater)	0.58596	2.95×10^{-8}	7.85×10^{-7}	1.92×10^{-5}	7.93×10^{-7}	-5.1×10^{-7}
SCM17(Groundwater)	0.30096	1.51×10^{-8}	3.64×10^{-7}	3.08×10^{-7}	4.65×10^{-7}	5.8×10^{-7}
SCM32(Groundwater)	0.323	1.63×10^{-8}	4.59×10^{-7}	6.75×10^{-6}	4.71×10^{-7}	7×10^{-8}
SCM08 (Groundwater)	38.456	1.93×10^{-6}	4.01×10^{-5}	3.19×10^{-5}	6.89×10^{-7}	-3.1×10^{-7}
SCM09(Groundwater)	0.6498	3.3×10^{-8}	6.43×10^{-7}	1.79×10^{-6}	3.51×10^{-7}	2.8×10^{-7}
Minimum	**0.13376**	**6.71×10^{-9}**	**1.05×10^{-7}**	**3.08×10^{-6}**	**1.5×10^{-7}**	**-5.1×10^{-7}**
Maximum	**38.456**	**1.93×10^{-6}**	**4.01×10^{-5}**	**4.12×10^{-5}**	**1.08×10^{-6}**	**5.8×10^{-7}**
Mean	**4.5942**	**2.31×10^{-7}**	**4.83×10^{-6}**	**1.16×10^{-5}**	**4.97×10^{-7}**	**-2.2×10^{-8}**

Table 4.23: Female ingestion effective dose in eight water samples

Sample code	***e^{238}U*(µSv/L)**	***e^{235}U*(µSv/L)**	**e^{234}U(µSv/L)**
SCM33 (Groundwater)	7.744×10^{-7}	3.72×10^{-8}	6.22×10^{-7}
SCM41 (Ocean water)	2.3012×10^{-6}	1.11×10^{-7}	3.21×10^{-6}
SCM40 (Ocean water)	2.1252×10^{-6}	1.03×10^{-7}	2.22×10^{-6}
SCM45 (Groundwater)	3.3924×10^{-6}	1.63×10^{-7}	4.64×10^{-6}
SCM17 (Groundwater)	1.7424×10^{-6}	8.37×10^{-8}	2.15×10^{-6}
SCM32 (Groundwater)	0.00000187	9.02×10^{-8}	2.71×10^{-6}
SCM08 (Groundwater)	0.00022264	1.07×10^{-5}	0.000237
SCM09 (Groundwater)	3.762×10^{-6}	1.83×10^{-7}	3.8×10^{-6}
Minimum	**7.744×10^{-7}**	**3.72×10^{-8}**	**6.22×10^{-7}**
Maximum	**0.00022264**	**1.07×10^{-5}**	**0.000237**
Mean	**2.9826×10^{-5}**	**1.44×10^{-6}**	**3.2×10^{-5}**

4.10. CONCEPTUAL HYDROGEOLOGICAL MODEL FOR THE THYSPUNT AREA

A conceptual hydrogeological model of Thyspunt is proposed and is based on the analysis and interpretation of geological, hydrogeological, hydrochemical and environmental isotope data. The model was constructed on the basis of the N-S cross sectional line indicated in Figure 2.3. The average annual precipitation of Thyspunt area is 621.47 mm, which is based on the 1980 to 2018 rainfall data, with average PET and AET of 821.5 and 535.93 mm/year, respectively. The annual potential evapotranspiration exceeds the annual precipitation in the area and hence, recharge could take place from exceptionally high rainfall within a short duration. Annual recharge estimated from the WTF method ranges between 0.588 and 72.183 mm/year (ave. 36.092 mm/year). Groundwater flows from the inland towards the Indian Ocean and mainly discharges in the form of springs, although discharge as baseflow into wetlands has been noted.

Based on lithological logs and aquifer properties, multiple hydrostratigraphic units exist in the area. Unconfined, intergranular aquifers composed of dunes occur at shallow depth, in addition to the unconfined, fractured aquifers of the TMG, and aquifer thickness ranges between 12.85 – 75.97 m, with minimum groundwater level of 3.53 m.b.g.l. Confined, fractured aquifers of the Goudini and Skurwerburg Formations occur at along the fold limb and are occasionally overlain by the unconfined, intergranular aquifers (Figure 4.54). The siltstone and shale units of the Ceres Subgroup and Baviaanskloof Formation act as the confining units to the confined aquifers. The general dip of the quartzites and shales of different Formations is to the southwest at 50 to 60° and the northeast at 28 to 44°, thereby favouring the interlayering of rocks with different aquifer properties responsible for the occurrence of confined aquifers in the area. At shallow depth, all quartzites behave as fractured aquifers, but confining comes to play at depth (Figure 4.54). Environmental isotopes and hydrochemical data indicate a strong link between most groundwater and springs, ascertaining that springs are a surface manifestation of groundwater. Furthermore, isotopic composition similarities between some groundwaters suggests a link between some aquifers. Intergranular aquifers are linked to lower fractured aquifers at depth through groundwater transfer from the intergranular aquifers into the lower fractured aquifers. The depleted isotopic signatures of all groundwater suggest recharge occurred during colder seasons or from rainfall with a high latitude moisture source. Moreover, groundwater flow lines indicate an ingress of groundwater from areas further inland, and hence, regional recharge dominates over local recharge. Numerous moisture sources are responsible for the water present in Thyspunt, with the most localised sources generating the winter rainfall. No seawater intrusion has been identified in the sampled aquifers, and this could be explained by the dip direction

of the rocks towards the ocean owing to folding, which hinders the ingress of seawater into the coastal aquifers. The Piper and Gibbs plots indicate the dominance of water-rock interactions in controlling the water chemistry. Furthermore, Ca – HCO_3^- is the dominant water facies and is largely attributed to the dissolution of carbonates in the local geology.

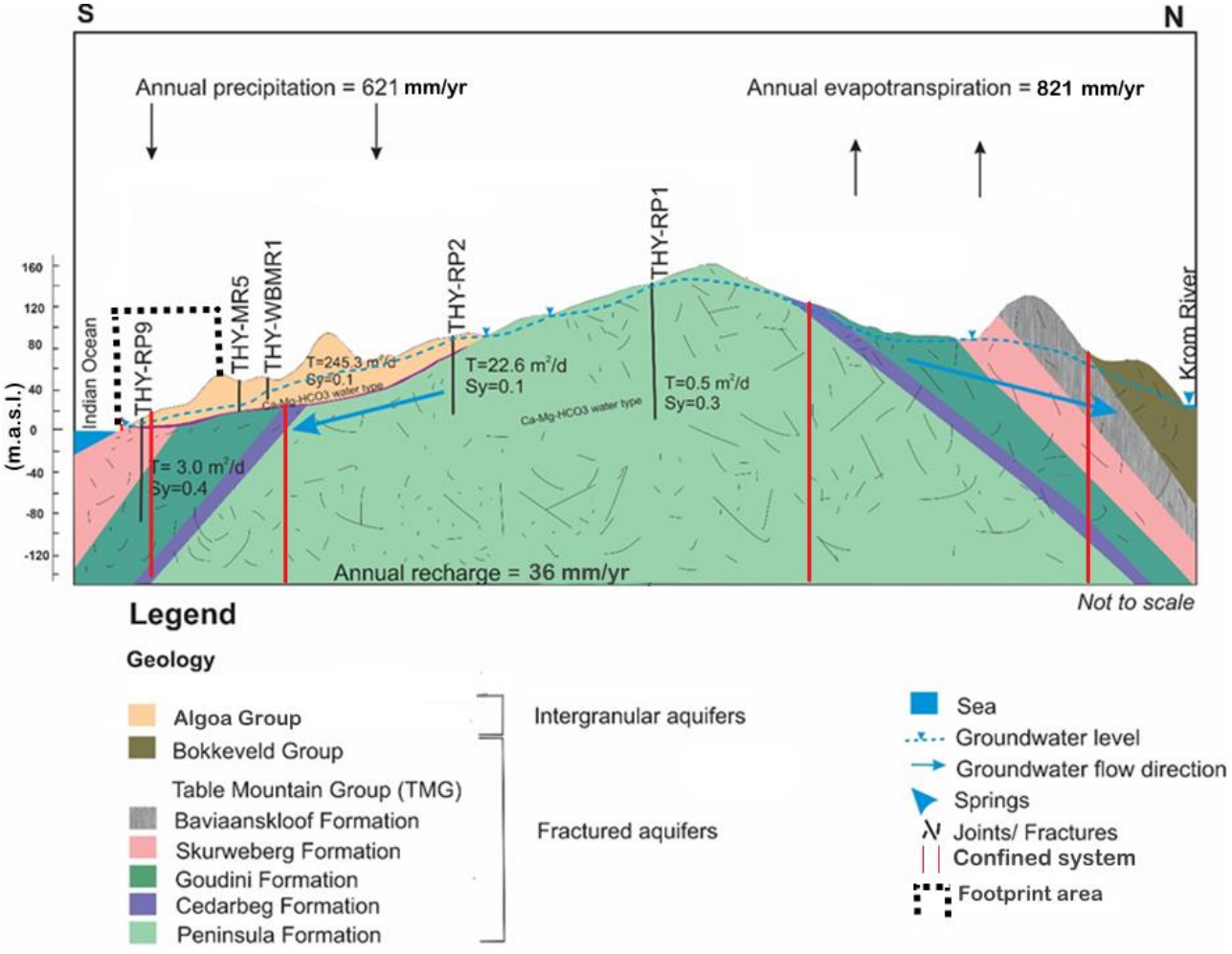

Figure 4.54 N-S conceptual model for Thyspunt (Courtesy: Moneri Modiba).

5. GROUNDWATER VULNERABILITY TO POLLUTION MAPPING

This chapter presents the results of the groundwater vulnerability to pollution mapping, thereby seeking to fulfil the second aim of this study. The results of each DRASTIC parameter are presented and discussed, together with the intrinsic and specific groundwater vulnerability to pollution maps.

5.1. Depth to groundwater

The measured groundwater depths in the area range between 3.53 and 28.87 m.b.g.l., with an average groundwater level of 13.31m.b.g.l. The majority of the study area is represented by groundwater levels that range between 10 and 20 m.b.g.l. (see Figure 5.1). The vulnerability rating associated with depth to groundwater ranges from 3 to 10 in the study area. In general, high vulnerability areas are located to the eastern/south-eastern parts of the study area, which is dominated by highly permeable, mobile dunes. The majority of the study area has a vulnerability rating of 5 (see Figure 5.2).

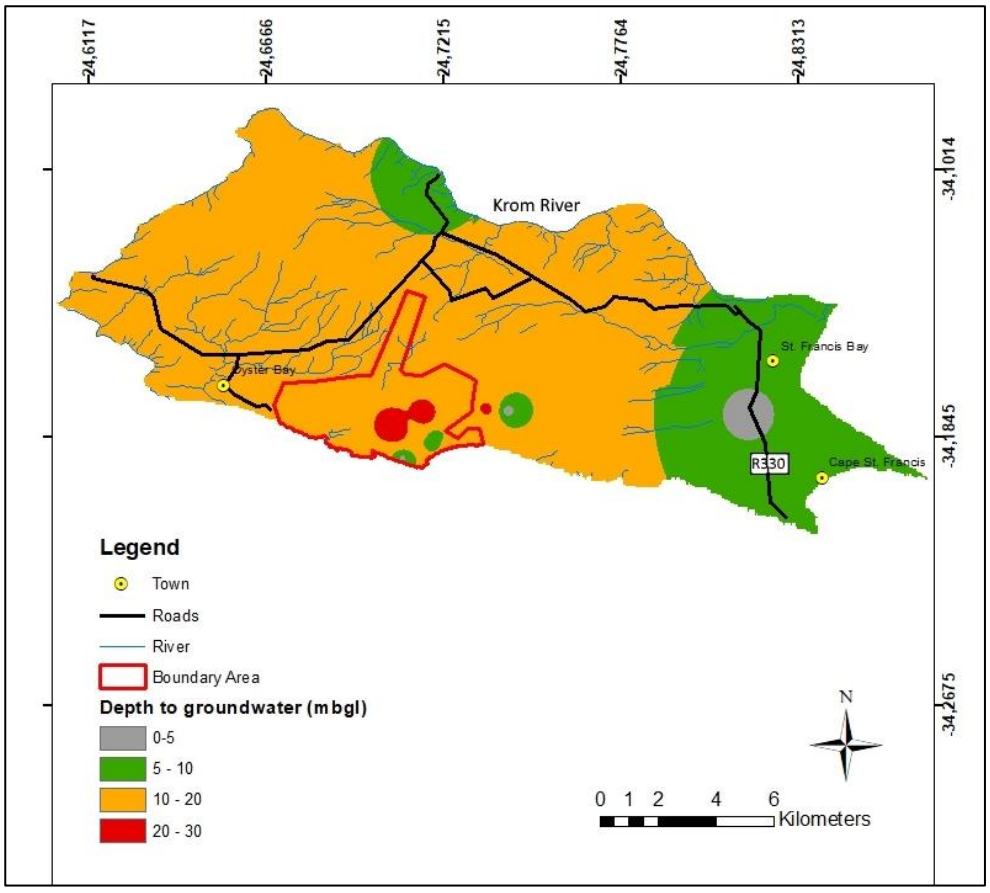

Figure 5.1. Depth to groundwater map

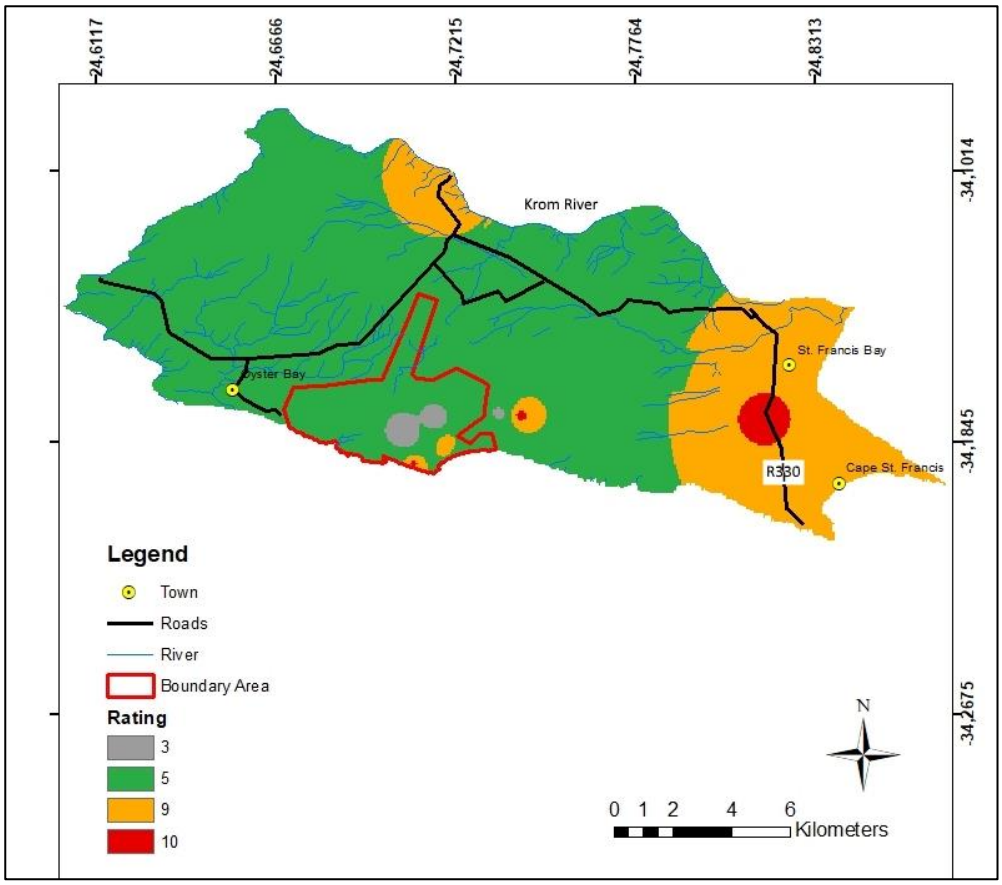

Figure 5.2. Depth to groundwater ratings.

5.2. Recharge

Two distinct recharge zones exist in the study area (Figure 5.3). About half of the study area receives an annual recharge of 153.8 mm/year. The other half is characterised by an average annual recharge of 68 mm/year. The ratings associated with recharge are 8 and 10 (Figure 5.4). The northern half of the study area is represented by a vulnerability rating of 8, whilst the southern half is represented by a vulnerability rating of 10. The coastal region has a vulnerability rating of 6.

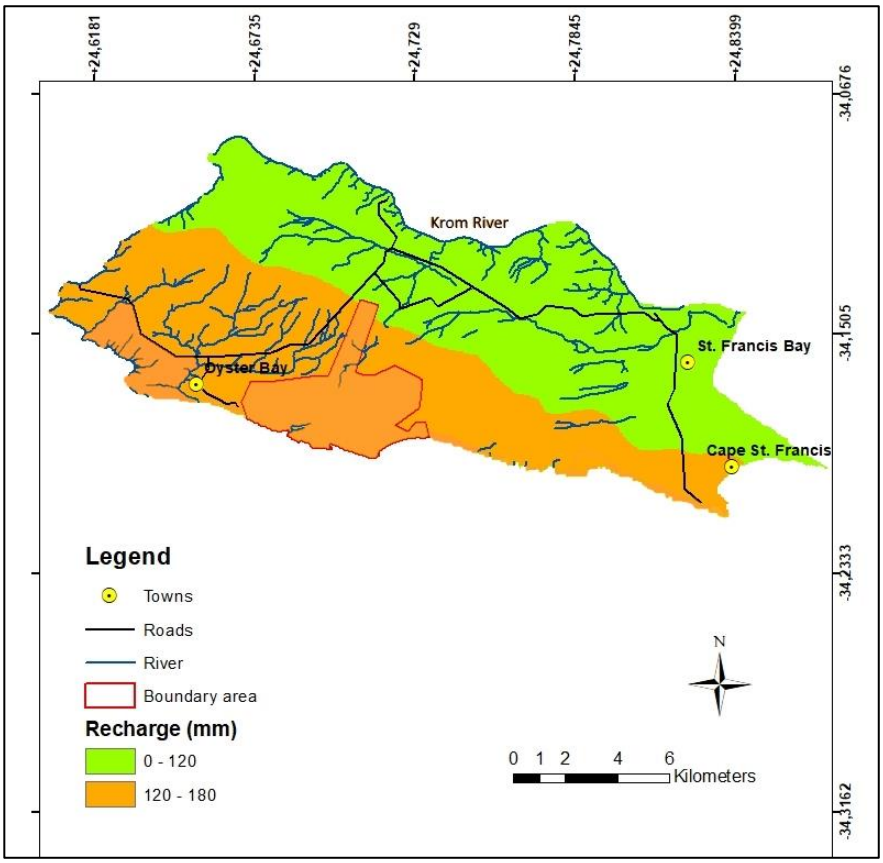

Figure 5.3. Annual recharge map.

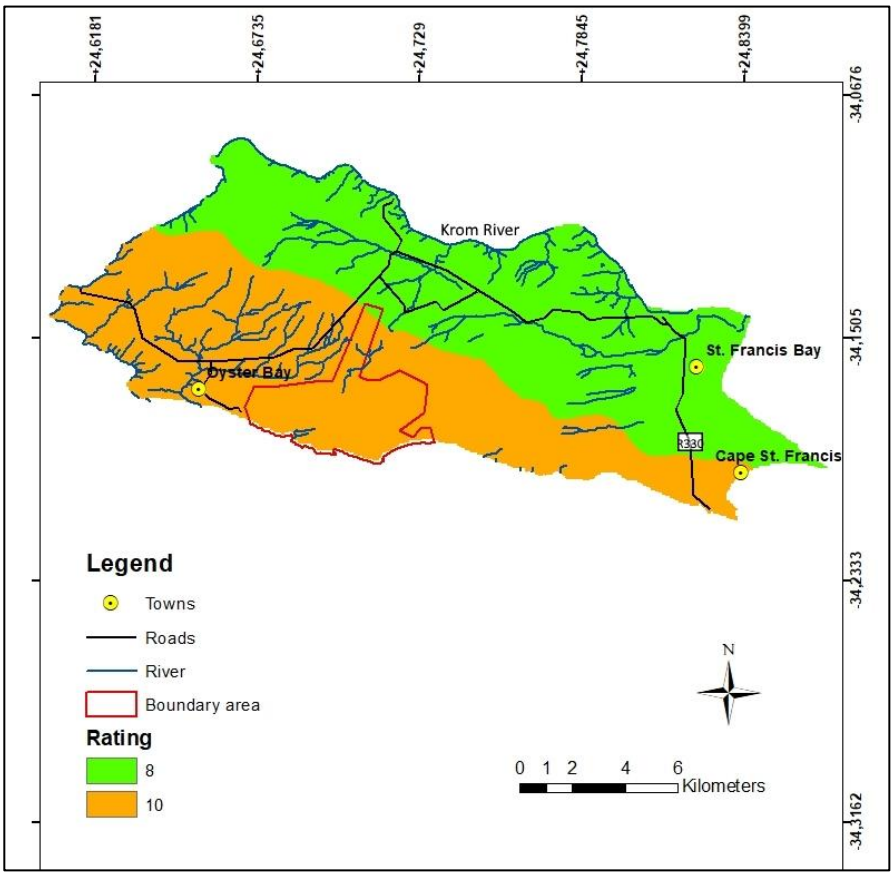

Figure 5.4. Recharge rating map

5.3. Aquifer media

The geological map of the study area shows that metasedimentary rocks (quartzite, metasandstone and shale) of the Table Mountain Group, Algoa Group sediments and aeolian deposits dominate the area. These lithologies comprise of the main aquifers in the study area (Figure 5.5). The vulnerability rating associated with aquifers ranges between 6 and 9 as indicated in Figure 5.6. The majority of the area is represented by a vulnerability rating of 9, which is associated with the alluvial, intergranular aquifers (dune-hosted). Fractured aquifers underlie the intergranular aquifers in the areas dominated by alluvial deposits on surface. The remainder of the study area is represented by vulnerability ratings of 6 and 7, and these are associated with shale and quartzite aquifers, respectively.

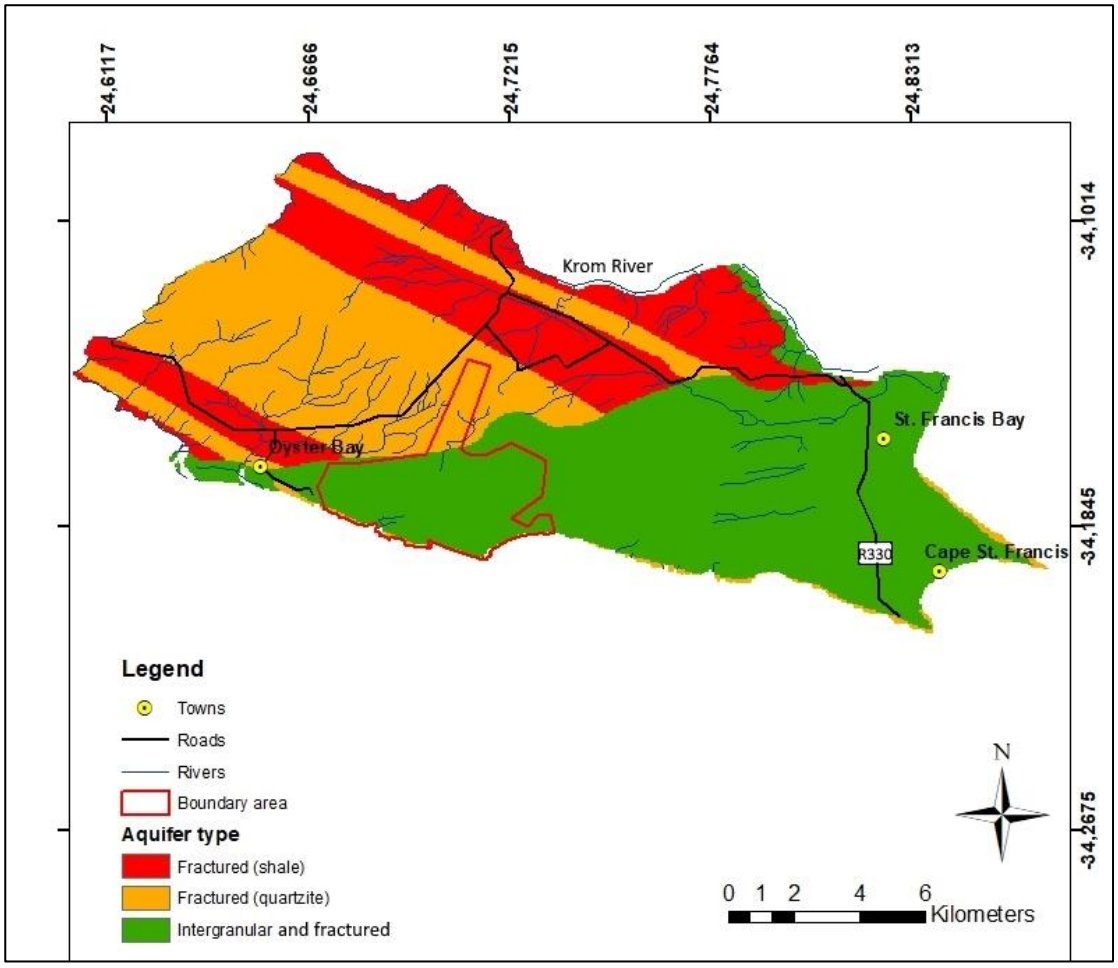

Figure 5.5. Aquifer map of the Thyspunt area.

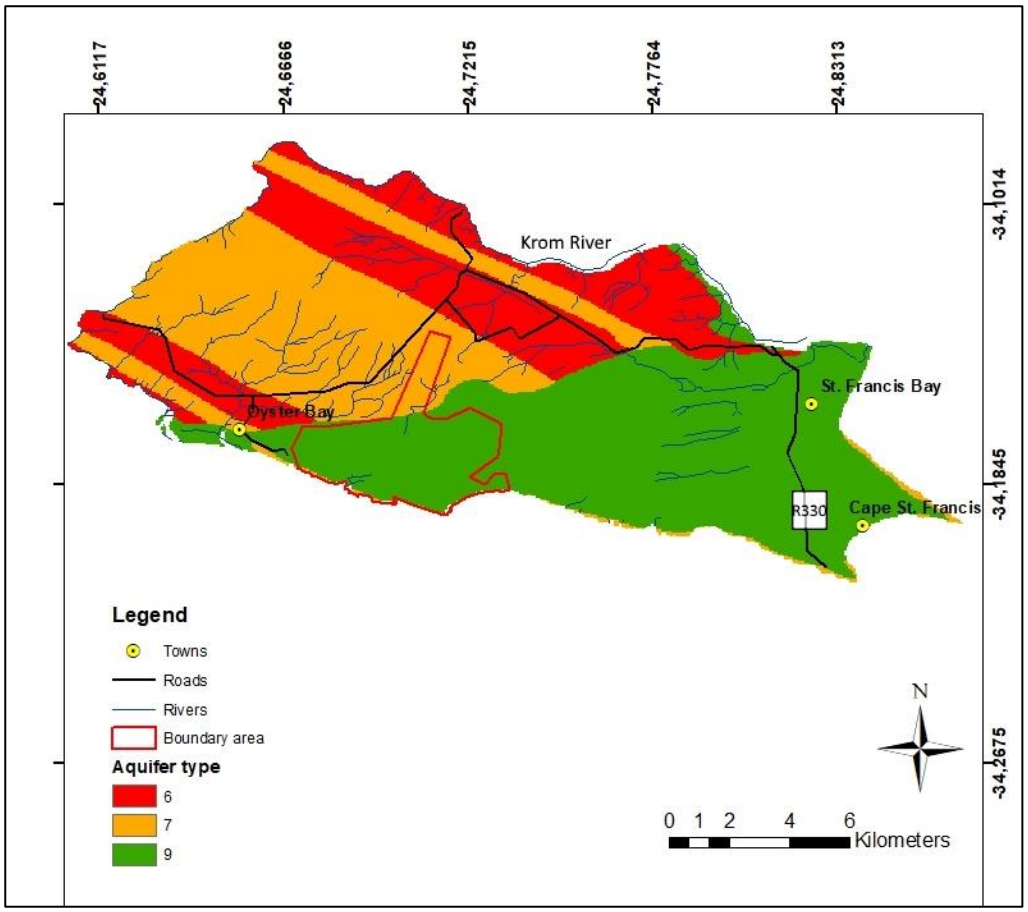

Figure 5.6. Aquifer rating map

5.4.Soil media

Figure 5.7 represents different soil types encountered in the study area. Sandy soil is the dominant soil type in the area. Although sandy soil dominates the area, it varies in grain size and organic content. Within the boundary area (Thyspunt Site), the grain size varies from fine sand in the vegetated areas to course grained in the dunes. Outside the Thyspunt site boundary, organic-rich, fine to medium-grained sandy soil dominates. Loam-sandy soil dominates the western periphery of the study area, whilst the northern periphery is characterised by sandy-clay soil. The soil associated vulnerability map indicates that the majority of the study area has a vulnerability rating of nine, and this is associated with the well-sorted, high infiltration rate of sandy soil (Figure 5.8). The western periphery has a vulnerability rating of 7, and this is linked to the loamy-sandy soil. The remainder of the area is characterised by a vulnerability of 4, and is associated with sandy-clay soil.

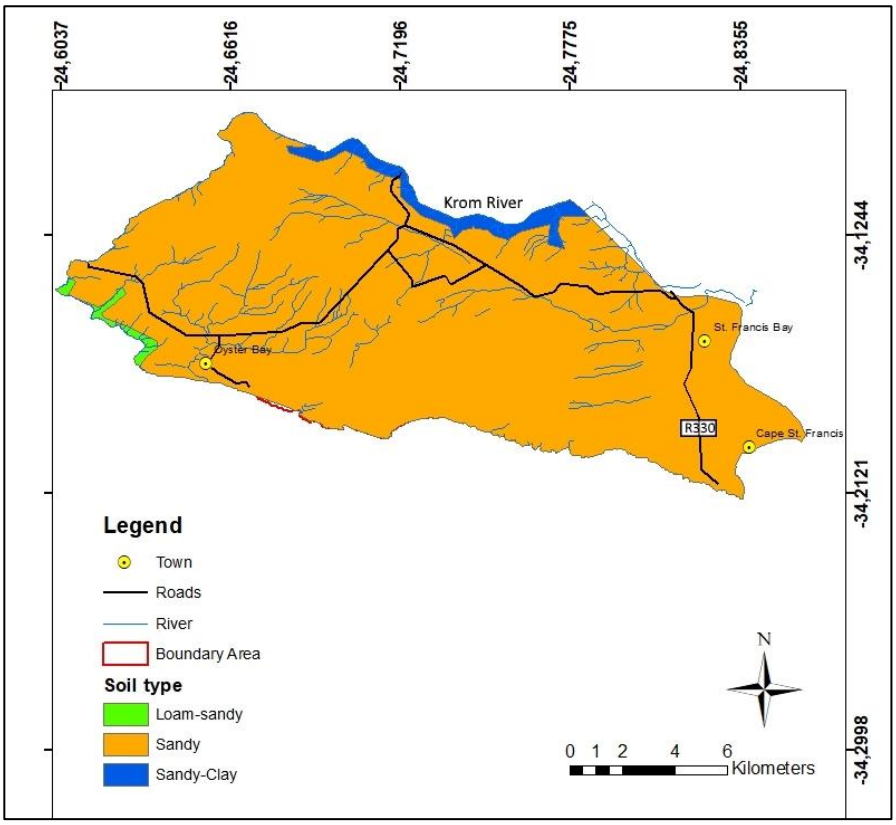

Figure 5.7. Soil map

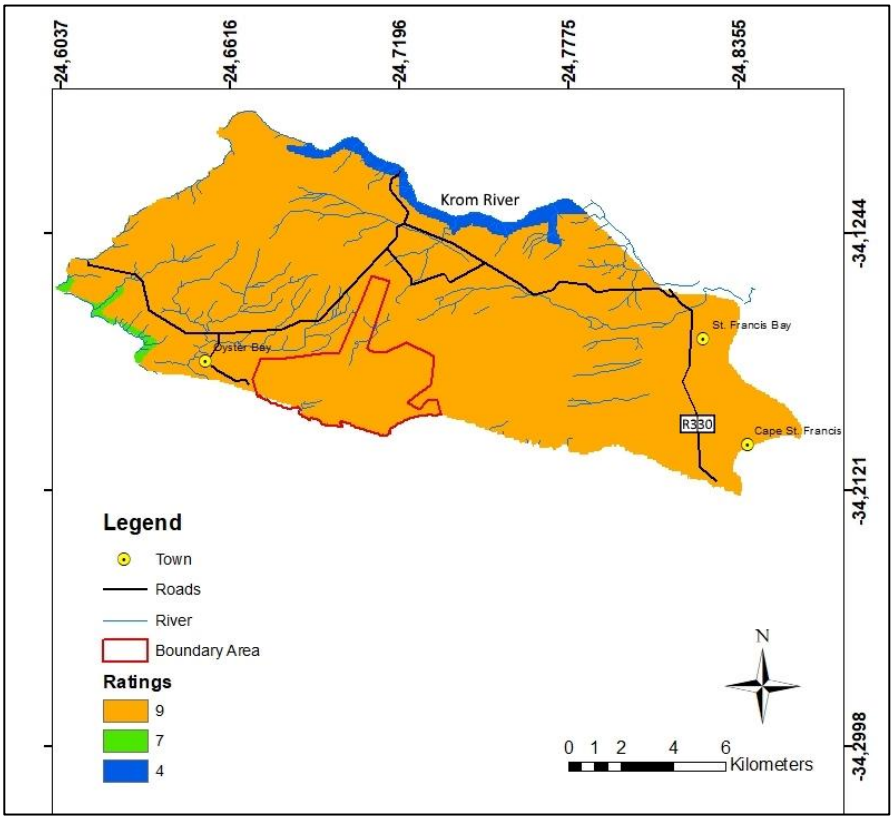

Figure 5.8. Soil rating map.

5.5.Topography

Figure 5.9 represents the slope percentage distribution of the area. The slope percentage generally decreases away from the centre of the study area. A vulnerability rating of 10 comprises the majority of the study area, with the majority of the area characterised by slope between 0 and 5%. The southern and northern peripheries of the area have variable vulnerability, ranging between 1 and 8 (Figure 5.10).

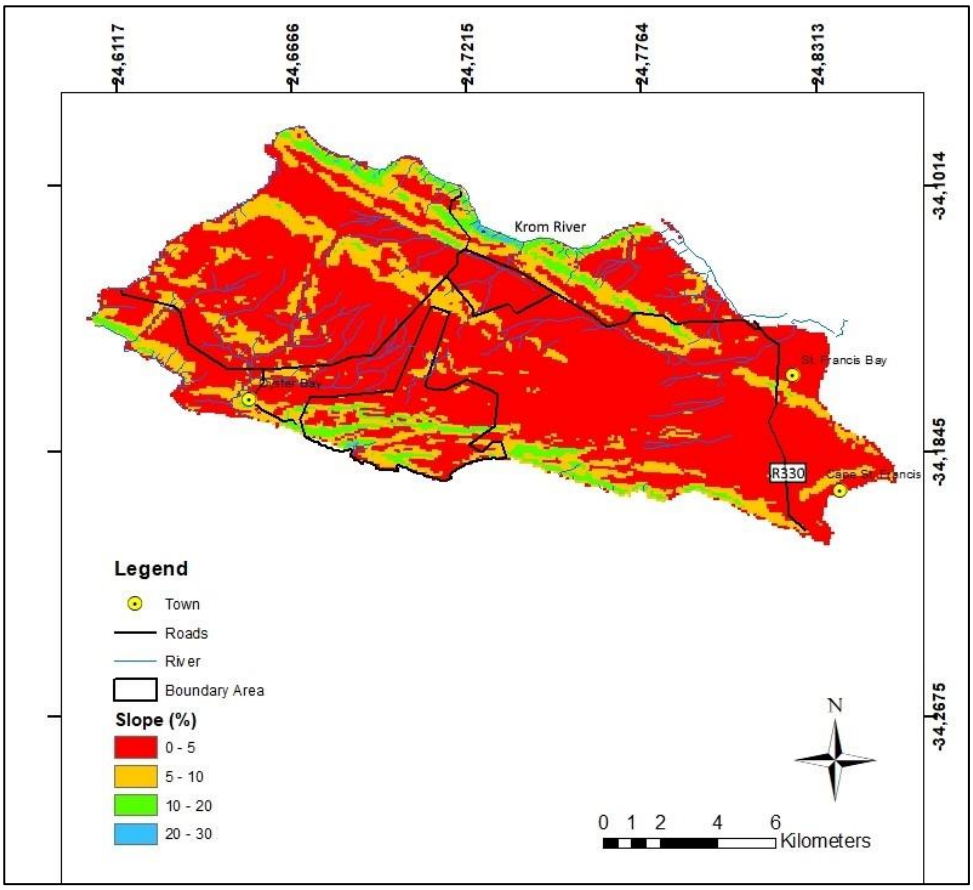

Figure 5.9. Slope percentage distribution

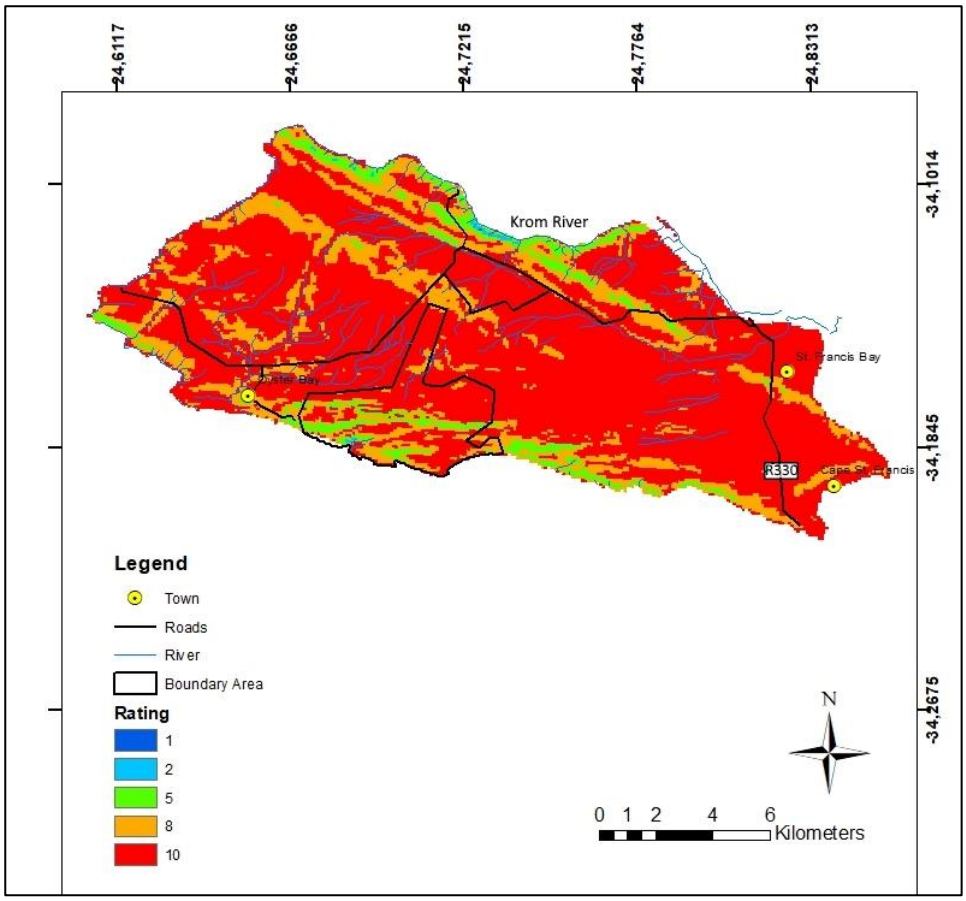

Figure 5.10. Topography rating map.

5.6. Impact of the vadose zone

The geological map of the area shows that indurated coastal sediments of the Algoa Group, Recent mobile dune deposits, and metasedimentary rocks of Table Mountain Group dominate the area (Figure 5.11). These lithologies also act as the vadose zones to the aquifers in the study area. A vadose zone related vulnerability map is presented in Figure 5.12. The vulnerability rating falls between 3 and 10. The highest rating was awarded to the mobile dunes and recent alluvial sediments. The western/norther-western portions of the study area are dominated by a vulnerability rating of 5. The eastern and southeastern sections of the study area are represented by vulnerability ratings of 9 and 10, and these are associated with indurated and mobile dunes, respectively. Indurated dunes are allocated a lower rating due to the reduced porosity, an aftermath of the compaction process. Vulnerability rating of 3 dominates the northern and southwestern peripheral areas.

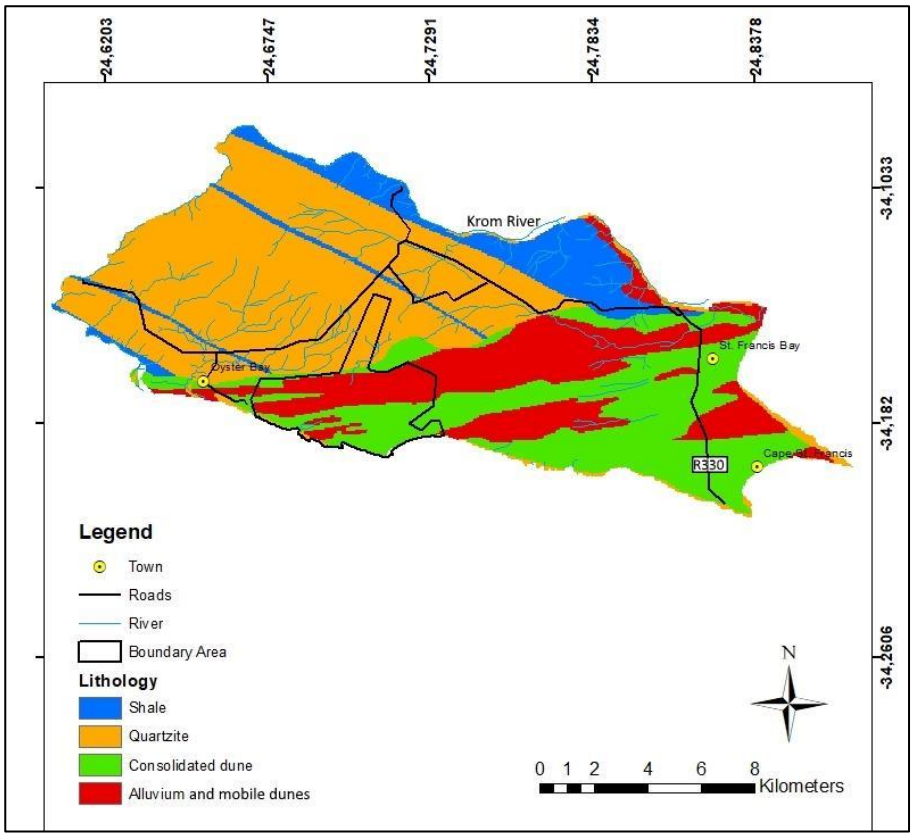

Figure 5.11. The lithology of the vadose zone map.

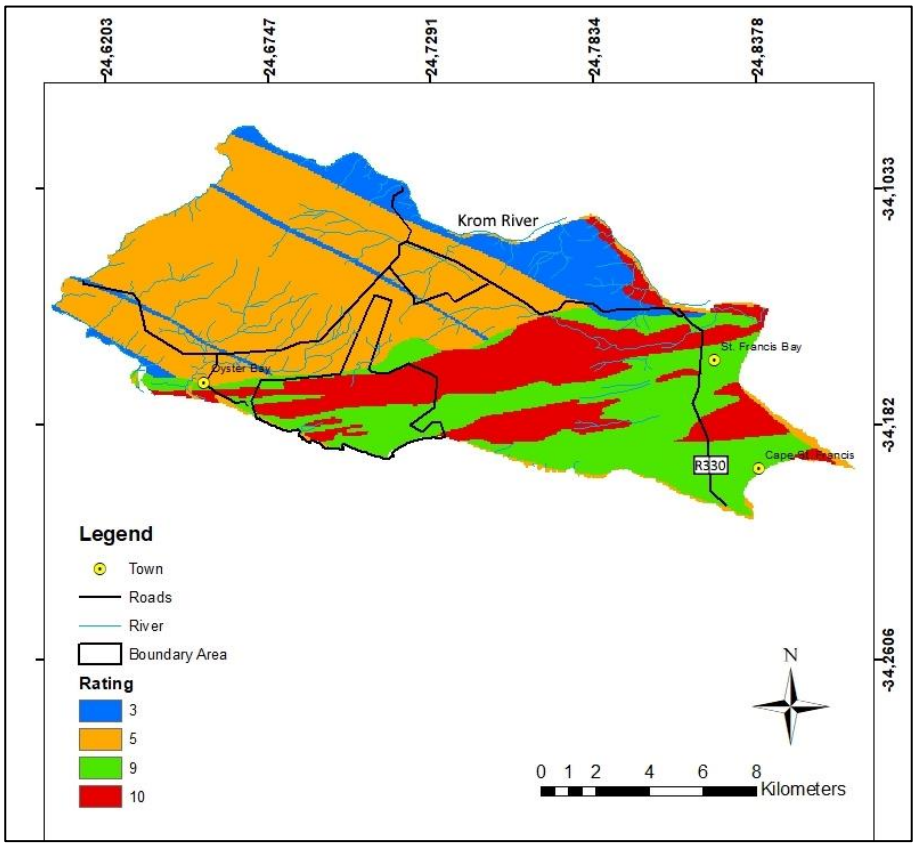

Figure 5.12. Vadose zone rating map.

5.7. Hydraulic Conductivity

The hydraulic conductivity of the area ranges between 0.012 to 19.12 m/day, and the majority of the aquifers have hydraulic conductivity values that range between 1 and 5 m/day (Figure 5.13). High conductivities are encountered in the highly porous and permeable sand dunes, whilst low conductivities are encountered in the metasedimentary rocks of the TMG. Figure 5.14 presents the conductivity-associated vulnerability of the area. Vulnerability ratings range between 2 and 10, with the majority of the study area classified with a rating of 7. The highest ratings are located within the Thyspunt site boundary where sand dunes and fractured quartzites make up the surface and immediate subsurface geology.

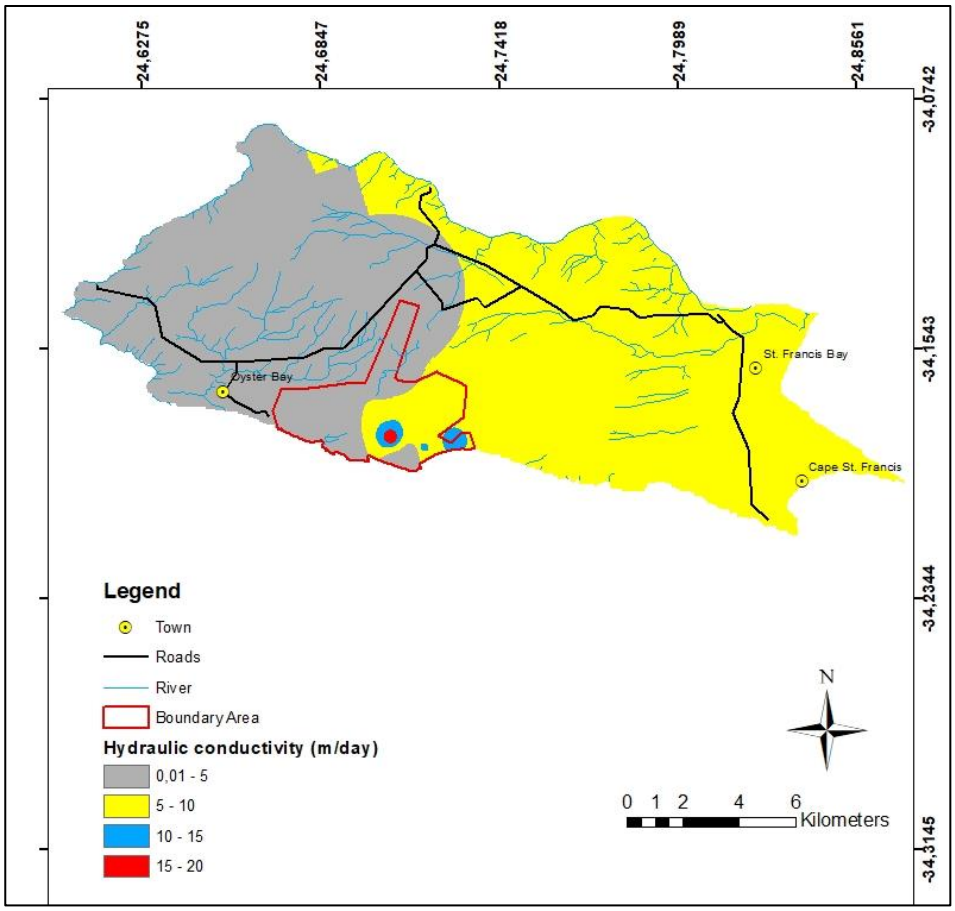

Figure 5.13. Hydraulic conductivity map.

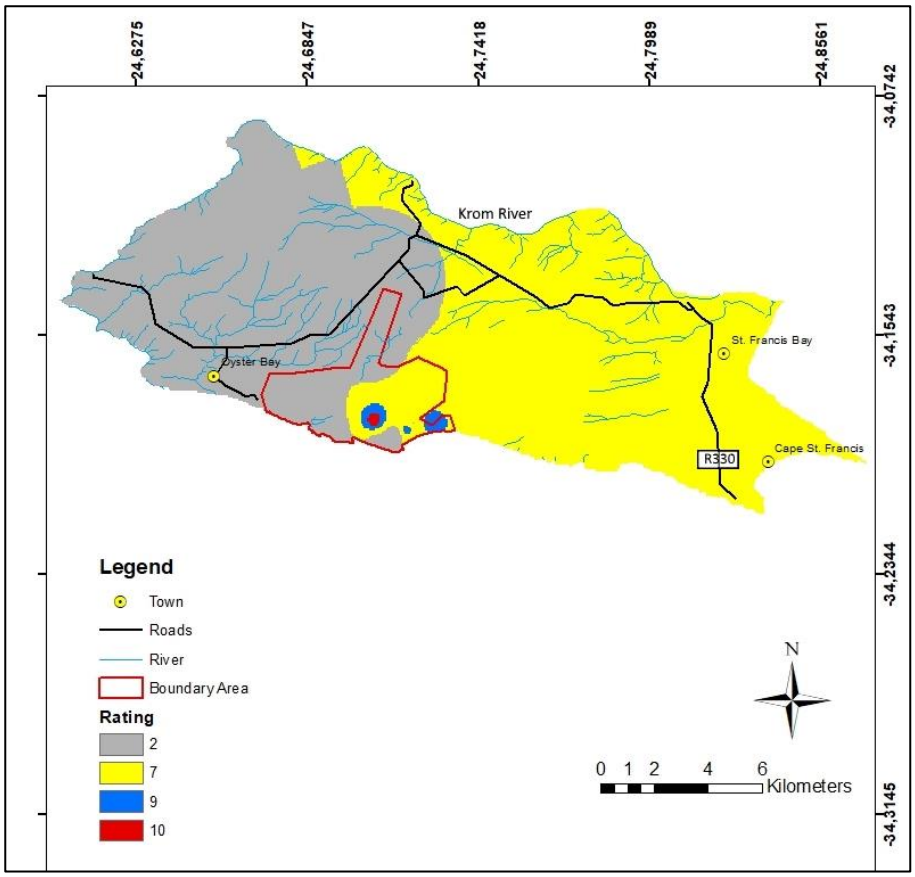

Figure 5.14. Hydraulic conductivity rating map.

5.8. Intrinsic vulnerability map

The DRASTIC index of the study area ranges between 30 and 65. For the practical application of the DRASTIC vulnerability map, the Drastic Index values were reclassified into three vulnerability degree zones, and this was modified from a classification by Witkowski et al., 2007. The Drastic Index results are presented in Table 5.1.

Table 5.1 DRASTIC Index and associated vulnerability degrees (modified from Witkowski et al., 2007)

DRASTIC Index	**Vulnerability degree**
30-41	Low vulnerability
42-53	Medium vulnerability
54-65	High vulnerability

According to the reclassified intrinsic DRASTIC vulnerability map, approximately 30% of the study area is classified as a high vulnerability zone (Figure 5.15). Both mobile and indurated dunes dominate this area. The high vulnerability to pollution is most likely a result of the porous sandy soil, relatively shallow groundwater levels, higher recharge rates and high conductivity of the dunes. The

majority of the area where most farms and settlements falls a medium vulnerability zone. Metasedimentary rocks of the TMG dominate this area, with the remaining portion characterised by indurated sand dunes. Fractured quartzite and shale aquifers, high topography, loam-rich sandy soil and deeper groundwater levels contribute to the medium vulnerability nature of the area. High topography lowers the likelihood of infiltration as high topography promotes surface runoff. In addition, relatively thick quartzite and to a lesser extent, shale comprise the vadose zone in most of the area. The thick and less permeable vadose zone indicate a lower probability for potential pollutants to enter the groundwater. In medium vulnerability regions dominated by dunes, the medium vulnerability could be attributed to deeper groundwater levels and higher topography. The remainder of the area, which constitutes less than 10% of the study area is classified as a low vulnerability zone and is mainly located on the northern periphery of the study area. Shales that belong to the Ceres Subgroup and Baviaanskloof Formation comprise the majority of the lithology. Sandy-clay soils with low porosity and permeability coupled with shale that make up the minority of the aquifers are responsible for the low vulnerability to pollution in the area.

According to Morris *et al.* (2003), a low vulnerability class implies that the groundwater/aquifer is only vulnerable to the most persistent pollutants in the long term. This, however, does not imply the aquifer is immune to pollution. Therefore, proper precautions are required to protect the aquifer. In contrast, high vulnerability implies vulnerability to most pollutants with the exception of pollutants that are easily transformed into other less harmful forms and/or adsorbed. About one-third of the study area is thus vulnerable to many pollutants whilst less than 10% of the area is only vulnerable to the most persistent pollutants overtime. More 50% of the Thyspunt site (boundary area) is classified as a high vulnerability zone, whilst the remaining area is a medium vulnerability zone. The Thyspunt site is mostly located on the sand dunes characterised by shallow groundwater levels, sandy soils, high recharge rates and thin clay-poor vadose zone. These characteristics are responsible for the high vulnerability nature of over 50% of the study area.

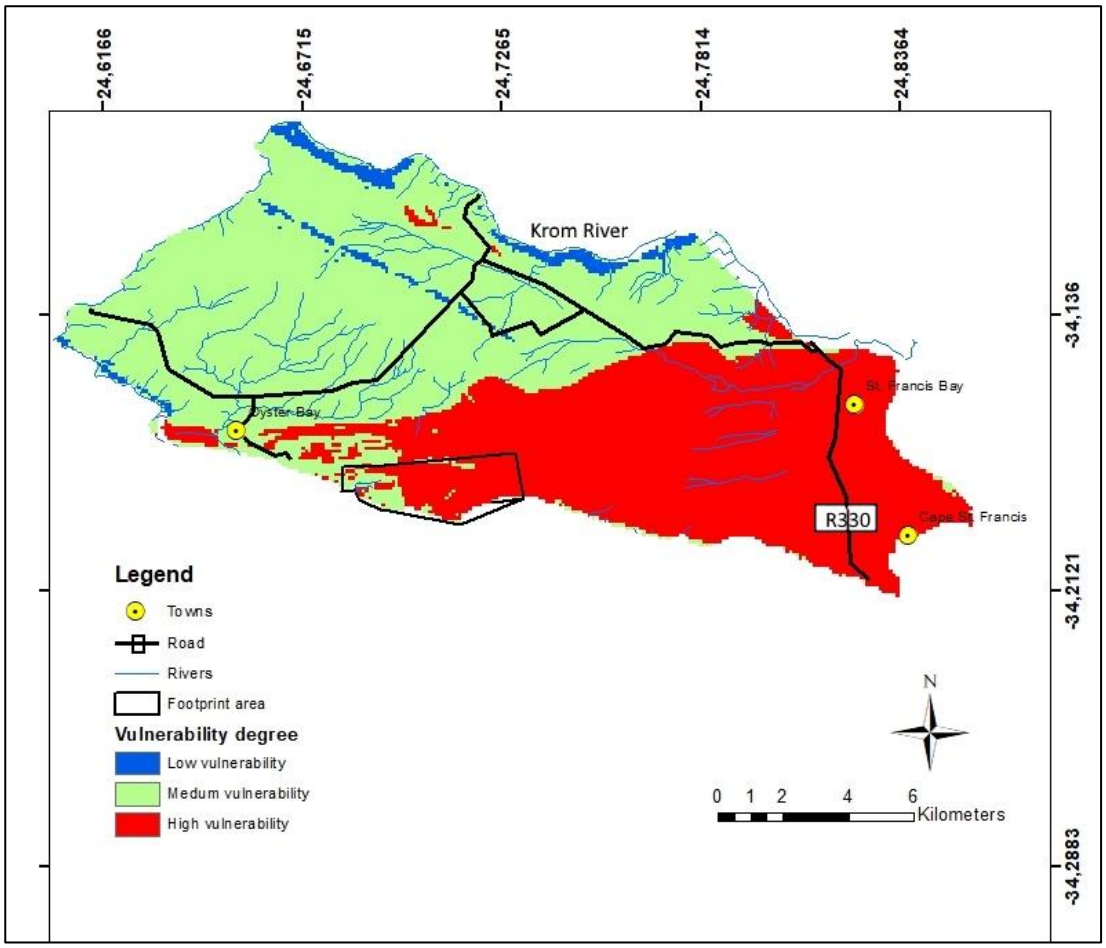

Figure 5.15. Intrinsic aquifer vulnerability to pollution map of the Thyspunt area.

5.9. Specific vulnerability map

The merit of the DRASTIC method is to allow us to create an ideal activity that could have impact on the environment. In this case, an ideal Nuclear Power Station was conceptualised and added to the seven DRASTIC parameters to generate a specific groundwater vulnerability to pollution map. The footprint area on the Eskom site is the proposed location of the nuclear power and related facilities, hence, the nuclear activity is restricted to this portion of the site (Figure 5.16). Additionally, the roads leading to the footprint area are also included since this could be considered as a potential risk due to possible accidents during the transportation of nuclear material and waste along the roads. During accidents, the nuclear material and waste could leak or spill into the environment and potentially into the aquifers. This, therefore, presents a potential contamination hazard to the aquifers. For the purpose of the vulnerability map, the footprint area was given a vulnerability weight of 5 and a rating of 10. As previously stated, the highest weight (w=5) and rating (r = 10) are assigned to the most significant parameter and the parameter that poses the highest risk, respectively. This is because nuclear activity has a high potential of polluting groundwater resources and therefore, potentially poses a high risk of

groundwater pollution. Furthermore, groundwater pollution emanating from radionuclides is very detrimental to the quality of groundwater, and therefore, any anthropogenic activity that can potentially introduce radionuclides into water (surface and groundwater) should be given high priority in pollution studies. A road buffer of 100 m was created and this represents the maximum areal extent of the accidental spills around the roads. The road buffer was assigned a vulnerability weight of 4 and a rating of 8. This is because the risk of accidental spills is less prominent than risks associated with the footprint area. The nuclear activity map of the study area and nuclear related groundwater vulnerability to pollution map are presented in Figure 5.16 and 6.17, respectively.

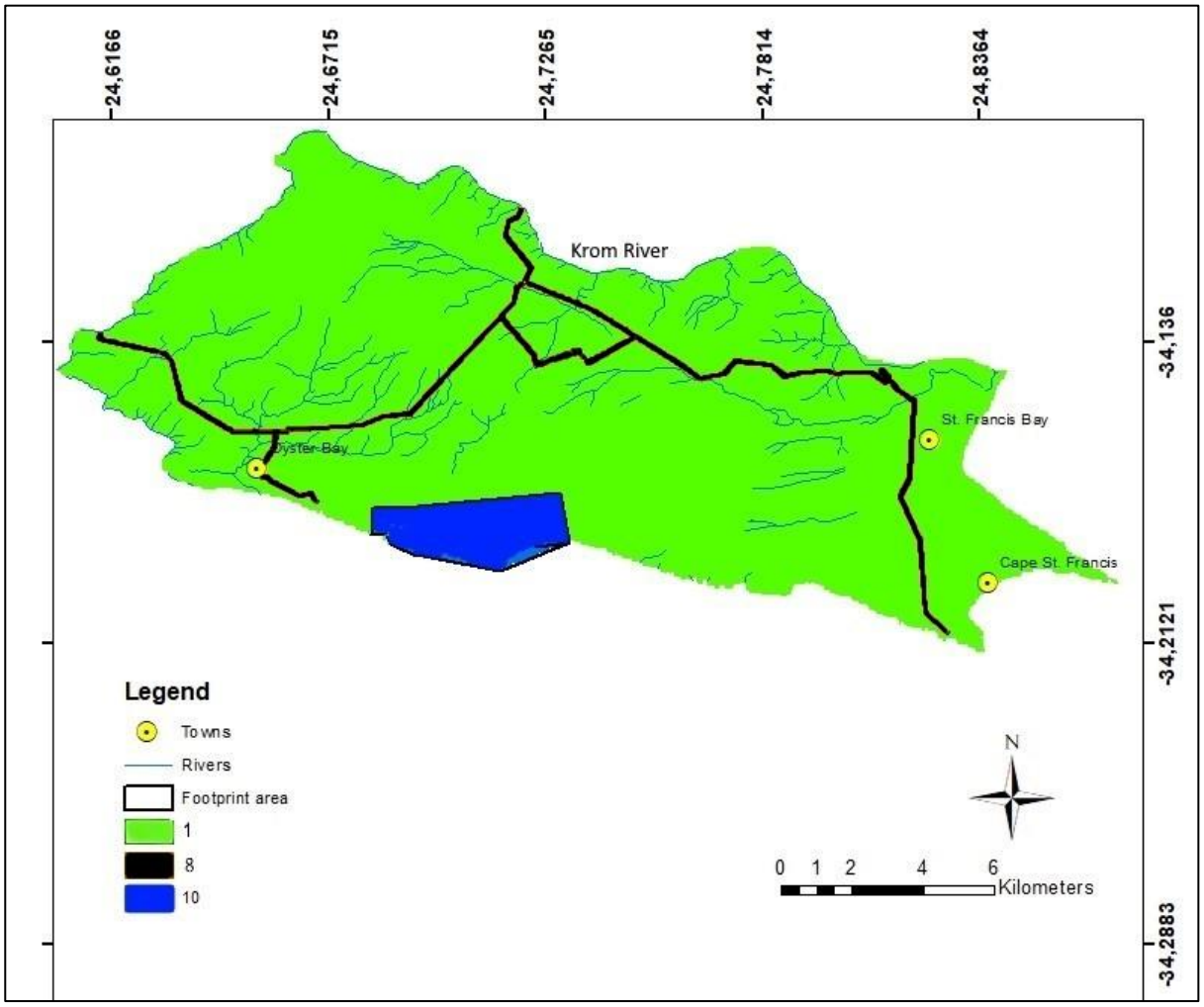

Figure 5.16. Nuclear activity rating map. Note that rating 8 refers to road buffer

Approximately 35% of the study area is classified as high vulnerability, and this includes about half of the footprint area. This is predominantly in the regions characterised by mobile and consolidated sand dunes. The porous sandy soil, relatively shallow groundwater levels, higher recharge rates and high conductivity of the dune deposits greatly contribute to the high vulnerability state. The medium vulnerability areas constitute about 35% of the study area, and are mostly in areas characterised by sandy-loam soils, high topography, relatively deeper groundwater levels and fractured quartzites and

shales, and to a lesser extent, dunes. Low vulnerability ratings are mostly restricted to areas characterised by shale, high topography and deep groundwater levels. Additionally, the nuclear power station is accompanied by numerous activities that have potential to affect the groundwater system. The road buffer area has both medium and high vulnerability ratings. High vulnerability is restricted to the north-eastern portions of the study area, an area classified as high vulnerability. The high vulnerability is a result of numerous factors, including shallow water levels, highly porous sandy soils, and high recharge rates. The addition of a potentially risky road for nuclear material transportation adds to the already highly vulnerable state of the area. Medium vulnerability constitutes the majority of the road buffer, and this is in the areas classified as medium and low vulnerability. The existing medium and low vulnerability conditions of these areas lower the vulnerability risk associated with the roads, and this is relative to the roads along the high vulnerability region. The footprint area, where the nuclear power plant and related facilities will be located, is classified as medium and high vulnerability zones. Approximately 80% of the footprint area is classified as high vulnerability zone. This is attributed to the high-risk nuclear plant, shallow groundwater levels in the underlying aquifers, high porosity sandy soils, intergranular (sand dune) aquifers and relatively gentle

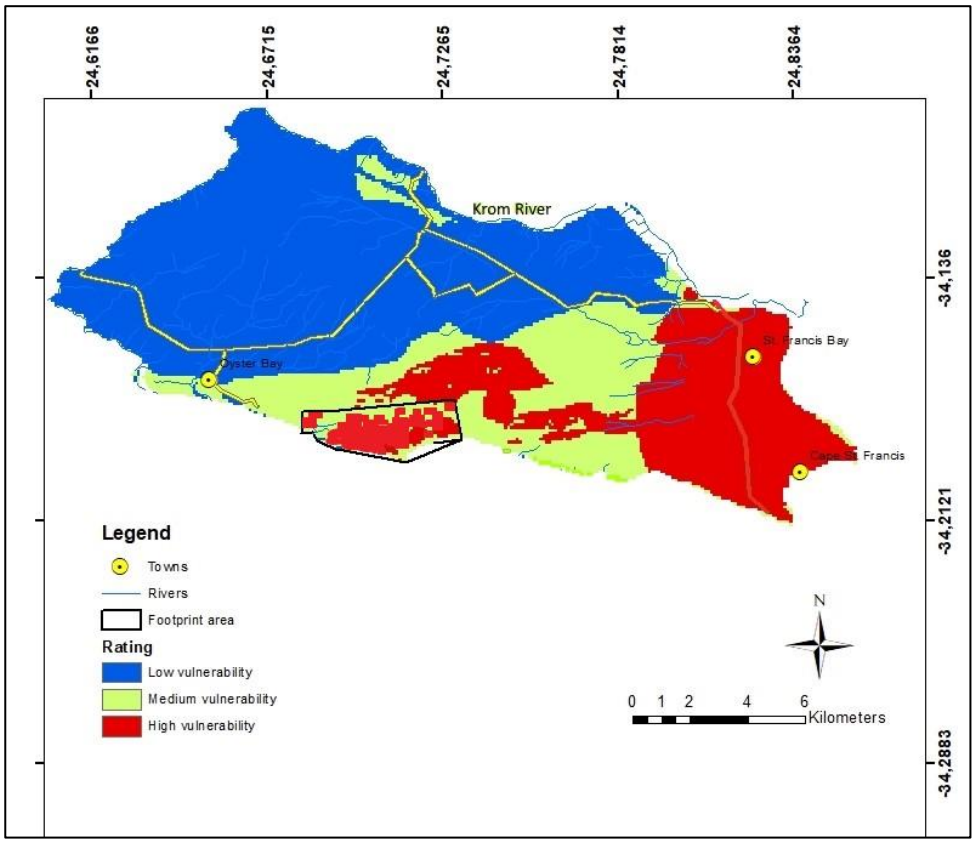

Figure 5.17. Specific vulnerability map, regarding the Nuclear Power Station in the Thyspunt area.

topography. The remainder of the footprint area is classified as a medium vulnerability area. This is in part attributed to the fractured quartzite bedrock, relatively deeper groundwater levels and relatively lower hydraulic conductivities of the aquifers. It is worth noting that the addition of the nuclear activity map as an additional parameter to the DRASTIC parameters results in lower vulnerability ratings compared to the intrinsic map. This is because the areas outside the footprint area were assigned a rating of 1, and this greatly lowered the degree of vulnerability for the majority of the study area.

5.10. Drastic validation

Isotopes

Isotopes can be used as a useful validation tool for vulnerability to pollution maps. Groundwater that has evaporation and/or rainfall isotopic signatures indicates some surface residence time of the recharging water prior to recharging the groundwater systems. Such recharging water is a potential carrier of pollutants and can introduce pollutants to the groundwater system. The stable isotope plot of the groundwater samples is presented in Figure 4.27. It is worth noting that the sampled aquifers are located within and in the immediate vicinity of the footprint area, thus only isotope results for these areas are presented. None of the sampled aquifers (through boreholes) have isotopic signatures that represent evaporative signatures and direct rainfall recharge. This observation implies that the recharging water was not subjected to any evaporation prior to entering the groundwater system, thus instead suggesting the recharging water did not spend a considerable time as surface water prior to recharging the aquifers. The risk of pollutants assimilating into (recharging) water lowers as the period that the water spends on surface shortens. This, therefore, lowers the threat to potentially introduce pollutants to the groundwater systems. The highly depleted isotopic signatures of all the groundwater suggests groundwater recharge by a high latitude moisture source and/or recharge during colder seasons. The presence of recharge indicates that the vadose zone does not hinder recharging water and the pollutants from reaching the aquifers. This therefore poses a potential of groundwater pollution by surface-sourced pollutants. These results therefore suggest a medium to high degree of vulnerability to pollution of the aquifers in the study area. This observation agrees with parts of the Thyspunt site where the sampled aquifers are located. The area from which the isotope samples were collected contains both medium and high vulnerability zones. This therefore, proves the validity of the intrinsic vulnerability map. Additionally, more isotope data from other parts of the study area could strengthen the validation of the intrinsic map.

6. CONCLUSION

The integrated application of data from pumping tests, meteorological parameter estimations, hydrochemical analyses, geological and hydrogeological investigations proved to be useful in developing a conceptual model for the Thyspunt Nuclear site. The TMG, Algoa Group and recent mobile dune deposits comprises the majority of the geology of the area. The Algoa Group sediments together with the Quaternary dune deposits and meta-sandstones of the TMG comprise the unconfined aquifers in the area. Underlying the unconfined aquifers are fractured and confined aquifers composed of the TMG quartzites. The results suggest that different aquifer types have different physical properties, including a difference in groundwater levels. Hydrochemical data indicates that Ca-Mg-HCO_3 are the dominant ions in both surface water and groundwater. Additionally, a hydrogeochemical evolution from Ca-Mg-HCO_3-dominated fresh groundwater to more saline groundwater dominated by Na and Cl ions in the direction of groundwater flow was noted. Mixing of water has also been identified closer to the coast, indicating convergence of different flow systems and eventual mixing en-route to the ocean. Shale from the Ceres Subgroup and Baviaanskloof Formation generally have elevated concentrations of trace metals (e.g. titanium, lead, uranium and thorium). The area is generally known to contain high background level of toxic metals and radionuclides. From a pollution perspective, water that interacts with the rocks in Thyspunt area could have a higher chance of containing potentially hazardous metals due to water-rock interaction. This is also the case for soil sampled from the footprint area, which shows elevated concentrations of uranium (1.741 ppm). Extra attention should, therefore, be given to water that comes in contact with shales as a precautionary measure to health protection. A strong hydraulic link exists between most aquifers and springs, as indicated by the stable isotope results. The strong hydraulic link could be detrimental from a pollution perspective because the contamination of one could result in contamination of all linked water sources. The absence of seawater intrusion in the sampled aquifers is likely made possible by the orientation of the local geology, which dips towards the ocean, therefore, inhibiting the ingress of seawater into the aquifers. Multiple moisture sources are responsible for the rainfall occurrence in the study area. Recharge largely occurs at a regional scale, although a point recharge is possible throughout the area.

The groundwater vulnerability to pollution assessment through the application of DRASTIC model indicates that the study area has three pollution categories: low, medium and high vulnerability; and this is evident on both the intrinsic and specific “nuclear activity” maps. Based on the result, the footprint is located on high vulnerability zone that will require profound attention. The locations of the areas with the highest infiltration capacities coincide with the areas categorised as having high vulnerability to pollution. Additional isotopes data will increase the robustness and validity of the

vulnerability maps, even though the validation of the vulnerability maps with stable isotopes proved successful. Even though the degree of groundwater vulnerability to pollution varies across the study area, it is important to note that all groundwater resources are in fact vulnerable to pollution. Sustainable and conservative groundwater use should always be practiced to ensure the protection of groundwater resources at all times. DRASTIC proved successful in assessing the degree of vulnerability of the Thyspunt area.

The lack of data, including long-term monitoring data of different meteorological parameters and groundwater level, and groundwater discharge have limited the estimation of a water budget for the study area. The acquisition of more data will, therefore, increase the robustness of the conceptual model and enhance the understanding of the hydrogeological dynamics of the Thyspunt area. It is also suggested to monitor water level for over a decade in order to get an insight into the long term groundwater level fluctuation.

7. RECOMMENDATIONS

The following recommendations are proposed based on the outcomes of this research:

1. Continuous, long-term monitoring of meteorological and groundwater level should be implemented. This will help improve hydrological parameter estimations such as evapotranspiration and recharge.

2. The measurement and recording of runoff and stream discharge should commence. This will be crucial for water budget estimations and subsequently, adequate groundwater management.

3. Better management and maintenance of the boreholes drilled on the Eskom site should be implemented. This will ensure protection of the groundwater resources and contribute towards high quality data recording through the installed data loggers.

4. Continuous water sampling for isotopes and water chemistry should be implemented to ensure better understanding of the hydrogeological dynamics and conditions of the study area.

5. The relevant policies and precautionary measures should be implemented to ensure the protection of groundwater resources, especially on the Eskom site.

8. REFERENCES

Ahmed, A. (2009). Using lithologic modelling techniques for aquifer characterisation and groundwater flow modelling of the Sohag area, Egypt, *Hydrogeology Journal*. 17, pp. 1189–1201

Alcala, F.J. and Custodio, E. (2008). Using the Cl/Br ratio as a tracer to identify the origin of salinity in aquifers in Spain and Portugal. *Journal of Hydrology*. 359, pp. 189– 207

Aller, L., Bennet, T., Lehr, J.H., Petty, R.J., (1987). *DRASTIC: A Standardized System for Evaluating Ground Water Pollution Using Hydrological Settings*. US EPA document no.EPA/600/2-85-018.

Al-Kharouf, S.J., Al-Hamarneh, I.F. and Dababneh, M. (2008). Natural radioactivity, dose assessment and uranium uptake by agricultural crops at Khan Al-Zabeeb, Jordan, *Journal of Environmental Radioactivity*. 99, pp.1192 – 1199.

Bethke, C.M. and Johnson, T.M. (2008). Groundwater Age and Groundwater Age Dating, Annual Review of Earth and Planetary Sciences. 36, pp.121-152

Chilton, J. (1996). *Water Quality Assessments - A Guide to Use of Biota, Sediments and Water in Environmental Monitoring* – 2nd edn. UNESCO/WHO/UNEP, Chapter 9

Christ, R.D. and Wernli, R.L. (2014). The ROV Manual: The Ocean Environment-2nd edn., Chapter 9.

Claassen, D. (2014). Geographical Controls on Sediment Accretion of The Cenozoic Algoa Group Between Oyster Bay and St. Francis, Eastern Cape Coastline, South Africa, *South African Journal of Geology*. 117, pp.109–128

Cothern, R.C., and Rebers, P.A. (1990). *Radon, radium and uranium in drinking water*, Lewis Publishers, Inc., pp. 286.

Department of Environmental Affairs (2016). Nuclear-1 EIA, Draft Environmental Management Plan – Revision 2. DEA Reference No.: 12/12/20/944

Department of Water Affairs (2010). Eastern Cape Groundwater Master Plan. DWA EC Office, Port Elizabeth. pp. 41

Department of Water Affairs and Forestry (1996). *South African Water Quality Guidelines, Volume 1 Domestic Use*, 2nd Edition.

Fritz, P., Fonte, J.C., Frape, S.K., Louvat, D., Michelot, J.L. and Balderer, W. (1988). The isotope geochemistry of carbon in groundwater at Stripa, *Geochimica de Cosmochimica Ado*. 53, pp. 1765-1175

Giacinto, J., Barnhurst, D. and Tiruneh, N. (2010). Conceptual Groundwater Model Development for New Nuclear Power Plants. 2nd Joint Federal Interagency Conference, Las Vegas, NV, June 27 - July 1, pp.1-12.

Han, D., Kohfahl, C., Song, X., Xiao, G. and Yang, J. (2011). Geochemical and isotopic evidence for palaeo-seawater intrusion into the south coast aquifer of Laizhou Bay, China, *Applied Geochemistry*. 26, pp. 863–883

Horne, A.J. & Goldman, C.R. (1994). Limnology, 2nd edn. Mc Graw-Hill. Inc. pp. 576.

Leyland, R.C., Witthüser, K.T. and van Rooy, J.L. (2008). Vulnerability Mapping in Karst Terrains, Exemplified in the Wider Cradle of Humankind World Heritage Site. Water Research Commission, pp. 1- 104.

Manga, M. (2001). Using springs to study groundwater flow and active geologic processes, *Annual Reviews Earth Planet Science.* 29,pp. 201–28

Neuman, S.P. (1974). Effect of partial penetration on flow in unconfined aquifers considering delayed gravity response, *Water Resources Research*, 10(2), pp. 303-312.

NRC (National Research Council) (1993) *Ground Water Vulnerability Assessment: Contamination Potential under Conditions of Uncertainty*. National Academy Press, Washington DC

Ojovan, M.I. and Lee, W.E. (2014). Naturally Occurring Radionuclides, Immobilisation (2nd edn). pp. 31-39

Theis, C.V. (1935). The relation between the lowering of the piezometric surface and the rate and duration of discharge of a well using groundwater storage, *Am. Geophys*. Union Trans., 16, pp. 519-524.

Talling, J.F. and Talling, I. B. (1965). The Chemical Composition of African Lake Waters, *International review of Hydrobiology*. 50, pp. 421 – 456.

Taylor, A.R., Smith, S.D., Lamontagne, S. and Suckow, A (2017). Characterising alluvial aquifers in a remote ephemeral catchment (Flinders River, Queensland) using a direct push tracer approach, *Journal of Hydrology*. 556, pp. 600–610

UNICEF. (2008). UNICEF Handbook on Water Quality. United Nations Children's Fund (UNICEF), New York, USA. pp. 179.

World Health Organization (WHO). 2011. Guidelines for drinking-water quality (4th ed.). WHO Library Cataloguing-in-Publication Data, pp. 564.

Yilmaz, E. & Koc, C. (2014). Physical and chemical evaluation for the water quality criteria in a farm on Akcay. *Journal Water Resources*, 6, pp. 63-67.

WHO (2003). Uranium in drinking water. Background document for preparation of WHO Guidelines for drinking-water quality. Geneva, World Health Organization (WHO/SDE/WSH/03.04/118)

Witkowski, A.J., Kowalczyk, A. and Vrba, J. (2007). Groundwater Vulnerability Assessment and Mapping : selected papers from the Groundwater Vulnerability Assessment and Mapping International Conference : Ustron, Poland, 2004. Taylor & Francis e-Library, pp. 105.

Xu, Y. and Beekman H.E. (2003) *Groundwater Recharge Estimation in Southern Africa.* UNESCO IHP Series No. 64. UNESCO, Paris.